

OPTIMAL LOCOMOTION OF MECHANICAL RECTIFIER SYSTEMS

A Dissertation

Presented to

the Faculty of the School of Engineering and Applied Science

University of Virginia

In Partial Fulfillment

of the Requirements for the Degree

Doctor of Philosophy in Mechanical and Aerospace Engineering

by

Justin T. Blair

August 2011

UMI Number: 3484633

All rights reserved

INFORMATION TO ALL USERS

The quality of this reproduction is dependent upon the quality of the copy submitted.

In the unlikely event that the author did not send a complete manuscript and there are missing pages, these will be noted. Also, if material had to be removed, a note will indicate the deletion.



UMI 3484633

Copyright 2011 by ProQuest LLC.

All rights reserved. This edition of the work is protected against unauthorized copying under Title 17, United States Code.



ProQuest LLC
789 East Eisenhower Parkway
P.O. Box 1346
Ann Arbor, MI 48106-1346

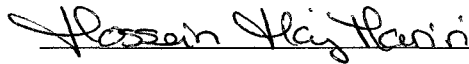
APPROVAL SHEET

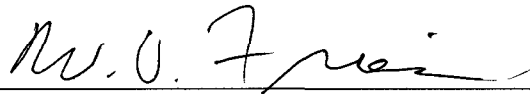
The dissertation is submitted in partial fulfillment
of the requirements for the degree of
Doctor of Philosophy in Mechanical and Aerospace Engineering

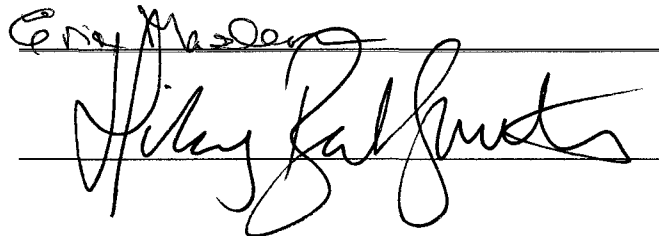

AUTHOR

This dissertation has been read and approved by the examining committee:


Dissertation Advisor







Accepted for the School of Engineering and Applied Science:


Dean, School of Engineering and Applied Science

August 2011

Contents

Abstract	iv
Acknowledgments	v
List of Figures	x
List of Tables	xii
List of Symbols	xiii
1 Introduction	3
1.1 Overview	3
1.2 Relation to the current state of knowledge	4
1.2.1 Optimality of animal locomotion	4
1.2.2 Biologically inspired locomotors	5
1.2.3 Locomotor models	7
1.2.4 Optimal gaits for robotic locomotors	7
1.2.5 Application of batoids to underwater vehicles	9
1.2.6 Biology of batoids and related modeling research	9
1.3 Objectives	11
1.4 Notation	12

2	General Framework for Animal Locomotion	14
2.1	Mechanical rectifier systems	14
2.1.1	General equations of motion	15
2.1.2	Derivation of the generalized force	17
2.2	Mechanisms underlying thrust generation	20
2.2.1	Nominal posture and approximation	20
2.2.2	Bilinear mechanism for rectification	22
3	Optimal Gait Problem	24
3.1	Optimal locomotion of the bilinear rectifier	24
3.1.1	Problem formulation	24
3.1.2	Tractable reformulation	26
3.1.3	Globally optimal solution	28
3.2	Verification through case studies	33
3.2.1	Simple mechanical rectifier	34
3.2.2	Link chain rectifier	38
4	Flapping-Wing Rectifier	47
4.1	Flapping-Wing Model	47
4.1.1	Overview	47
4.1.2	Equations of motion	49
4.1.3	Model parameters	55
4.2	Flapping Gait Analysis	62
4.2.1	Observed and perturbed gait	62
4.2.2	Effects of wing geometry on basic flapping gaits	64
4.2.3	Optimal Gaits	68
5	Conclusion	77
5.1	Summary	77

5.2	Future Work	79
6	Appendix	82
6.1	Preliminary lemmas	82
6.2	Link chain rectifier model	84
6.3	Batoid thickness data	87
6.4	Natural modes	92
6.5	Basic gaits	98
6.6	Optimal gaits	102
6.6.1	Minimum objective values vs. frequency, ω	102
6.6.2	Minimum curvature rate gaits	105
6.6.3	Minimum power gaits	111
6.6.4	Minimum actuation rate gaits	117

Abstract

Vehicles utilizing animal locomotion mechanisms may possess increased performance parameters and the ability to overcome more difficult terrain than conventional wheel or propeller driven vehicles. The essential mechanism underlying animal locomotion can be viewed as mechanical rectification that converts periodic body movements to thrust force through interactions with the environment. This dissertation defines a general class of mechanical rectifiers as multi-body systems equipped with such thrust generation mechanisms. A general model is developed from the Euler-Lagrange equation and simplified by assuming small body oscillations around a given nominal posture. The model reveals that the rectifying dynamics can be captured by a bilinear (but not linear) term of body shape variables. An optimal gait problem is formulated for the bilinear rectifier model as a minimization of a quadratic cost function over the set of periodic functions subject to a constraint on the average locomotion velocity. We prove that a globally optimal solution is given by a harmonic gait that can be found by generalized eigenvalue computation with a line search over cycle frequencies. We verify the solution method through case studies of a two dimensional chain of links for which snake-like undulations and jellyfish-like flapping gaits are found to be optimal, and obtain analytical insights into determinants of optimal gaits from a simple disk-mass rectifier system. Lastly, we develop a dynamic model for batoid swimming featuring a 6 degree-of-freedom main body (position and orientation), with independent wing deformation (described as the motion of many discrete points in the body-fixed coordinate frame), and calculate various gaits. Multiple wing shapes and optimality criteria are considered, such as the maximum thrust to deflection ratio or minimum input power, and the resulting gaits are compared.

Acknowledgments

We thank T. Iwasaki at the University of California, Los Angeles, for his tireless guidance with this research, W.O. Friesen and J. Chen at the University of Virginia for providing the measured data for a leech, S. Russo at the University of Virginia for providing the measured joint and thickness data for batoid wings, F. Fish at West Chester University for the batoid scans and deflection test data, and the countless other people who have lent their support over the years.

List of Figures

2.1	Multilink swimming system	15
3.1	Exploiting symmetry of the frog-like multilink system	28
3.2	Simple mechanical rectifier	34
3.3	Link chain rectifier	39
3.4	Objective function vs. frequency ω : power in mW, torque in $(\text{N}\cdot\text{mm}\cdot 100)^2$, shape derivative in $(\text{deg}/\text{ms})^2$	41
3.5	Optimal body shapes (snap shots during swimming at an arbitrary time instant)	41
3.6	Undulatory gaits: Phase and amplitude of relative angles ϕ_i along the body	42
3.7	Flapping gaits: Phase and amplitude of relative angle perturbations $B^T\vartheta$ along the body	44
3.8	Snap shots of LCR locomotion, taken 1.25 periods apart.	45
3.9	Simulated CG velocity	46
4.1	Flapping-wing system with point mass wings.	48
4.2	Euler angle convention.	48
4.3	Torque approximation.	49
4.4	Normal vectors for point mass i	52
4.5	Surface normal and velocity projections.	52
4.6	Atlantic, Butterfly, and Cownose joint locations, [mm].	57

4.7	Atlantic (rectangular, radial), Butterfly (rectangular), and Cownose (rectangular, radial, and shifted radial) grids.	59
4.8	Atlantic bending test, gravity is to the right.	61
4.9	Simulated bending test for uniform and thickness-proportional stiffness, rectangular grid.	61
4.10	Simulated bending test for uniform and thickness-proportional stiffness, radial grid.	61
4.11	Biological gait amplitude and phase contour and perturbed gait amplitude and phase contour for the Atlantic ray.	64
4.12	Basic gait snapshots for the Cownose ray.	65
4.13	Basic gait amplitudes (top) and phases (bottom).	66
4.14	High-aspect rectangular wing basic gait snapshots.	67
4.15	Low-aspect rectangular wing basic gait snapshots.	67
4.16	High and low-aspect rectangular wing basic gaits (amplitude and phase) . .	68
4.17	Minimum curvature gait snapshots for the Atlantic (top), Butterfly (mid), and Cownose (bottom) rays, rectangular grid.	69
4.18	Minimum curvature gait amplitude (top) and phase (bottom) contour plots for the Atlantic (left), Butterfly (mid), and Cownose (right) rays, rectangular grid.	70
4.19	Minimum power gait snapshots for the Atlantic (top), Butterfly (mid), and Cownose (bottom) rays, rectangular grid.	70
4.20	Minimum actuation gait snapshots for the Atlantic (top), Butterfly (mid), and Cownose (bottom) rays, rectangular grid.	71
4.21	Two snapshots of the minimum actuation gait (top) and associated natural mode (bottom), 1st mode Atlantic ray (left), 5th mode Butterfly ray (right).	72
4.22	Minimum actuation gait snapshots for the Atlantic ray (top) and Cownose ray (bottom), radial grid.	73

4.23	Minimum curvature rate gait snapshots, Cownose, rectangular grid.	74
4.24	Amplitude and phase contour plots for the minimum curvature rate gait, Cownose, rectangular grid.	74
4.25	Minimum power gait snapshots, Atlantic, rectangular grid.	75
4.26	Amplitude and phase contour plots for the minimum power gait, Atlantic, rectangular grid.	75
4.27	Amplitude (3D), amplitude contour, and phase contour plots for the mini- mum actuation rate gait, Atlantic, rectangular grid.	76
6.1	Atlantic cross sections for thickness measurements.	87
6.2	Butterfly cross sections for thickness measurements.	88
6.3	Cownose cross sections for thickness measurements.	89
6.4	First 10 natural modes for Atlantic rectangular grid, two snapshots each. . .	92
6.5	First 10 natural modes for Atlantic radial grid, two snapshots each.	93
6.6	First 10 natural modes for Butterfly rectangular grid, two snapshots each. .	94
6.7	First 10 natural modes for Cownose symmetric rectangular grid (symmetric constraint), two snapshots each.	95
6.8	First 10 natural modes for Cownose radial grid, two snapshots each.	96
6.9	First 10 natural modes for Cownose shifted radial grid (symmetric con- straint), two snapshots each.	97
6.10	Basic gait for Atlantic rectangular grid.	98
6.11	Basic gait for Atlantic radial grid.	99
6.12	Basic gait for Butterfly rectangular grid.	99
6.13	Basic gait for Cownose rectangular grid (symmetric constraint).	100
6.14	Basic gait for Cownose radial grid.	100
6.15	Basic gait for Cownose radial shifted grid (symmetric constraint).	101
6.16	Min. obj. vs ω , Top to bottom: Curv., Curv.Rate, Power, Act., Act.Rate . .	102

6.17	Min. obj. vs ω (continued), Top to bottom: Curv., Curv.Rate, Power, Act., Act.Rate	103
6.18	Symmetry vs ω (zero:symmetric, nonzero:anti-symmetric), Top to bottom: Curv., Curv.Rate, Power, Act., Act.Rate	104
6.19	Minimum curvature rate gait for Atlantic rectangular grid.	105
6.20	Minimum curvature rate gait at ω_{bio} for Atlantic rectangular grid.	105
6.21	Minimum curvature rate gait for Atlantic radial grid.	106
6.22	Minimum curvature rate gait at ω_{bio} for Atlantic radial grid.	106
6.23	Minimum curvature rate gait for Butterfly rectangular grid.	107
6.24	Minimum curvature rate gait at ω_{bio} for Butterfly rectangular grid.	107
6.25	Minimum curvature rate gait for Cownose rectangular grid (symmetric constraint).	108
6.26	Minimum curvature rate gait at ω_{bio} for Cownose rectangular grid (symmetric constraint).	108
6.27	Minimum curvature rate gait for Cownose radial grid.	109
6.28	Minimum curvature rate gait at ω_{bio} for Cownose radial grid.	109
6.29	Minimum curvature rate gait for Cownose radial shifted grid (symmetric constraint).	110
6.30	Minimum curvature rate gait at ω_{bio} for Cownose radial shifted grid (symmetric constraint).	110
6.31	Minimum power gait for Atlantic rectangular grid.	111
6.32	Minimum power gait at ω_{bio} for Atlantic rectangular grid.	111
6.33	Minimum power gait for Atlantic radial grid.	112
6.34	Minimum power gait at ω_{bio} for Atlantic radial grid.	112
6.35	Minimum power gait for Butterfly rectangular grid.	113
6.36	Minimum power gait at ω_{bio} for Butterfly rectangular grid.	113
6.37	Minimum power gait for Cownose rectangular grid (symmetric constraint).	114

6.38	Minimum power gait at $\omega_{b_{10}}$ for Cownose rectangular grid (symmetric constraint).	114
6.39	Minimum power gait for Cownose radial grid.	115
6.40	Minimum power gait at $\omega_{b_{10}}$ for Cownose radial grid.	115
6.41	Minimum power gait for Cownose radial shifted grid (symmetric constraint).	116
6.42	Minimum power gait at $\omega_{b_{10}}$ for Cownose radial shifted grid (symmetric constraint).	116
6.43	Minimum actuation rate gait for Atlantic rectangular grid.	117
6.44	Minimum actuation rate gait at $\omega_{b_{10}}$ for Atlantic rectangular grid.	117
6.45	Minimum actuation rate gait for Atlantic radial grid.	118
6.46	Minimum actuation rate gait at $\omega_{b_{10}}$ for Atlantic radial grid.	118
6.47	Minimum actuation rate gait for Butterfly rectangular grid.	119
6.48	Minimum actuation rate gait at $\omega_{b_{10}}$ for Butterfly rectangular grid.	119
6.49	Minimum actuation rate gait for Cownose rectangular grid (symmetric constraint).	120
6.50	Minimum actuation rate gait at $\omega_{b_{10}}$ for Cownose rectangular grid (symmetric constraint).	120
6.51	Minimum actuation rate gait for Cownose radial grid.	121
6.52	Minimum actuation rate gait at $\omega_{b_{10}}$ for Cownose radial grid.	121
6.53	Minimum actuation rate gait for Cownose radial shifted grid (symmetric constraint).	122
6.54	Minimum actuation rate gait at $\omega_{b_{10}}$ for Cownose radial shifted grid (symmetric constraint).	122

List of Tables

3.1	Objective functions specified by Π	25
3.2	Optimal parameters for SMR locomotion	36
3.3	Optimal frequencies [rad/s] and simulated velocities [mm/s]	46
4.1	Starting joint positions and point mass counts for rectangular wing grids. . .	57
4.2	Starting joint positions, point mass counts, and row angles for radial wing grids.	58
4.3	Thickness function coefficients.	60
4.4	Observed gait metrics	62
4.5	Basic gait wing phase lags.	66
6.1	Atlantic thickness measurements, cm	90
6.2	y-positions of Atlantic thickness measurements, mm	90
6.3	Butterfly thickness measurements, cm	90
6.4	y-positions of Butterfly thickness measurements, mm	91
6.5	Cownose thickness measurements, cm	91
6.6	y-positions of Cownose thickness measurements, mm	91
6.7	Undamped natural frequencies.	98
6.8	Optimal gaits for the Atlantic ray, rectangular grid.	123
6.9	Optimal gaits for the Atlantic ray, radial grid.	123
6.10	Optimal gaits for the Atlantic ray, rectangular grid, observed ω	123

6.11	Optimal gaits for the Atlantic ray, radial grid, observed ω	123
6.12	Optimal gaits for the Butterfly ray, rectangular grid.	124
6.13	Optimal gaits for the Butterfly ray, rectangular grid, observed ω	124
6.14	Optimal gaits for the Cownose ray, rectangular grid (symmetric).	124
6.15	Optimal gaits for the Cownose ray, radial grid.	124
6.16	Optimal gaits for the Cownose ray, shifted radial grid (symmetric).	125
6.17	Optimal gaits for the Cownose ray, rectangular grid (symmetric), observed ω	125
6.18	Optimal gaits for the Cownose ray, radial grid, observed ω	125
6.19	Optimal gaits for the Cownose ray, shifted radial grid (symmetric), observed ω	125

List of Symbols

A	Affine environmental force matrix
A_b	Flapping-wing rectifier body area
a_i	Entry of matrix Q in the (i, i) location
a_b	Flapping-wing rectifier body drag coefficient
B	Actuation matrix
C	Coriolis and centrifugal matrix
\mathbb{C}	Complex set
c	Flapping-wing rectifier wing curvatures; Friction coefficients
D	Damping matrix
d	Body damping; Flapping-wing rectifier wing grid spacing
E	Elastic energy
e	2.7182818284590452353602874713526624; Vector of ones
e_i	Vector whose i^{th} entry is one and zero otherwise
F	Linear combination of proper transfer functions and differentiators
f	Vector of environmental forces; Minimum eigenvalue of Z
g	Net gravity (buoyancy) vector
h	Highest order harmonic
J	Inertia matrix

j	Imaginary number $\sqrt{-1}$
K	Stiffness matrix
k	Upper bound on integer set; body stiffness
L	Langrangian; Linearized environmental force matrix
\mathbb{L}	Set of feasible optimal gait generalized eigenvalues
ℓ	Number of actuators
m	Total mass of the system
m_i	Mass of flapping-wing rectifier point mass i
N	Center of mass velocity to environment frame transformation matrix
n	Dimension of generalized coordinates or forces; Surface normal vector
P	Harmonic balance system (shape and orientation) matrix
P_n	Surface normal projection matrix
\mathbb{P}	T -periodic, unbiased, continuously differentiable, scalar or vector function
p	Number of spatial dimensions (1, 2, or 3)
Q	Quadratic environmental force matrix
q	Generalized coordinates
R	Local shape velocity frame to environment frame transform; Rotation matrix
\mathbb{R}	Real set
r	Vector of cartesian coordinates
r_b	Cartesian coordinates of the flapping-wing rectifier main body
S	Thrust matrix, skew-symmetric part of Λ
T	Period of oscillation; Kinetic energy;
T_c	Curvature matrix
t	Flapping-wing rectifier wing thickness
u	Applied acutation input

V	Potential energy
\mathbb{V}	Direction of locomotion
v	Locomotion speed, Flapping-wing rectifier surface velocity
v_y	Flapping-wing rectifier center of mass steady-state velocity
v_z	Flapping-wing rectifier approximate surface normal velocity operating range
v_o	General locomotion velocity
W	Virtual work; Shape variable coefficient matrix
w	Global center of mass position vector
w_b	Flapping-wing rectifier body width
X	Harmonic balance reformulation objective matrix
Y	Harmonic balance reformulation constraint matrix
y	T -periodic steady state response
Z	$X - \lambda Y$
\mathbb{Z}	Positive integers
z	Test vector in optimal gait solution
α	Average thrust
α_b	Yaw of the flapping-wing rectifier main body
β	Objective function weighting parameter
β_b	Roll of the flapping-wing rectifier main body
γ	Environmental force function; Minimum objective value
γ_b	Pitch of the flapping-wing rectifier main body
ϵ	Infinitesimal value
η	Nominal posture
θ	Vector of local shape and orientation variables
ϑ	Periodic body motion about the nominal posture

Λ	Linear environmental force coefficient matrix
λ	Eigenvalues
μ	Input signal; Dissipative force function; Viscosity of water
Π	Objective transfer function matrix
\mathbb{I}	Set of transfer functions
π	3.14159265358979323846264338327950
ρ	Density of water
ϕ	Actuator displacements (i.e. joint angles)
ϕ_b	Orientation variables of the flapping-wing rectifier main body
φ	Vector of relative displacements for dissipative forces (i.e. joint angles)
Ψ	Constant Hermitian matrix
ψ	Generalized forces
Ω	Rotation matrix
ω	Frequency of Oscillation

Chapter 1

Introduction

1.1 Overview

Currently, there are a number of situations in which existing machines for transportation, from wheeled terrestrial vehicles to airplanes and submarines, are poorly suited for various reasons. Most importantly, they lack the ability to adapt to rough or varying terrain to maintain a forward velocity, and lack the agility to maneuver in confined terrain. A potential solution to the problem is the design of robotic systems utilizing various forms of animal locomotion. For instance, undulatory locomotion of slender animals (e.g., snake crawling, leech swimming) seems especially well suited for adapting to various terrains, while flapping locomotion of winged animals achieves agility. In the case of underwater vehicles, the winged propulsion of manta rays seems particularly advantageous, possessing an agile, silent, efficient locomotion while possessing a large central body cavity which seems particularly well suited for the transportation of a payload. In addition, the mechanisms of animal locomotion may provide a framework for designing a robotic locomotor capable of robustly maintaining velocity under an optimal condition with respect to a given criterion such as power efficiency, adaptively changing propulsion strategy as the surrounding environment changes.

Animal locomotion may be viewed as a process of mechanical rectification [1, 2] in which a periodic body motion is converted to sustained thrust force through dynamic interactions with the environment. A specific motion pattern (or “gait”) is chosen by each animal, depending upon the given environment, desired locomotion speed and range, disability conditions on the body (such as under-actuation), and other factors [3–6]. A fundamental problem in designing robotic locomotors, as well as in understanding animal locomotion mechanisms, is to determine a gait for the given mechanical system that optimizes a quantity representing the cost and/or performance (such as input energy), while maintaining a desired velocity.

This dissertation includes previously published papers on this topic. Conference papers have appeared in [7, 8], where optimal gaits were sought over the set of harmonic signals and solutions were given without details of proofs. The journal paper in [9] extends these previous results to the case of general periodic signals and provides complete proofs with derivations of the general rectifier equations. Conference paper [10] discusses the derivation of a flapping-wing rectifier and the associated optimal gaits.

1.2 Relation to the current state of knowledge

1.2.1 Optimality of animal locomotion

Early biological studies focus on the energetic cost of locomotion for specific animals. For example, Hoyt and Taylor, based on the observation that horses naturally choose to trot at low speeds and gallop at high speeds, examine in [3] the metabolic energy cost (defined as O_2 consumption per kilogram-meter) as locomotion speed is varied. They find that for each gait type (i.e. walking, trotting, and galloping), horses naturally choose to run at a narrow band of speeds located around the associated local minima for metabolic energy cost. Likewise, Pennycuik shows in [11] that the gnu and other animals also possess similar attributes. These findings are not surprising, as the cost of locomotion for various

animals can be a large part of their daily energetic needs [12]. This is shown for many terrestrial mammals in studies by Garland [13], Girard [14], and Corp et al. [15]. Likewise, Christian et al. [16] and Drent et al. [17] show this for lizards, and Ginneken et al. [18] shows this for eels during long-distance migration.

Biologists have also widely hypothesized that gait transitions occur to maintain a minimum metabolic cost as locomotion speed is varied (an *energetic* trigger for gait transition) [19]. Examples of this hypothesis can be found in [3, 20–25]. Other studies dispute this hypothesis, finding that there are *mechanical* triggers which cause gait transition. Farley and Taylor show in [26] that horses change gaits when musculoskeletal forces reach a critical level. Hreljac shows in [19] that the gait transition during human locomotion is also not an energy saving mechanism. Additionally, he shows in [27] that human gait selection is subject to kinematic factors such as maximum ankle angular velocity. More recently, there have been additional studies examining more abstract triggers. For example, Kram et al. show in [28] that the walk-run transition in humans is triggered by the dynamics of an inverted-pendulum system, occurring at a nearly constant Froude number, while Diedrich and Warren, Jr. show in [4] that gait transitions behave like non-equilibrium phase transitions between attractors which occur near the energy separatrix.

These biological studies show that many animals possess a combination of body design, gait choice, and locomotion speed that possess a large degree of optimality with respect to energy cost of locomotion, subject to various constraints that are assumed to limit structural wear and damage. Such animals would therefore be appropriate for the design of efficient robotic vehicles based on animal locomotion mechanisms.

1.2.2 Biologically inspired locomotors

Engineers have been attempting to develop legged walking robots for over 40 years in order to design vehicles that can move easily over rough, irregular, inaccessible, or dangerous terrain [29, 30]. Delcomyn provides in [30] a thorough summary of insect-based

walking robots that have been designed toward this goal. Some early designs were simple robots with single-segment legs with limited movements [31, 32]. More recently, robots have been developed with legs more closely matching the leg structure of real insects to utilize the advantages such structures may have for traversing difficult terrain, such as stick insects [33, 34] and cockroaches [35, 36]. An excellent example of an insect-based robot overcoming difficult terrain is the eight-legged robot named Dante II, which was successfully used to explore an active volcano [37].

Similarly, various robots mimicking marine animals have been designed for the aquatic environment with the goal of improving performance parameters such as propulsive efficiency, maneuverability, and stationary stability in the presence of large perturbations [38, 39]. Yu et al. provide in [39] the design, construction, and control issues of a robotic dolphin that has the potential to achieve many of these goals, as well as a list of other successful biomimetic robots including well known robots based on fish from MIT (RoboTuna and RoboPike), Draper Laboratory (VCUUV), and Mitsubishi [40–42], lamprey robots [43], the robotic Blackbass [44], a two-joint dolphin robot [45], and link-based robotic fish [46]. Additionally, the design of micro-scale swimming robots is of interest due to such demands as the maintenance of factory pipelines and delicate internal surgical operations and diagnosis, and to advances in the precise process technology needed for fabrication [47]. Guo et al. describe in [47] an underwater fish-like micro robot utilizing an ionic conducting polymer film for the actuator. He also provides a list of several existing fish-like micro robots using other materials such as shape memory alloy (SMA) actuators, GMA actuators, piezoelectric (PZT) actuators, and polymer actuators, with each design boasting unique advantages and disadvantages [48–53]. Thus, a large array of robotic locomotors have been designed and built, with each demonstrating varying advantages over the current wheeled, screwed, and jet-engine vehicles.

1.2.3 Locomotor models

Dynamical models are important for understanding biological mechanisms as well as for fine tuning the robotic locomotor design. In the design of the biologically inspired locomotors in the previous section and the optimal gaits for robotic locomotors in the following section, many different models are developed for each unique system. Among the many complexities, assumptions, and simplifications included in the various models are numerous nonlinearities (from such sources as fluid dynamic models, friction models, and material properties, just to name a few), non-slip contacts or other non-holonomic constraints, or planar assumptions.

The general principles underlying animal locomotion have been compiled in various reviews [54, 55], illustrating important principles such as common structural properties, gait characteristics, control systems, and the generation of thrust through reaction forces produced by interaction of an animal's body with the environment. The proposed research will encapsulate such principles in a general, three dimensional, unified model for locomotion of animal systems which produce thrust through periodic motion in the presence of a surrounding environment, such as swimming fish, crawling snakes, or flying birds.

1.2.4 Optimal gaits for robotic locomotors

Optimal gaits have been investigated in the literature on robotic locomotors. One approach is based on biological inspirations, wherein a particular gait, observed in animal locomotion, is parameterized and examined for optimality with respect to a cost function. Optimizations are typically performed via gridding of the parameter space and numerical simulations. This type of approach has been taken to search for optimal gaits for robots that mimic human walking [56], snake crawling [57], and anguilliform swimming [58]. Methods such as these might obtain an optimal parameter set within the particular gait examined, but may miss globally optimal gaits that differ from what is observed in biology.

Other approaches to find optimal gaits are based on some standard formulations of

optimal control problems and various combinations of existing optimization methods. A popular method is to expand the signals over a finite set of basis functions, reducing the problem to a parametric optimization. Reference [59] used this method to find an optimal gait for eel swimming, where the necessary condition for optimality was solved using Newton iteration. This method is also used for biped walking with the aid of sequential quadratic programming [60, 61]. Another well known method is to apply the calculus of variations to reduce the optimization to a two-point boundary-value problem. This method has been used by [62] for nonholonomic locomotion systems, by [63] for a seven-link biped robot, and by [64] for shape actuated locomotion systems. While it would be ideal to have global solutions to general optimal control problems, most, if not all, of the currently available methods guarantee local optimality at best. This means that the solution depends on the initial condition of the numerical search in general, and hence can be far from the global optimum.

In this dissertation, we take a different approach, focusing on systems which are in continual contact with the environment (including swimming and slithering, but excluding walking). Instead of searching for locally optimal gaits for a fully nonlinear model of a locomotor system, we will first simplify the model through techniques such as Taylor series and describing function, and then develop a method for finding globally optimal gaits. In this way, potential sub optimality is not hidden behind the numerical optimization procedure, but is explicit in the problem formulation. The optimal gait for the simplified model could then be used as an initial condition in a local optimization for the original model. Thus, our method can be viewed as a complement to, rather than a replacement of, existing local optimization methods. The process to compute our solution is extremely fast and numerically stable. Hence, it can be applied to hyper-redundant rectifier systems with many degrees of freedom. Another advantage is that an optimal gait is found within those achievable by the given set of actuators. This feature is especially important for under actuated systems that have less actuators than the number of shape variables because not

all gaits are achievable by a small number of actuators. In summary, most existing methods are local and/or rely on numerical iterative searches and hence their solutions can be far from optimum.

1.2.5 Application of batoids to underwater vehicles

Batoids seem particularly well suited for the design of underwater vehicles, based on many factors. First, the general shape of rays, with a relatively large central body cavity, mostly stationary between the undulating propulsive wings, seems particularly well suited for the classic localized design often seen in existing vehicles. Second, the wide variety of batoid sizes provide options for many desired purposes, from small Atlantic ray based vehicles for investigating tiny crevices to very large Manta ray based vehicles for carrying large payloads. Manta rays in particular are expected to be very efficient for locomotion, due to their large size. This is based on two arguments, the first of which being research that shows that larger animals have greater metabolic efficiency than smaller animals (both at rest and during locomotion) [65]. The second argument is based on the explanation by Heine [66] that flapping rays such as the manta are extremely active, spending their time constantly swimming and regularly undergoing long migrations. Such active behavior suggests that their structure is well optimized for efficient swimming.

1.2.6 Biology of batoids and related modeling research

A detailed paper by Schaefer and Summers [67] shows that the skeletal structure of a batoid's wing is related to the type of swimming that a ray uses. Additionally, Rosenberger explains in [68] that the various types of pectoral fin based locomotion in batoids has been divided traditionally into two categories: undulation, termed "rajiform" locomotion [69], and oscillation, termed "mobuliform" locomotion [70]. Undulation is defined by having a wave number greater than 1.0 along the fin during swimming. Oscillation is similar to flapping in birds, possessing a wave number of less than 0.5 along the fin, and is the mode

of locomotion employed by manta rays. Rays that swim by undulation are generally sedentary and possess wing spans roughly less than or equal to their body length, while rays that swim by oscillation are very active, with wing spans larger than their body length [66].

To gather enough data to create an accurate model for batoid swimming, multiple studies of various species are considered and appropriate parameters are determined. The need for varied data is due to the rarity of existing biological studies of rays, in addition to the tendency of such studies to focus on many biological and behavioral aspects that are not clearly useful for the design of batoid based underwater vehicles. A recent thesis by Forch [71] provides a summary of the sparse research on manta rays, explaining that the rarity is a result of the difficulty to keep mantas in captivity due to their large size, while controlled studies are also difficult to perform in the wild. References used to establish suitable model parameters for his model include [66, 72–78]. In his thesis, Forch creates a simple model of a manta ray with many simplifying assumptions, such as symmetric wings, a body constrained to move only in the forward direction, and a wing consisting of point masses constrained to only move up and down relative to the body. This dissertation develops a more realistic model of batoid swimming, with a full 6 degree-of-freedom body with independent wings, which more closely agrees with actual batoids. Additionally, we focus on smaller ray species with more readily available data, which are currently being investigated by Fish [79] and Russo [80]. Similar to this dissertation, Russo is attempting to determine the relationship between wing structure and observed biological gait. His approach is closer to an inverse optimal control problem, where the objective is determined given the optimal gait and mechanical system, by performing a numerical perturbation analysis of the wing structure while imposing the observed gait and measuring various quantities of interest (such as wing tissue strain), while this dissertation follows the traditional optimal control framework: Given the system and objective function, determine the optimal gait.

1.3 Objectives

This dissertation establishes a new framework for control theory that enables efficient locomotion of robotic systems and gains a deeper understanding of biological locomotion mechanisms. Specifically, we develop a systematic method for determining optimal gaits for a general class of locomotor systems, and uncover design principles underlying efficient swimming of batoid fish (rays). We first define a general class of mechanical rectifiers which capture the essential dynamics of animal locomotion, develop equations of motion, and then approximate the system by assuming small perturbations around a nominal posture. It turns out that a linear approximation fails to capture the rectifying dynamics; the simplest model should contain a bilinear term of the shape variables and their derivatives.

We then formulate an optimal gait problem for the bilinear rectifier model, where a quadratic cost function is minimized over the set of periodic body movements achievable by control inputs, subject to an equality constraint on the average locomotion velocity. The problem belongs to the class of infinite dimensional nonconvex problems that are extremely difficult in general. However, our result reveals that a globally optimal gait is purely sinusoidal, and can be found by calculating the generalized eigenvalues of a pair of Hermitian matrices and by sweeping over the frequency. We verify the optimization process through case studies of multilink locomotors, which is a mechanical rectifier formed as a chain of multiple links subject to environmental forces with directional preference. We demonstrate that natural gaits similar to those observed in animal locomotion can be found, without any *a priori* assumptions, through minimization of such cost functions as input power, rate of shape change, and torque derivative. In particular, undulatory gaits similar to snake crawling or leech/lamprey swimming are found to be optimal if the nominal posture is straight, while flapping gaits observed in jellyfish-like animals are optimal if the nominal posture is curved. We also examine the effects of approximations employed in the problem formulation through simulations of the bilinear and fully-nonlinear rectifier equations. Additionally, we consider a disk-mass system that captures the rectifying dynamics in the

simplest manner. Analytical expressions of optimal gaits are obtained for this simple case, and are used to make some general observations through analogy to more complex rectifiers, suggesting how system parameters affect the gait.

Finally, we examine bird or fish-like systems which are in constant contact with the surrounding environment and locomote primarily through the periodic motion of wings (or fins), which we call “flapping-wing” rectifiers. We assume a simple point mass model for the wing geometry, and allow independent wing motion and body translation and rotation, and examine the effects of various wing shapes and optimality criteria on gait selection. We show that the bilinear thrust term has a strong influence on gait selection by comparing the basic efficient gait (which maximizes the ratio of the thrust to wing deflection) with other optimal gait results through gait snapshot, amplitude, and phase plots. We find that a long, high-aspect-ratio wing results in an oscillatory (flapping) gait while a short, low-aspect-ratio wing results in an undulatory gait. We observe both symmetric and anti-symmetric optimal gaits, depending on a combination of objective function, frequency, and wing shape, through the excitation of various natural modes. We find that the minimum curvature and minimum power gaits are most similar to the observed biological gaits, possessing similar tip amplitudes and oscillation frequencies, however with lower phase lags, resulting in generally more oscillatory shapes.

1.4 Notation

The sets of n by m real and complex matrices are denoted by $\mathbb{R}^{n \times m}$ and $\mathbb{C}^{n \times m}$, respectively, where the dimensional notation is omitted if $m = 1$ or $n = m = 1$. The set of positive real numbers is \mathbb{R}_+ . The set of positive integers is denoted by \mathbb{Z} , and its subset up to k by \mathbb{Z}_k . Let $\mathbb{Z}_\infty := \mathbb{Z} \cup \{\infty\}$. For matrices M_i with $i \in \mathbb{Z}_k$, the matrix obtained by stacking them in a column is denoted by $\text{col}(M_1, \dots, M_k)$, and we use $\text{diag}(M_1, \dots, M_k)$ if they are stacked on the diagonal. When the argument is a single vector v , $\text{diag}(v)$ is the diagonal

matrix whose i^{th} diagonal entry is v_i . For a complex matrix M , its transpose, complex conjugate transpose, and real part are denoted by M^T , M^* , and $\Re[M]$, respectively. For a generic function $F(x)$ and $h \in \mathbb{Z}_\infty$, define

$$F^h(x) := \text{diag}(F(x), F(2x), \dots, F(hx)).$$

If F is a constant matrix, F^h is the block diagonal matrix having F repeated h times on the diagonal. For a differentiable mapping $f : \mathbb{R}^n \rightarrow \mathbb{R}^m$ of variable $x \in \mathbb{R}^n$, its partial derivative $\partial f / \partial x$ is the $n \times m$ matrix with (i, j) entry $\partial f_j / \partial x_i$.

The set of all T -periodic, unbiased, continuously differentiable, possibly vector-valued functions is denoted by \mathbb{P}_T . For $h \in \mathbb{Z}$, the finite dimensional subspace of \mathbb{P}_T spanned by harmonics up to the h^{th} order is denoted by \mathbb{P}_T^h . For consistency, we also define $\mathbb{P}_T^\infty := \mathbb{P}_T$. The phasor \hat{x} of $x \in \mathbb{P}_T^h$ with $h \in \mathbb{Z}_\infty$ is defined by the coefficients of the complex Fourier series as follows:

$$x(t) = \sum_{k=1}^h \Re [\hat{x}_k e^{j\omega kt}], \quad \hat{x} := \text{col}(\hat{x}_1, \hat{x}_2, \dots, \hat{x}_h),$$

where $\omega := 2\pi/T$, and \hat{x}_k is called the k^{th} phasor of x . Let \mathbb{II} be the set of transfer functions $\Pi(s)$ of the form $\Pi(s) = F(-s)^T \Psi F(s)$, where Ψ is a constant Hermitian matrix and $F(s)$ is a linear combination of stable (proper) transfer functions and differentiators. If an input $\mu \in \mathbb{P}_T$ is applied to $F(s)$, the output is given by $y + \tilde{y}$ where y is the steady state response that is T -periodic, and \tilde{y} is the transient response that eventually dies out. With a slight abuse of notation, we denote the T -periodic signal $y^T \Psi y$ by $\mu^T \overset{\circ}{\Pi} \mu$. This notation is motivated by the fact (see Lemma 6 in Appendix 6.1) that the average value of $y^T \Psi y$ over a cycle is given by $\hat{\mu}^* \Pi(j\omega) \hat{\mu} / 2$ when μ is sinusoidal (i.e. $\mu \in \mathbb{P}_T^1$).

Chapter 2

General Framework for Animal Locomotion

2.1 Mechanical rectifier systems

Consider a multi-body mechanical system placed in an environment of up to three spatial dimensions. The bodies are rigid, and are connected to each other through rigid or flexible mechanisms (e.g., rotational joints as in manipulator arms [81], and flexible wires as in tensegrity structures [82,83]). The system is equipped with actuators, each of which generates a local input force that acts between bodies, and produces no global thrust with respect to the environment. For example, motors may drive joints and linear actuators may push and pull links relative to one another, but there are no jet engines. The motion of the bodies produce interactive forces and torques from the environment, and when periodic motion can result in a net thrust due to those interactive forces, we call the system a *mechanical rectifier* [84, 85].

We restrict our attention to systems that *continually* interact with the environment. This excludes systems such as walking robots but still includes a wide range of other animal locomotions, such as swimming, crawling (as in snakes), and flying. The multilink robot

inspired by swimming frogs, depicted in Fig. 2.1, is one such example.

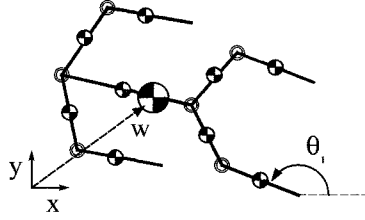


Figure 2.1: Multilink swimming system

The following sections first develop equations of motion for a general class of mechanical rectifiers in up to three spatial dimensions, then derive an approximate quadratic system that captures and reveals the mechanism of rectification.

2.1.1 General equations of motion

To derive the equations of motion for a general multibody rectifier system, we begin with the well known Euler-Lagrange equation:

$$\frac{d}{dt} \left(\frac{\partial L}{\partial \dot{q}} \right) - \frac{\partial L}{\partial q} = \psi, \quad (2.1)$$

where $q(t) \in \mathbb{R}^n$ are the generalized coordinates, $\psi(t) \in \mathbb{R}^n$ are the generalized forces, and $L(q, \dot{q}) := T - V \in \mathbb{R}$ is the difference between the kinetic energy $T(q, \dot{q})$ and the potential energy $V(q)$. The generalized force ψ is defined by

$$\delta W = (\delta q)^T \psi, \quad (2.2)$$

where δW is the virtual work done by external forces and torques, and δq is the virtual displacement in generalized coordinates. Let us split the generalized coordinates q into

two parts:

$$q = \begin{bmatrix} \theta \\ w \end{bmatrix},$$

where $w(t) \in \mathbb{R}^p$ is the global position vector for the center of mass of the system relative to the environment (the spatial dimension is $p = 1, 2,$ or 3), and $\theta(t) \in \mathbb{R}^n$ contains the variables specifying the local shape and global orientation of the bodies. It is assumed that the kinetic energy T and potential energy V are given by

$$T = \frac{1}{2} \left(\dot{\theta}^\top J(\theta) \dot{\theta} + m \dot{w}^\top \dot{w} \right), \quad V = E(\theta) + mg^\top w,$$

where $J(\theta)$ is the inertia matrix, m is the total mass of the system, $E(\theta)$ is the elastic energy stored in the system, and g is the net gravity (buoyancy) vector. We consider the case where the generalized force consists of environmental forces, actuator inputs, and dissipative effects such as joint frictions.

Assembling all the generalized forces (details will be given in the next section) and exploiting the structures of the kinetic and potential energies, the equations of motion for general rectifier systems are given by the following form:

$$\begin{aligned} J(\theta)\ddot{\theta} + C(\theta, \dot{\theta})\dot{\theta} + k(\theta) + d(\theta, \dot{\theta}) \\ + R(\theta)^\top \gamma(R(\theta)\dot{\theta} + N(\theta)\dot{w}) = B(\theta)u, \\ m\ddot{w} + mg + N(\theta)^\top \gamma(R(\theta)\dot{\theta} + N(\theta)\dot{w}) = 0, \end{aligned} \tag{2.3}$$

where the terms $J(\theta)\ddot{\theta} + C(\theta, \dot{\theta})\dot{\theta}$ and $m\ddot{w}$ are the inertial torques and forces, $k(\theta) + d(\theta, \dot{\theta})$ are the torques due to body stiffness and damping, $u(t) \in \mathbb{R}^\ell$ is the applied input, the terms involving γ capture the effect of environmental forces, and

$$C(\theta, \dot{\theta}) := \left(\frac{\partial J(\theta)\dot{\theta}}{\partial \theta} \right)^\top - \frac{1}{2} \left(\frac{\partial J(\theta)\dot{\theta}}{\partial \theta} \right), \quad k(\theta) := \frac{\partial E(\theta)}{\partial \theta}.$$

The quantity $R(\theta)\dot{\theta} + N(\theta)\dot{w}$ is the vector of link velocities in the body coordinates, relative to the environment. The function $\gamma : \mathbb{R}^\sigma \rightarrow \mathbb{R}^\sigma$ is a possibly nonlinear mapping that generates the forces and torques resulting from the relative motion. Typically, γ satisfies the sector condition $y_i x_i \geq 0$ for each entry of the input/output pair $y = \gamma(x)$. We see from (2.3) that the applied input u changes the shape and orientation θ , which in turn drives the global position w through interactions with the environment. In particular, a periodic motion θ , generated by a periodic input u via the first equation, can be rectified through the second equation to result in a “locomotion” with velocity \dot{w} .

2.1.2 Derivation of the generalized force

We now provide a detailed derivation of the generalized force ψ that leads to terms in (2.3). Specifically, we will derive the three terms in $\psi = \psi_e + \psi_a + \psi_d$ where ψ_e is the environmental force, ψ_a is the actuator force, and ψ_d is the dissipative force, respectively. In the development, “forces” are meant to include both linear forces and rotational torques, and similar generalizations apply to “displacements,” “velocities,” and “coordinates.”

Environmental forces

We assume that the effect of the environmental forces on the system can be approximately represented by forces acting on a finite number of points on the bodies. Let r be a vector indicating the Cartesian coordinates of such points, and f be the corresponding vector of forces acting on them. The velocity of the points relative to the environment, \dot{r} , can be expressed as $\Omega(\theta)\dot{r}$ in the body coordinates, where $\Omega(\theta)$ is the rotation matrix that transforms a vector from the inertial frame to the body frame. Assume that the environmental force is a (possibly nonlinear) function of the relative velocity and is given by $-\gamma(\Omega(\theta)\dot{r})$ in the body frame. Transforming it back to the inertial frame, the environmental force is given by

$$f = -\Omega(\theta)^\top \gamma(\Omega(\theta)\dot{r}). \quad (2.4)$$

Note that the Cartesian coordinates r are linear in w . In fact, it would have the form $r(q) = \rho(w) + \epsilon(\theta)$ for some functions ρ and ϵ where the former is linear. We then have

$$\dot{r} = \left(\frac{\partial r}{\partial \theta} \right)^\top \dot{\theta} + \left(\frac{\partial r}{\partial w} \right)^\top \dot{w}$$

where the coefficient of \dot{w} is constant. The virtual work done by the environmental force is $\delta W_e = (\delta r)^\top f = (\delta q)^\top \psi_e$, from which we obtain the corresponding generalized force

$$\psi_e = \frac{\partial r}{\partial q} f = - \begin{bmatrix} R(\theta)^\top \\ N(\theta)^\top \end{bmatrix} \gamma(R(\theta)\dot{\theta} + N(\theta)\dot{w}),$$

where

$$R(\theta) := \Omega(\theta) \left(\frac{\partial r}{\partial \theta} \right)^\top, \quad N(\theta) := \Omega(\theta) \left(\frac{\partial r}{\partial w} \right)^\top.$$

Actuator forces

Let ϕ_i be the displacement of the i^{th} actuator, e.g., the joint angle driven by a rotary motor or displacement of a linear motor, and let u_i be the force or torque generated. Define $\phi \in \mathbb{R}^\ell$ and $u \in \mathbb{R}^\ell$ by stacking ϕ_i and u_i in columns where ℓ is the number of actuators. Suppose that ϕ is a differentiable function of θ , and is independent of w due to the assumption that all actuators are local, only generating forces/torques between bodies. The virtual work done by the actuators is

$$\delta W_a = (\delta \phi)^\top u = (\delta \theta)^\top \frac{\partial \phi}{\partial \theta} u.$$

Hence, from (2.2), the generalized forces due to the actuators are given by

$$\psi_a = \begin{bmatrix} B(\theta)u \\ 0 \end{bmatrix}, \quad B(\theta) := \frac{\partial \phi}{\partial \theta}.$$

Note that $B(\theta)$ is a constant matrix if ϕ is a linear function of θ , which is the case when, e.g., θ contains all the joint angles and ϕ consists of those actuated. The matrix $B(\theta)$ depends on θ in general, as is the case if a body is driven by a linear actuator attached to another body, similar to skeletal muscles.

Dissipative forces

Let φ be the vector of relative displacements of two bodies between which dissipative forces like frictions exist. The variable φ is a function of θ , but not w , for the dissipation effect due to the interactions with the environment is captured within the environmental force. Let us assume that the dissipative forces experienced through displacement φ is a differentiable function of $\dot{\varphi}$, denoted by $-\mu(\dot{\varphi})$. Typically, the function μ is a diagonal mapping such that each diagonal entry satisfies the sector condition $\mu_i(\dot{\varphi}_i)\dot{\varphi}_i > 0$. The virtual work done by the dissipative forces is

$$\delta W_d = -(\delta\varphi)^\top \mu(\dot{\varphi}) = -(\delta\theta)^\top \frac{\partial \varphi}{\partial \theta} \mu \left(\left(\frac{\partial \varphi}{\partial \theta} \right)^\top \dot{\theta} \right),$$

from which we obtain the associated generalized forces

$$\phi_d = \begin{bmatrix} -d(\theta, \dot{\theta}) \\ 0 \end{bmatrix}, \quad d(\theta, \dot{\theta}) := \frac{\partial \varphi}{\partial \theta} \mu \left(\left(\frac{\partial \varphi}{\partial \theta} \right)^\top \dot{\theta} \right).$$

If μ represents linear (viscous) damping, then the generalized forces have the form $d(\theta, \dot{\theta}) = D(\theta)\dot{\theta}$ for some positive (semi)definite matrix $D(\theta)$. If φ is a linear function of θ (e.g. joint angles), then $d(\theta, \dot{\theta})$ becomes independent of θ .

2.2 Mechanisms underlying thrust generation

To gain insight into the locomotion mechanism of rectifier systems, we attempt to analyze the behavior of the rectifier (2.3) through the simplest approximate model that captures the essential dynamics of rectification. This section develops such a simple model and reveals the mechanism underlying rectification of periodic body motion θ to yield global velocity \dot{w} . In the rest of this dissertation, we consider for simplicity the case where the effect of the gravity potential can be neglected (swimming of a neutrally buoyant system, crawling on the horizontal plane, etc.), and set $g = 0$ in (2.3).

2.2.1 Nominal posture and approximation

Many biological systems are observed to take a particular posture for relaxed cruising between active locomotion phases. For instance, a fish cruises with a straight body posture, while a ray cruises with a posture resembling a fixed-wing aircraft. Motivated by these cruising postures, we introduce the notion of a *nominal posture*. A posture of the rectifier specified by the shape and orientation $\theta(t) = \eta \in \mathbb{R}^n$ is said to be nominal at velocity $\dot{w}(t) = v_o \in \mathbb{R}^p$ if

$$\begin{aligned} R(\eta)^\top \gamma(N(\eta)v_o) + k(\eta) &= 0, \\ \delta := N(\eta)^\top \gamma(N(\eta)v_o) &\in \mathbb{V}, \end{aligned} \tag{2.5}$$

where \mathbb{V} is the straight line in \mathbb{R}^p that is parallel to v_o and passes through the origin, indicating the direction of locomotion. Condition (2.5) means that if the rectifier takes a nominal posture η at velocity v_o and receives a (fictitious) external force in the direction of v_o to balance out the environmental drag δ , then the locomotion velocity and body shape/orientation are simultaneously maintained, i.e., $\dot{w}(t) \equiv v_o$ and $\theta(t) \equiv \eta$, in the absence of any actuating input u . Certain periodic body motion θ about a nominal posture η , generated by actuator input u , is expected to produce the necessary thrust for the system that balances out the drag and maintains locomotion at the average velocity v_o . Throughout the dissertation, we

choose the global coordinate frame so that its first axis is aligned with \mathbb{V} , that is, $v_o = \nu e_1$ for some $\nu \in \mathbb{R}$ where $e_i \in \mathbb{R}^p$ is the vector whose i^{th} entry is one and the others are zero.

We now consider a periodic body motion $\theta(t)$ about a nominal posture η at velocity v_o , and assume that small oscillation of $\vartheta(t) := \theta(t) - \eta$ maintains the locomotion velocity $\dot{w}(t)$ near v_o . To simplify the equations of motion in (2.3), we first linearize the environmental force function γ using the Taylor series (slope at a nominal operating point) or the describing function (average slope in the operating region) [86]. While such approximation could introduce a potentially large error in general, qualitative characteristics of the environmental forces, that are important for shaping the gait, may be captured. For instance, anisotropy of normal and tangential forces, which is known to be essential for undulatory locomotion [57, 87, 88], can be well captured by linear models [57, 89]. For further simplification, the nonlinear equations of motion in (2.3) may be linearized by expanding each expression into its Taylor series in terms of ϑ , and keeping up to the first order terms. However, as shown shortly, the essential dynamics for rectification turns out to be embedded in the second or higher order terms in the second equation of (2.3), and hence the linearized model fails to capture the locomotion dynamics. For this reason, we choose to linearize the first equation in terms of ϑ but keep up to the second order terms in the second equation. In particular, we make the following approximations:

$$\begin{bmatrix} R(\theta)^\top \\ N(\theta)^\top \end{bmatrix} \gamma(R(\theta)\dot{\theta} + N(\theta)\dot{w}) \cong \begin{bmatrix} D_1 & A(\vartheta) \\ A(\vartheta)^\top & Q(\vartheta) \end{bmatrix} \begin{bmatrix} \dot{\vartheta} \\ \dot{w} \end{bmatrix},$$

$$J(\theta) \cong J(\eta) =: J, \quad B(\theta) \cong B(\eta) =: B,$$

$$k(\theta) \cong k(\eta) + K\vartheta, \quad d(\theta, \dot{\theta}) \cong D_2\dot{\vartheta},$$

where J , D_1 , D_2 , K , and B are constant matrices,¹ $A(\vartheta)$ is affine in ϑ , and $Q(\vartheta)$ is quadratic in ϑ . Hence, assuming that $\vartheta(t)$ and its derivatives are small, and that $\dot{w}(t) \cong v_o$,

¹With a slight abuse of notation, we use symbol J to denote the nominal value of $J(\theta)$, and similarly for B .

the general equations of motion in (2.3) are approximated by

$$\begin{aligned} J\ddot{\vartheta} + D\dot{\vartheta} + K\vartheta + L(\vartheta)v &= Bu, \\ m\dot{v} + A(\vartheta)^\top\dot{\vartheta} + Q(\vartheta)v &= 0, \end{aligned} \tag{2.6}$$

where $D := D_1 + D_2$, $L(\vartheta) := A(\vartheta) - A(0)$, and $v(t) := \dot{w}(t)$ is the velocity of the center of mass. We shall call the system (2.6) a *bilinear rectifier* since the essential mechanism for thrust generation is captured by the bilinear term $A(\vartheta)^\top\dot{\vartheta}$ as explained in the next section.

2.2.2 Bilinear mechanism for rectification

The dynamics of rectification is transparent in the simplified equations of motion (2.6). In particular, the second equation shows that a periodic body movement $\vartheta(t)$ leads to the thrust $-A(\vartheta)^\top\dot{\vartheta}$ and drag $Q(\vartheta)v$. The difference between the two gives the acceleration term $m\dot{v}$, and the thrust and drag should balance on average during the steady state locomotion. A close look at the thrust term reveals that the essential dynamics of rectification is captured by the skew-symmetric part of the linear coefficient matrix in $A(\vartheta)$. To explain this, let us consider the simple case where the direction of locomotion is fixed ($p = 1$) and define $\Lambda \in \mathbb{R}^{n \times n}$ by $A(\vartheta) = \Lambda\vartheta + A(0)$. Then the average thrust α over a cycle of periodic motion is given by

$$\alpha = -\int_0^T A(\vartheta)^\top\dot{\vartheta}dt = -\int_0^T \dot{\vartheta}^\top S\vartheta dt, \quad S := \frac{\Lambda - \Lambda^\top}{2}, \tag{2.7}$$

where T is the period of $\vartheta(t)$, and we noted that the integral of $\dot{\vartheta}^\top P\vartheta$ over a cycle is zero for any periodic signal ϑ and for an arbitrary symmetric matrix P . We now see that the periodic motion $\vartheta(t)$ is rectified through the bilinear mechanism $\dot{\vartheta}^\top S\vartheta$ in (2.7) to generate the thrust. This observation motivates us to call (2.6) the bilinear rectifier. It should be emphasized that, if the original equations of motion (2.3) are linearized in terms of ϑ , then we have $\Lambda = 0$ and the resulting approximation fails to capture the thrust essential for

locomotion.

The bilinear mechanism in (2.7) is a generalization of the rectifying dynamics studied by Brockett [2, 90], where $\dot{\vartheta}^T S \vartheta$ takes the form $\vartheta_1 \dot{\vartheta}_2 - \vartheta_2 \dot{\vartheta}_1$, representing a canonical dynamics for rectification. The basic mechanism for gait selection is embedded in the eigenvectors of S . It has been shown [85] that the eigenvector ϑ_o of jS associated with the maximum eigenvalue λ_o gives the basic gait, which maximizes the thrust to amplitude ratio at a given cycle frequency ω :

$$\max_{\vartheta \in \mathbb{P}_T} \frac{\int_0^T (-\dot{\vartheta}^T S \vartheta) dt}{\int_0^T \|\vartheta\|^2 dt} = \max_{\hat{\vartheta} \in \mathbb{C}^n} \frac{j\omega \hat{\vartheta}^* S \hat{\vartheta}}{\|\hat{\vartheta}\|^2} = \omega \lambda_o, \quad (2.8)$$

where $T := 2\pi/\omega$ and the maximum is attained at $\hat{\vartheta} = \vartheta_o$ or $\vartheta(t) = \Re[\vartheta_o e^{j\omega t}]$. The resulting gait $\vartheta(t)$ turns out to be a circle on the $(\vartheta_1, \vartheta_2)$ plane for Brockett's canonical rectifier, and a body undulation with traveling waves for a robotic snake [57]. Optimality criteria for gait selection would also include other factors such as energy consumption and amplitudes of control inputs and motion variables. The optimal gaits with respect to such criteria turn out to be variations of the basic gait embedded in the bilinear rectification mechanism.

Chapter 3

Optimal Gait Problem

3.1 Optimal locomotion of the bilinear rectifier

In this section, we first formulate an optimal locomotion problem to find a gait (periodic ϑ) that minimizes a quadratic cost function for the mechanical rectifier. The problem is difficult, so we reformulate it for tractability using the standard averaging technique, and finally give a globally optimal solution to the modified problem. The optimal gait theory will be developed for the bilinear rectifier (2.6), but the result will be validated later for the original fully nonlinear system (2.3) through numerical simulations.

3.1.1 Problem formulation

Consider the mechanical rectifier (2.6) with nominal posture η at locomotion velocity v_o . We would like to find an optimal gait $\vartheta(t)$ (and the control input $u(t)$ achieving the gait) that minimizes a quadratic cost function subject to the constraint that the average velocity of locomotion is v_o . The problem can be formulated as the following optimization over the

set of T -periodic signals \mathbb{P}_T :

$$\begin{aligned} & \min_{\substack{T \in \mathbb{R}_+ \\ v, \vartheta, u \in \mathbb{P}_T}} \frac{1}{T} \int_0^T \begin{bmatrix} \vartheta \\ u \end{bmatrix}^\top \overset{\circ}{\Pi} \begin{bmatrix} \vartheta \\ u \end{bmatrix} dt \\ & \text{subject to } \frac{1}{T} \int_0^T v dt = v_o, \end{aligned} \quad (3.1)$$

where u , ϑ , and v are signals satisfying (2.6), and $\Pi(s) \in \mathbb{II}$ is a given transfer function. Without loss of generality, we assume that the locomotion is along the x -axis with speed $v \in \mathbb{R}$, so that $v_o = ve_1$.

The objective function is quadratic in ϑ and u , and through the choice of $\Pi(s)$, derivatives of ϑ and u may also be captured, representing many physical quantities. Table 3.1 provides a short list of such quantities and their associated weighting function $\Pi(j\omega)$, where $\varphi := W\vartheta$ is the vector of shape variables (e.g. joint angles) specified by a constant matrix W . The average value over one period is taken for input power, and mean-square values for the other quantities. The cost function can be made to include multiple objectives by taking a weighted sum of these (and other) quantities.

Table 3.1: Objective functions specified by Π

Quantity	Objective Integral	$\Pi(j\omega)$
Perturbation from η	$\frac{1}{T} \int_0^T \ \vartheta\ ^2 dt$	$\begin{bmatrix} I & 0 \\ 0 & 0 \end{bmatrix}$
Shape Magnitude	$\frac{1}{T} \int_0^T \ \varphi\ ^2 dt$	$\begin{bmatrix} W^\top W & 0 \\ 0 & 0 \end{bmatrix}$
Shape Derivative	$\frac{1}{T} \int_0^T \ \dot{\varphi}\ ^2 dt$	$\begin{bmatrix} \omega^2 W^\top W & 0 \\ 0 & 0 \end{bmatrix}$
Input Torque	$\frac{1}{T} \int_0^T \ u\ ^2 dt$	$\begin{bmatrix} 0 & 0 \\ 0 & I \end{bmatrix}$
Input Torque Rate	$\frac{1}{T} \int_0^T \ \dot{u}\ ^2 dt$	$\begin{bmatrix} 0 & 0 \\ 0 & \omega^2 I \end{bmatrix}$
Input Power	$\frac{1}{T} \int_0^T \dot{\theta}^\top B u dt$	$\frac{1}{2} \begin{bmatrix} 0 & -j\omega B \\ j\omega B^\top & 0 \end{bmatrix}$

For the quadratic cost function with an arbitrary weighting Π_o , the solution to problem (3.1) may generate a gait with a large amplitude oscillation of ϑ , violating the small am-

plitude assumption imposed to derive the quadratic equations of motion in (2.6). Such gait may not be appropriate for the original equations of motion (2.3). To remedy this situation, one can penalize the amplitude of ϑ by setting

$$\Pi = (1 - \beta)\Pi_a + \beta\Pi_o, \quad (3.2)$$

where Π_a corresponds to the first entry in Table 3.1, and β is a weighting parameter satisfying $0 \leq \beta \leq 1$. When Π_a and Π_o define competing objectives, the amplitude of optimal ϑ would be a nondecreasing function of β . The largest value of β can thus be found so as to satisfy a hard constraint on the amplitude of ϑ , if desired. This type of Pareto-optimal approach has been used for multiobjective H_2 control with a proof of convergence [91].

3.1.2 Tractable reformulation

Let us now reformulate the problem in (3.1) for tractability by simplifying the constraints through the averaging technique. If $v(t) \cong v_o = \mathbf{v}e_1$, it follows from averaging the second equation in (2.6) over a cycle that

$$\int_0^T \left((a_i + \vartheta^\top Q_i \vartheta) \mathbf{v} + \dot{\vartheta}^\top \Lambda_i \vartheta dt \right) = 0 \quad (3.3)$$

holds approximately for $i \in \mathbb{Z}_p$, where a_i , Q_i , and Λ_i are the constants specified by

$$L(\vartheta)e_i = \Lambda_i \vartheta, \quad e_i^\top Q(\vartheta)e_1 = a_i + b_i^\top \vartheta + \vartheta^\top Q_i \vartheta.$$

Conversely, if (3.3) holds, then $v(t) \equiv v_o$ satisfies the second equation in (2.6) on average. Therefore, it appears reasonable to replace the velocity constraint in (3.1) and the second

equation in (2.6) by the p equations in (3.3). Finally, let us define the following problem:

$$\begin{aligned} \min_{\substack{T \in \mathbb{R}_+ \\ \vartheta, u \in \mathbb{P}_T}} \frac{1}{T} \int_0^T \begin{bmatrix} \vartheta \\ u \end{bmatrix}^\top \mathring{\Pi} \begin{bmatrix} \vartheta \\ u \end{bmatrix} dt \quad \text{subject to} \\ \left\{ \begin{array}{l} \int_0^T \left((a_1 + \vartheta^\top Q_1 \vartheta) v + \dot{\vartheta}^\top \Lambda_1 \vartheta \right) dt = 0, \\ J \ddot{\vartheta} + D \dot{\vartheta} + (K + v \Lambda_1) \vartheta = Bu \end{array} \right. \end{aligned} \quad (3.4)$$

where the constraint (3.3) is imposed only for $i = 1$. We expect that a solution to this problem will automatically satisfy the remaining omitted acceleration constraints, i.e., (3.3) for $i = 2, \dots, p$, on the grounds that acceleration in a direction normal to \mathbb{V} would require a larger value of the objective function and would hence be eliminated. This is also what we have observed in all of our numerical studies.

The omission of constraints (3.3) for $i = 2, \dots, p$ can be rigorously justified for certain practical cases. Recall that most animals have a body symmetric about an axis (or a plane), and the direction of locomotion is often chosen to be aligned with the axis of symmetry. A robotic locomotor may be designed to have this property. In this case, feasible gaits may be restricted to be symmetric about the \mathbb{V} line, at the expense of potential increase in the cost function value. A benefit is that the symmetry can be exploited to make the gait optimization simpler. A symmetric gait would automatically lead to locomotion along the \mathbb{V} line due to the balance of forces. The equations of motion (2.6) can then be given in terms of a reduced number of independent variables with only one degree of freedom in v , i.e., $p = 1$. For an example, the locomotor in Fig. 2.1 could be reduced to the system shown in Fig. 3.1, assuming that the arm and leg movements are symmetric about the dashed line. The reduction in the size of the optimization problem (the dimensions of ϑ and u) would generally lead to more efficient and reliable computation.

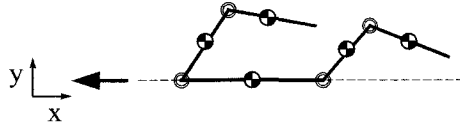


Figure 3.1: Exploiting symmetry of the frog-like multilink system

3.1.3 Globally optimal solution

This section presents an exact solution to the problem in (3.4). We first consider a finite dimensional approximation of the problem where the underlying space of periodic signals \mathbb{P}_T in (3.4) is replaced by the subspace \mathbb{P}_T^h spanned by the first h harmonics of the Fourier series expansion for a given $h \in \mathbb{Z}$. The following lemma reduces this modified problem to a constrained quadratic optimization.

Lemma 1 *Let $h \in \mathbb{Z}$ be given, and consider the problem obtained by replacing \mathbb{P}_T by \mathbb{P}_T^h in (3.4). Define*

$$\begin{aligned} X(\omega) &:= \frac{1}{2} \begin{bmatrix} P(\omega) \\ I \end{bmatrix}^* \Pi(j\omega) \begin{bmatrix} P(\omega) \\ I \end{bmatrix}, \\ Y(\omega) &:= P(\omega)^* (S(\omega) - \nu Q_1) P(\omega) / (2a_1 \nu), \\ S(\omega) &:= j\omega(\Lambda_1 - \Lambda_1^T) / 2, \\ P(\omega) &:= (\nu \Lambda_1 + K + j\omega D - \omega^2 J)^{-1} B. \end{aligned} \tag{3.5}$$

Then the problem is equivalent to

$$\min_{\omega \in \mathbb{R}, \hat{u} \in \mathbb{C}^{\ell h}} \{ \hat{u}^* X^h(\omega) \hat{u} : \hat{u}^* Y^h(\omega) \hat{u} = 1 \}. \tag{3.6}$$

In particular, a solution (ω, \hat{u}) to (3.6) gives an optimizer

$$u(t) = \sum_{k=1}^h \Re [\hat{u}_k e^{j\omega k t}], \quad \hat{u} = \text{col}(\hat{u}_1, \dots, \hat{u}_h)$$

for the original problem (3.4).

Proof. Let \hat{v}_k and \hat{u}_k be the k^{th} phasors of periodic signals $v(t)$ and $u(t)$, respectively. Using Lemma 6 in Appendix 6.1, it can be verified that the objective function in (3.4) is given by

$$\frac{1}{2} \sum_{k=1}^h \begin{bmatrix} \hat{v}_k \\ \hat{u}_k \end{bmatrix}^* \Pi(j\omega k) \begin{bmatrix} \hat{v}_k \\ \hat{u}_k \end{bmatrix}$$

and the constraints are expressed as

$$\left(2a_1 + \sum_{k=1}^h \hat{v}_k^* Q_1 \hat{v}_k \right) v - \sum_{k=1}^h \hat{v}_k^* S(\omega k) \hat{v}_k = 0,$$

$$\hat{v}_k = P(\omega k) \hat{u}_k, \quad k \in \mathbb{Z}_h.$$

The result then follows by eliminating the variable \hat{v}_k through the second constraint and assembling the summations into Hermitian forms of augmented vectors. ■

For a fixed ω , the problem in (3.6) is a static quadratic optimization, which is nonconvex in general because $X^h(\omega)$ and $Y^h(\omega)$ are possibly indefinite. Nonconvex optimizations are often hard to solve, but for this particular problem, we have an exact, analytical solution.

Lemma 2 *Let Hermitian matrices X and Y be given and consider*

$$\min_{z \in \mathbb{C}^m} \{ z^* X z : z^* Y z = 1 \}. \quad (3.7)$$

The constraint is feasible if and only if the largest eigenvalue of Y is positive. In this case, the objective function is bounded below on the feasible set if and only if the following (convex) set is nonempty:

$$\mathbb{L} := \{ \lambda \in \mathbb{R} : X \geq \lambda Y \}.$$

The largest element λ_o of \mathbb{L} is well defined and is a generalized eigenvalue of (X, Y) . The minimum value of (3.7) is equal to λ_o . An optimizer z_o is given by an eigenvector of the pair (X, Y) associated with the generalized eigenvalue λ_o , normalized so that $z_o^ Y z_o = 1$.*

Proof. The minimum value in (3.7) is bounded below and is greater than a given value $\gamma \in \mathbb{R}$ if and only if

$$z^*Xz \geq \gamma, \quad \forall z \in \mathbb{C}^m \quad \text{s.t.} \quad z^*Yz = 1.$$

Feasibility of the constraint implies its regularity; if z_o satisfies $z_o^*Yz_o = 1$, then $z = 2z_o$ and $z_o/2$ respectively make the value of $z^*Yz - 1$ positive and negative. Hence, the S-procedure (Lemma 7 in Appendix 6.1) can be used to verify that this condition holds if and only if there exists $\lambda \in \mathbb{R}$ such that

$$z^*Xz - \gamma \geq \lambda(z^*Yz - 1), \quad \forall z \in \mathbb{C}^m,$$

which is equivalent to

$$X \geq \lambda Y, \quad \gamma \leq \lambda.$$

The minimum value in (3.7) is obtained by maximizing γ subject to these constraints over the variables $\lambda, \gamma \in \mathbb{R}$. Since the largest γ is equal to λ , the minimum value is given by the largest element of \mathbb{L} .

Let $f(\lambda)$ be the minimum eigenvalue of $X - \lambda Y$. Note that $f(\lambda)$ is a concave function of λ since the matrix is affine in λ . By feasibility of the constraint, Y must have at least one positive eigenvalue, and hence $f(\lambda)$ is negative for sufficiently large λ . On the other hand, boundedness of the objective function guarantees that \mathbb{L} is nonempty, and hence $f(\lambda)$ is nonnegative for some λ . Therefore, there exists λ_o such that $f(\lambda_o) = 0$ and $f(\lambda) < 0$ for all λ greater than λ_o . Clearly, λ_o is the largest element of \mathbb{L} , and is a generalized eigenvalue of (X, Y) .

If an eigenvector z_o of (X, Y) , associated with the generalized eigenvalue λ_o , can be chosen so that $z_o^*Yz_o = 1$, then it is easy to verify that z_o is an optimizer that gives the objective function value λ_o . To show existence of such z_o , let z_e be an eigenvector of

$Z_\varepsilon := X - (\lambda_o + \varepsilon)Y$ associated with its minimum eigenvalue, where $\varepsilon \in \mathbb{R}$. Since λ_o is the largest element of \mathbb{L} , we have $z_\varepsilon^* Z_\varepsilon z_\varepsilon < 0$ for all $\varepsilon > 0$. Since $Z_0 \geq 0$, we have

$$0 \leq z_\varepsilon^* Z_0 z_\varepsilon = z_\varepsilon^* (Z_\varepsilon + \varepsilon Y) z_\varepsilon < \varepsilon z_\varepsilon^* Y z_\varepsilon.$$

Thus $z_\varepsilon^* Y z_\varepsilon$ is positive and therefore z_ε can be normalized so that $z_\varepsilon^* Y z_\varepsilon = 1$. In this case, $z_\varepsilon^* Z_\varepsilon z_\varepsilon < 0$ implies $z_\varepsilon^* X z_\varepsilon < \lambda_o + \varepsilon$. Now, the result follows by passing the limit $\varepsilon \downarrow 0$ and noting that $Z_\varepsilon z_\varepsilon \rightarrow 0$. ■

Based on Lemma 2, a solution to (3.7) can be found by computing the generalized eigenvalues of (X, Y) . If the constraint is feasible and objective function is bounded, then one (or more) of the generalized eigenvalues must be real and satisfy $X \geq \lambda Y$. The largest of such generalized eigenvalues is λ_o . If λ_o is not repeated, then it has one-dimensional eigenspace. In this case, every eigenvector z_o satisfies $z_o^* Y z_o > 0$ and hence can be normalized so that $z_o^* Y z_o = 1$. This z_o is an optimizer of (3.7). If λ_o is repeated, then the dimension of the eigenspace is more than one and $z_o^* Y z_o$ can be nonpositive for some eigenvector. However, Lemma 2 guarantees that there is at least one vector in the eigenspace that gives positive $z_o^* Y z_o$ and hence is a solution after the normalization.

The following result establishes that the optimal value of (3.6) is independent of h . The important implication is that the optimum of the original problem (3.4) can always be achieved by a sinusoid with a single frequency component.

Lemma 3 *Consider the optimization problem (3.6), and denote by γ_h the optimal value of the objective function. Then, for an arbitrary $h \in \mathbb{Z}$, it holds that $\gamma_h = \gamma_1$.*

Proof. In view of Lemma 2, the problem (3.6) can be reformulated as

$$\begin{aligned} \gamma_h &= \min_{\omega \in \mathbb{R}} \max_{\lambda \in \mathbb{R}} \{ \lambda : X^h(\omega) \geq \lambda Y^h(\omega) \} \\ &= \min_{\omega \in \mathbb{R}} \max_{\lambda \in \mathbb{R}} \{ \lambda : X(k\omega) \geq \lambda Y(k\omega), \forall k \in \mathbb{Z}_h \}. \end{aligned}$$

Note that, for each $k\omega$, the set of $\lambda \in \mathbb{R}$ satisfying $X(k\omega) \geq \lambda Y(k\omega)$ is convex. Using this fact, the problem can further be reformulated as

$$\begin{aligned}\gamma_h &= \min_{\omega \in \mathbb{R}} \min_{k \in \mathbb{Z}_h} \max_{\lambda \in \mathbb{R}} \{ \lambda : X(k\omega) \geq \lambda Y(k\omega) \} \\ &= \min_{\omega \in \mathbb{R}} \max_{\lambda \in \mathbb{R}} \{ \lambda : X(\omega) \geq \lambda Y(\omega) \}.\end{aligned}$$

Thus $\gamma_h = \gamma_1$ and the proof is complete. ■

We are now ready to state the main result.

Theorem 1 *Consider the rectifier system given in (2.6) and the optimal locomotion problem in (3.4). Define $X(\omega)$, $Y(\omega)$, and $P(\omega)$ by (3.5). Let γ be the optimal value of the objective function. Then we have*

$$\gamma = \min_{\omega \in \mathbb{R}} \max_{\lambda \in \mathbb{R}} \{ \lambda : X(\omega) \geq \lambda Y(\omega) \}. \quad (3.8)$$

Let ω_o and λ_o be the optimizers. Then, the optimal period is $T = 2\pi/\omega_o$, and the optimal gait ϑ and input u are given by

$$u(t) = \Re[z_o e^{j\omega_o t}], \quad \vartheta(t) = \Re[P(\omega_o) z_o e^{j\omega_o t}],$$

where $z_o \in \mathbb{C}^\ell$ is the eigenvector of the pair $(X(\omega_o), Y(\omega_o))$ associated with the generalized eigenvalue λ_o , normalized to satisfy $z_o^ Y(\omega_o) z_o = 1$.*

Proof. Recall that the cost function is an average value of $\xi^T \Psi \xi$ over one cycle, where ξ is the steady state output of $F(s)$ with input $[\vartheta^T \ u^T]^T \in \mathbb{P}_T$, and Ψ and $F(s)$ are defined from $\Pi(s) = F(-s)^T \Psi F(s) \in \mathbb{III}$. Since \mathbb{P}_T is a subset of continuously differentiable periodic signals and $F(s)$ is a linear combination of stable transfer functions and differentiators, the signal ξ is continuous and periodic. Therefore, the signal ξ , and hence the definite integral of $\xi^T \Psi \xi$ in the cost function, can be approximated by truncated Fourier series to

an arbitrary accuracy. From Lemma 1, the problem (3.4) can then be characterized as the limit ($h \rightarrow \infty$) of the sequence of quadratic optimizations (3.6). Lemma 3 shows that the optimal value of (3.6) is independent of h , hence the optimal value of the original problem (3.4) is equal to that of (3.6) with $h = 1$, indicating that a sinusoid is an optimizer. The solution to the optimization over \mathbb{P}_T^1 is given by Lemma 2 with $h = 1$, as stated in the theorem. ■

The optimal locomotion problem (3.6) is nonconvex (partly) due to the velocity constraint. In general, it is difficult to find a solution to a nonconvex problem, with guaranteed global optimality, since multiple local optima may exist. For our particular problem, however, it is possible to determine the global optimum with the aid of the S-procedure (Lemma 7 in Appendix 6.1) as shown in Theorem 1. The optimal gait among all periodic functions has turned out to be a pure sinusoid for the bilinear rectifier (2.6). This can be viewed as a generalization of the previous result [85] that proved optimality of sinusoids when maximizing the thrust generated by a bilinear rectifier. The problem in (3.8) can be solved by generalized eigenvalue computation plus a line search over the frequency ω . In particular, the optimal solution, for a fixed ω , is given by the maximal real generalized eigenvalue λ_o of the pair $(X(\omega), Y(\omega))$ and the corresponding eigenvector z_o .

3.2 Verification through case studies

In this section, we will demonstrate the utility of our optimal gait result through analytical and numerical examples. We first consider a simple mechanical rectifier, which is a disk-mass system that captures the rectifier dynamics in the simplest manner. Analytical solutions are obtained for this simple case, which is used to make some general observations through analogy to more complex rectifiers. We also consider a mechanical rectifier formed by a chain of rigid links, and apply Theorem 1 to find optimal gaits with respect to several cost functions. Two nominal postures are examined: the straight posture “—”

and the bow posture “(” while moving to the left. Various gaits will be shown to emerge from optimization of different cost functions with different nominal postures, including undulatory and flapping gaits as well as their hybrid.

3.2.1 Simple mechanical rectifier

A very simple model, as shown in Fig. 3.2, which consists of a spinning disk with moment of inertia J , driven by the friction of a point mass m sliding on its surface, contains all the essential elements of the locomotion problem.

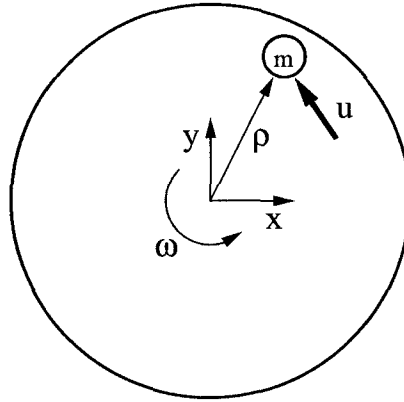


Figure 3.2: Simple mechanical rectifier

The point mass receives a controlling force u and represents the dynamics of an organisms body. The friction force between point mass and disk, which is proportional to the relative velocity with constant c , represents the interaction of the body with the environment, and the angular velocity of the disk ϖ represents the locomotion speed. We call this system a simple mechanical rectifier (SMR) since periodic movements of the mass can be rectified to yield disk rotation in a fixed direction on average.

The equation of motion is given by

$$\begin{aligned} m\ddot{\rho} + (c + d)\dot{\rho} + c\varpi S\rho &= u, \\ J\dot{\varpi} + (a + c\rho^T\rho)\varpi + c\rho^T S\rho &= 0, \end{aligned} \tag{3.9}$$

where $\rho(t) \in \mathbb{R}^2$ is the coordinate of the point mass, and

$$S := \begin{bmatrix} 0 & 1 \\ -1 & 0 \end{bmatrix}.$$

The $d\dot{\rho}$ term represents the energy loss associated with the actuation of the point mass by input u , and $a\varpi$ is the frictional torque at the disk bearing. Clearly, (3.9) is of the form (2.6) where ρ and ϖ correspond to ϑ and v , respectively. Note that the nominal posture ($\rho = 0$) for SMR is when the mass is at the disk center.

To examine the mechanism of rectification, let us consider the case where the disc inertia J is so large that ϖ may be considered constant over a cycle. In this case, the standard averaging technique yields

$$\begin{aligned} \varpi &\cong \alpha / \int_0^T (a/c + \|\rho\|^2) dt, \\ \alpha &:= - \int_0^T \dot{\rho}^\top S \rho dt = \int_0^T (\rho_1 \dot{\rho}_2 - \rho_2 \dot{\rho}_1) dt, \end{aligned}$$

where T is the cycle period of the mass movement. Note that α is a half of the area enclosed by the orbit of the mass trajectory $\rho(t)$, which is defined positive when the orbit goes counterclockwise. For the same size of mass motion as measured by α , faster rotation is achieved if the mass motion occurs near the disk center so that ρ , and hence the denominator, is small. For this reason, it makes sense to choose the nominal posture at the disk center. The term $\rho_1 \dot{\rho}_2 - \rho_2 \dot{\rho}_1$ is the Lie bracket $[\rho_1, \rho_2]$, representing a canonical form of rectifying dynamics studied by [90] in the context of nonholonomic systems control.

We shall apply Theorem 1 to the simple mechanical rectifier described by (3.9) to find two optimal gaits that minimize the input power and shape derivative, respectively, while

maintaining the average angular velocity ϖ_o . In particular, we consider

$$\gamma := \min_{\substack{T \in \mathbb{R}_+ \\ \rho, u \in \mathbb{H}_T}} \frac{1}{T} \int_0^T f(\dot{\rho}, u) dt$$

$$\text{s.t.} \quad \begin{cases} \int_0^T ((a + c\rho^\top \rho)\varpi_o + c\dot{\rho}^\top S\rho) dt = 0, \\ m\ddot{\rho} + (c + d)\dot{\rho} + \varpi_o c S\rho = u, \end{cases} \quad (3.10)$$

where $f(\dot{\rho}, u) := \dot{\rho}^\top u$ (input power) or $\|\dot{\rho}\|^2$ (“shape” derivative). The result is summarized as follows.

Lemma 4 *Consider the simple mechanical rectifier in (3.9) and the optimal locomotion problem in (3.10). The globally optimal solution is characterized by*

$$\rho(t) = \alpha \begin{bmatrix} \cos \omega t \\ \sin \omega t \end{bmatrix},$$

where ρ , α , and associated optimal cost γ , are given by Table 3.2 with $a_c := a/c$ and $d_c := d/c$.

Table 3.2: Optimal parameters for SMR locomotion

	Input Power	Shape Derivative
γ	$2ad_c \left(1 + \sqrt{1 + \frac{1}{d_c}}\right)^2 \varpi_o^2$	$8a_c \varpi_o^2$
α	$\sqrt{a_c} \sqrt{1 + \frac{1}{d_c}}$	$\sqrt{a_c}$
ω	$\left(1 + \sqrt{\frac{d_c}{1 + d_c}}\right) \varpi_o$	$2\varpi_o$

Proof. The result basically follows from Theorem 1, but the analytical formulas are easier to derive if we first reformulate the problem in terms of ρ rather than u . This is possible because the coefficient matrix of u is square nonsingular. Following a similar procedure to

Lemma 1, the problem reduces to

$$\min_{\omega \in \mathbb{R}, \hat{\rho} \in \mathbb{C}^2} \{ \hat{\rho}^* X_\omega \hat{\rho} : \hat{\rho}^* Y_\omega \hat{\rho} = 1 \},$$

where X_ω and Y_ω are defined by

$$X_\omega := \omega((c+d)\omega I - j\varpi_o cS), \quad Y_\omega := c(j\omega S - \varpi_o I)/(2a\varpi_o)$$

for the minimum input power case, and $X_\omega := \omega^2 I$ and the same Y_ω as above for the minimum shape derivative case.

In view of Lemma 2, we fix ω and search for generalized eigenvalue/eigenvector pair (λ, e) such that $(X_\omega - \lambda Y_\omega)e = 0$. Since both X_ω and Y_ω are of the form $\alpha I + \beta S$, we see that e must be an eigenvector of S , i.e., $e_\pm := [1 \pm j]^T$. Hence, the optimal ρ is a scalar multiple of e_+ or e_- . For feasibility, we choose the one such that

$$e_\pm^* Y_\omega e_\pm = (c/a)(\mp\omega/\varpi_o - 1) > 0.$$

Since the signal $\rho(t)$ expressed by its phasor $\hat{\rho}$ and frequency ω can also be expressed by the conjugate of $\hat{\rho}$ and $-\omega$, we can fix the sign of ω without loss of generality. Here, we let ω have the same sign as ϖ_o . In this case, the feasibility requires us to choose e_- and the frequency must satisfy $|\omega| > |\varpi_o|$. For such ω , the optimal $\hat{\rho}$ is given by $\hat{\rho} = \alpha e_-$ for positive scalar α such that $\hat{\rho}^* Y_\omega \hat{\rho} = 1$. More specifically,

$$\hat{\rho} = \alpha \begin{bmatrix} 1 \\ -j \end{bmatrix}, \quad \alpha = \sqrt{\frac{a_c \varpi_o}{\omega - \varpi_o}}.$$

To find the optimal frequency, we minimize $\gamma(\omega) := \hat{\rho}^* X_\omega \hat{\rho}$ over ω . Taking the derivative, setting the result to be zero, and solving for ω such that $|\omega| > |\varpi_o|$, we obtain the unique solution indicated in Table 3.2. ■

The optimal orbit of the mass, $\rho(t)$, is circular; $\rho_1(t)$ and $\rho_2(t)$ have the same amplitude, and the former leads the latter by 90° . This property is independent of the system parameters and the desired speed ϖ_o , but is determined by the structure of the rectifying dynamics as an eigenvector of S , as shown in Section 2.2.2.

We notice from Table 3.2 that the optimal frequency ω is proportional to the desired speed ϖ_o , which makes physical sense. On the other hand, the optimal amplitude α is independent of ϖ_o , but scales with the square root of a/c . The parameters a and c roughly correspond to c_t and c_n in the undulatory locomotor, respectively. Hence, the fact that the ρ orbit is larger when a/c is larger, is analogous, for instance, to the fact that snakes undulate with larger amplitude on ice than on grounds.

Finally, we note that the optimal α and ω for the minimum input power approach that for the minimum shape derivative as d/c tends to infinity. If the cost (power loss) for the mass motion itself is much larger than the cost for driving the disk, then the minimum power gait tends to minimize the mass motion. Generalizing the idea for the undulatory locomotor, we expect that the optimal gaits from the input power and shape derivative minimizations would become similar if the joint frictions (ignored in our study) were large. In fact, this expectation turned out to be true, and moreover, optimal gaits from input torque minimization also approached the optimal shape derivative case. Thus, the choice of the objective functions among those in Table 3.1 is not important and all cases give similar results when the joint frictions are large.

3.2.2 Link chain rectifier

Consider the planar motion of a chain of n rigid links as shown in Fig. 3.3. For $i \in \mathbb{Z}_n$, the i^{th} link has mass m_i , moment of inertia J_i , length $2\ell_i$, and angular displacement $\theta_i(t)$ measured from the x -axis. For $i \in \mathbb{Z}_{n-1}$, the joint between the i^{th} and $(i+1)^{\text{th}}$ links is actuated by torque input u_i (when positive, the i^{th} and $(i+1)^{\text{th}}$ links tend to rotate counterclockwise and clockwise, respectively), and the joint angle is denoted by $\phi_i :=$

$\theta_i - \theta_{i+1}$. The body is placed in an environment (on the ground, in water, etc.), and is subject to the interactive forces.

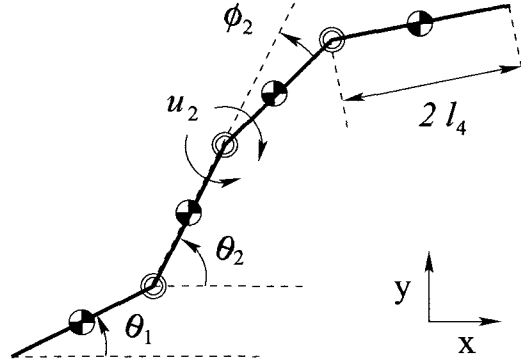


Figure 3.3: Link chain rectifier

The key property for mechanical rectification is the difference in the tangential and normal components of the interactive force from the environment acting on each link. In particular, the normal force tends to be much larger than the tangential force. This is true for e.g. snake crawling on the ground [87] as well as for slender-body swimming [89, 92, 93]. The simplest way to capture this property, which is often adequate for at least qualitative analyses, is to approximate the tangential and normal forces on each link (f_{t_i} and f_{n_i}) by linear functions of the respective components of the relative velocity between the link and environment (v_{t_i} and v_{n_i}). That is, for the i^{th} link,

$$f_{t_i} = c_{t_i} v_{t_i}, \quad f_{n_i} = c_{n_i} v_{n_i}, \quad (3.11)$$

where c_{t_i} and c_{n_i} are constants such that $c_{t_i} \ll c_{n_i}$. The linear model in (3.11) may be obtained from direct curve fitting of experimental data, or from (quasi)linearization of a more realistic nonlinear model. We call the system under this type of directional forces a link chain rectifier (LCR).

The general equations of motion for the LCR have been derived in an attempt to model robotic snake locomotion [57], and are of the form given by (2.3). Motion dynamics near an

arbitrary nominal posture η can be approximated by the bilinear rectifier (2.6). The details of the models are summarized in Appendix 6.2. The models thus developed naturally capture the dynamics of slender animals that undulate for locomotion, such as crawling snake [57, 87], and swimming leech and lamprey [94–96]. While the nominal posture for such undulatory locomotion would be straight, optimizations at another nominal posture will lead to flapping gaits, as shown later.

For the planar case ($p = 2$), the term $L(\vartheta)$ for rectifying dynamics in (2.6) has the form $\begin{bmatrix} \Lambda_1 \vartheta & \Lambda_2 \vartheta \end{bmatrix}$. The model for LCR defined in Appendix 6.2 shows that, regardless of the nominal posture η , the skew-symmetric part of Λ_k is zero (in fact Λ_k is diagonal) for $k \in \mathbb{Z}_2$ if the environmental interactive force has no directional preference, i.e., $c_{t_i} = c_{n_i}$ for $i \in \mathbb{Z}_n$. In this case, the net thrust over a cycle is zero for any periodic body motion as seen in (2.7). This is a proof that the directional preference in the environmental force is essential for locomotion of LCR.

For the numerical studies reported below, we set the parameter values from measured data of a medium size leech to keep the model realistic. The leech has mass $m = 1.1$ g and length $\ell = 107.3$ mm, and was observed to swim at speed around 0.157 m/s by undulating its slender body like snakes with a cycle frequency near 2.7 Hz. The leech has a segmented body that can be modeled by a chain of n identical links where $n = 18$.

Serpentine gait

We set the nominal posture to be straight ($\eta = 0$). No stiffness or damping is assumed at the body joints. The parameters of the bilinear rectifier (2.6) for this case are summarized at the end of Appendix 6.2. Assuming an average velocity of $v = -0.157$ m/s (negative sign indicates swimming to the left), the optimal gait problem (3.4) is solved for three cost functions in Table 3.1: input power, input torque, and shape derivative where $W := B$. The optimal gait for each case has been found by solving (3.8) via eigenvalue computations with frequency sweep.

Figure 3.4 shows the minimum value of each objective function as a function of frequency ω , which is the maximum real generalized eigenvalue of the pair $(X(\omega), Y(\omega))$ in (3.5). Each function turned out to be quasi-convex and have a unique global minimum for this particular example. The optimal cycle frequencies of periodic body motion are found to be 22.0 rad/s (power), 78.1 rad/s (torque), and 16.0 rad/s (shape), whereas the frequency observed for the particular leech used for modeling was 17.0 rad/s.

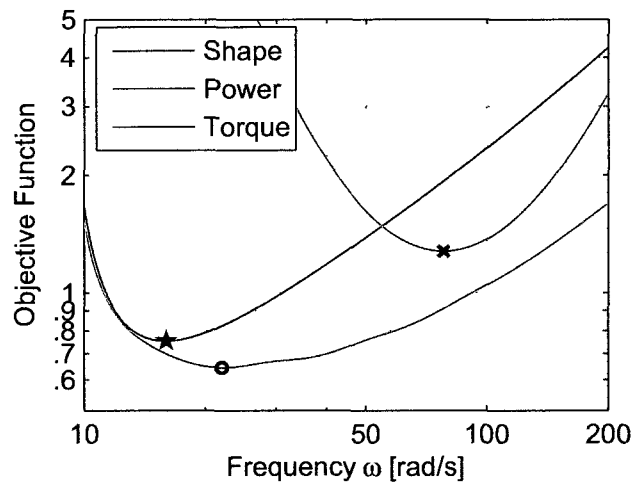


Figure 3.4: Objective function vs. frequency ω : power in mW, torque in $(\text{N}\cdot\text{mm}\cdot 100)^2$, shape derivative in $(\text{deg}/\text{ms})^2$.

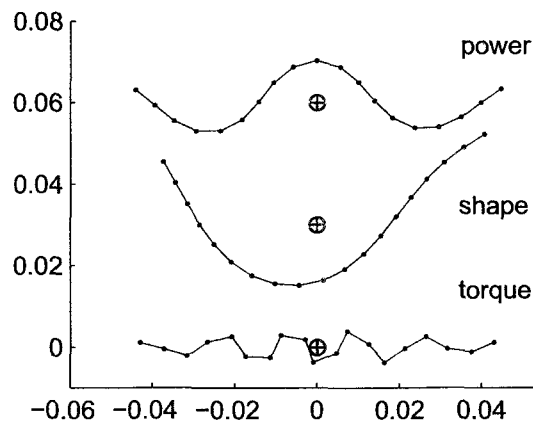


Figure 3.5: Optimal body shapes (snap shots during swimming at an arbitrary time instant)

The optimal body shapes are shown in Fig. 3.5. These shapes are generated from the phases and amplitudes (Fig. 3.6) of the shape variables (joint angles) ϕ_i . In each figure, the leech head/tail is to the left/right. The phase angle decreases from head to tail, indicating waves traveling down the body to generate thrust. The number of waves expressed by the body is roughly equal to the phase lag from head to tail, divided by 360° . During swimming, the live leech exhibited about 250° phase lag, and approximately uniform (but slightly increasing toward the tail) amplitudes over the body of about 10° . The resulting body shape was fairly close to the one for the minimum shape derivative depicted in Fig. 3.5. Hence, it is tempting to conclude that the shape derivative, rather than the power or torque, may be closely related to the quantity that actual leeches try to minimize. However, the SMR results from the previous section show that the power and torque optimal gaits approach the minimum shape case as internal losses due to the shape deformation increase. This could alternatively indicate that the internal losses due to shape deformation in actual leeches is very high, and that the choice of objective is not discernable.

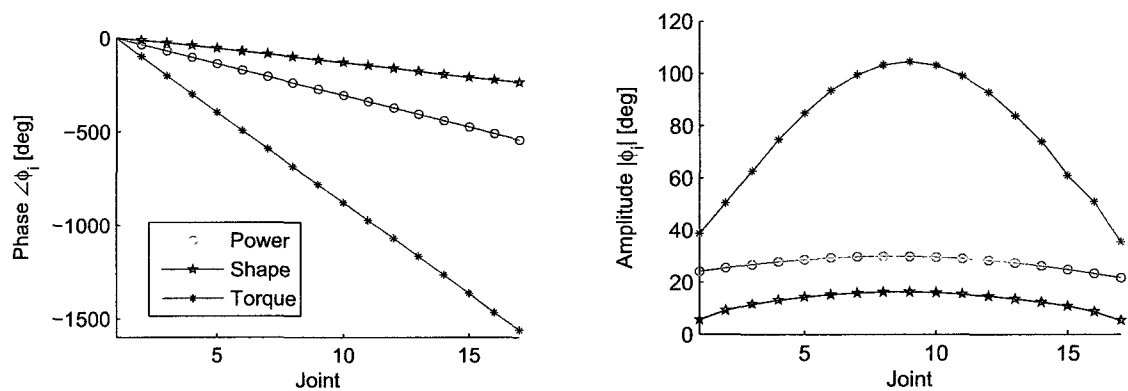


Figure 3.6: Undulatory gaits: Phase and amplitude of relative angles ϕ_i along the body

Propulsive extremities

In the previous section, the nominal posture was chosen to be straight with the locomotion velocity vector v_o aligned with the body. We now consider the situation where the body is initially straight and is *perpendicular* to v_o . The body would then be bent due to the fluid

drag, and, with flexible joints, take a bow posture “(” when it moves to the left and the drag balances with the restoring stiffness force. We choose this as the nominal posture. In particular, η is set so that η_i linearly decreases from $\eta_1 = \pi - 0.068$ to $\eta_n = 0.068$ rad. Assuming an average velocity of $v = -0.1$ m/s (negative sign indicates swimming to the left), the joint stiffnesses k_i ($i \in \mathbb{Z}_{n-1}$) have been specified so that the first condition in (2.5) is satisfied. Gaits expected at this nominal posture include two flagella pushing a central body forward, a radially symmetric jellyfish-like locomotion, or kicking legs attached to a central body for appropriately low numbers of links.

We have solved the optimal locomotion problem in (3.4) with objective function Π in (3.2) where Π_a captures the perturbation from η , and Π_o captures the shape derivative, input torque rate, or input power as indicated in Table 3.1. For each case, the optimal gait was computed using Theorem 1, where the scalar weight β was tuned by iteration so that the amplitude constraint $\|\hat{\vartheta}\|^2 = 10$ was satisfied, as described in Section 3.1.1. The results of the three optimizations are summarized in terms of $\varphi := B^T \hat{\vartheta}$, which are the joint angle deflections from the nominal posture. Numerical simulations are then used to examine the effects of approximations associated with the equations of motion and the optimal gait problem. Unless otherwise noted, the second equation in (2.6) is simulated by enforcing the calculated optimal gait $\theta(t)$ as the input.

Figure 3.7 shows the phase and amplitude of φ for the three optimal gaits whose frequencies are summarized in Table 3.3. We see that the phase is maximum at or around the middle of the body and decreases toward both ends. This means that all three gaits possess some degree of traveling waves down each arm. However, the minimum shape derivative motion has a much smaller phase variation than the power or torque rate case, indicating that it has a much lower number of waves expressed along the body. It should be noted that the torque rate criterion generated an asymmetric gait. After checking this result against the optimal gait under the symmetry constraint, we found that the asymmetric gait did indeed have a strictly smaller minimum objective value. Among the three cases, the average am-

plitude over the body tends to be smaller if the phase variation is smaller. This is because small, relatively in-phase, joint angle amplitudes add up to produce a large overall motion which maintains the desired velocity. Interestingly, the torque rate case does not bend at all at the center joint (only rotates), retaining its initial nominal bend at all times.

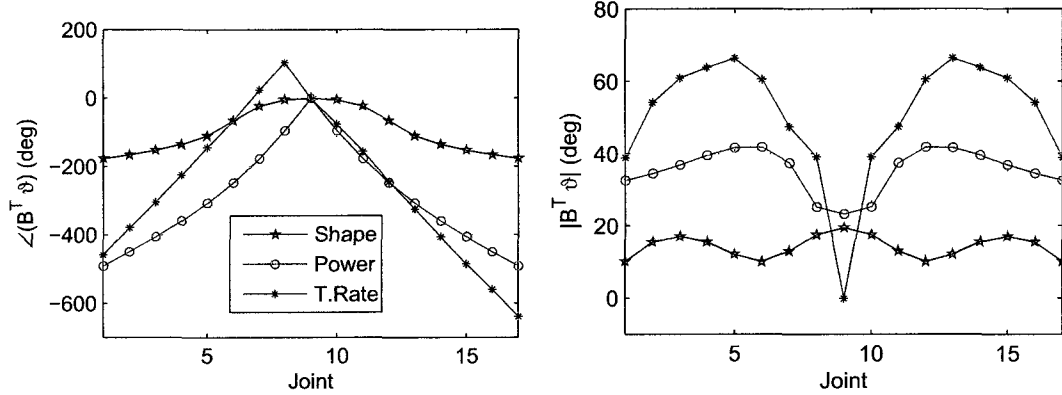


Figure 3.7: Flapping gaits: Phase and amplitude of relative angle perturbations $B^T \vartheta$ along the body

Figure 3.8 shows five snapshots of simulated optimal locomotion for each case, taken 1.25 periods apart. These figures clearly show that the optimal motion calculated for minimum power and shape derivative are symmetric about the direction of locomotion (horizontal axis). The asymmetry is clearly visible for the torque rate case. The flapping gait is found optimal for the shape derivative criterion, while undulation of each arm is optimal for the torque rate criterion. The optimal gait for the power criterion is a mixture of flapping and undulation. The horizontal axis scales are different in each figure due to the differing optimal frequencies calculated for each motion; for example the shape derivative motion moves much further in five periods than the torque rate motion, although the locomotion speeds are about the same.

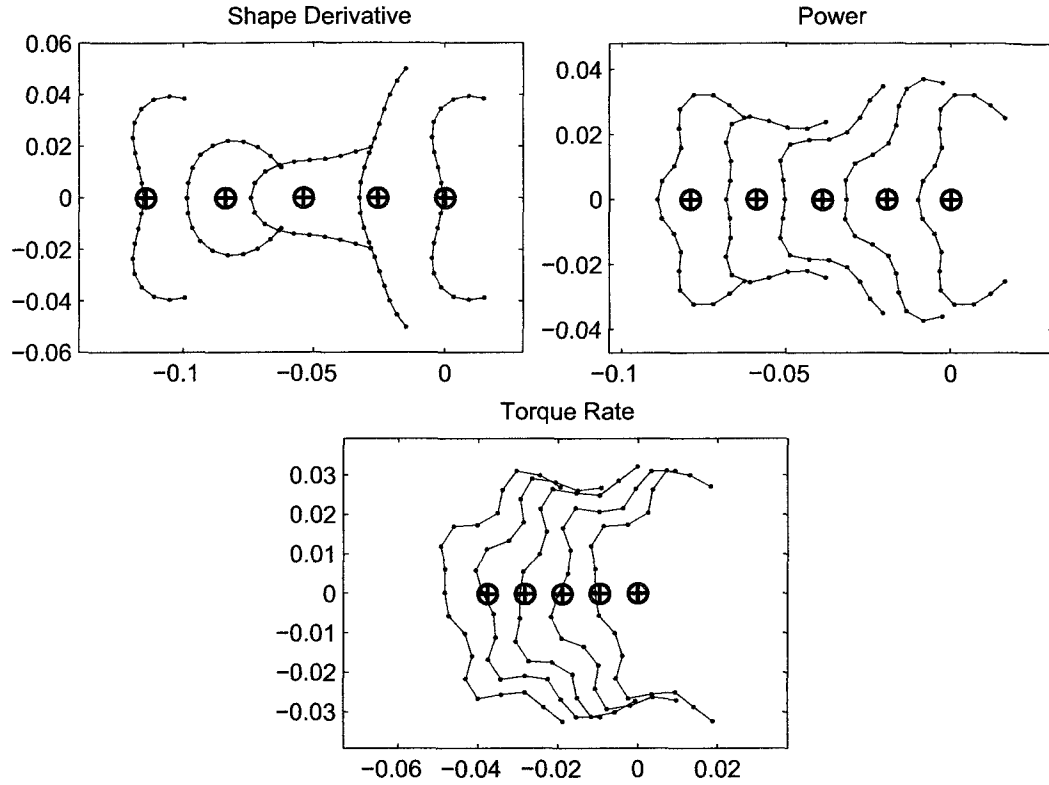


Figure 3.8: Snap shots of LCR locomotion, taken 1.25 periods apart.

Figure 3.9 shows the simulated velocity, where the time responses are colored in the same way as Fig. 3.7 for each case. We see that the y -velocity is exactly zero for the symmetric gaits, and oscillating closely about zero for the asymmetric gait. Thus, as expected, the optimization forces the y -velocity to be zero on average even though no such constraint is explicitly imposed. The oscillation of the x -velocity is small in the power and torque rate cases, but is much larger in the shape derivative case due to the large stroking motion of the arms. The non-sinusoidal shape in the shape derivative case results from higher frequency components which can be explained by thinking of a flipping fish tail: for one period of motion the tail produces two thrusts. The varying magnitude of the x -velocity results from the alternating high and low drag associated with the arms being extended out or folded back during the stroke. In general, the higher the wave number and frequency a motion possesses, the smaller the perturbation about the desired average velocity.

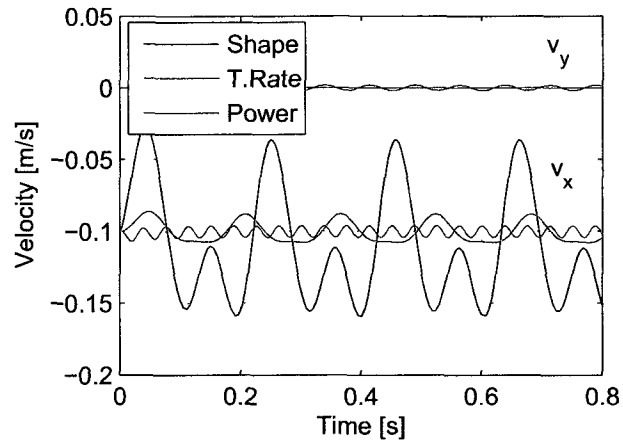


Figure 3.9: Simulated CG velocity

Finally, average x -velocities are summarized in Table 3.3. The “nonlinear v ” and “bilinear v ” indicate the average velocities calculated from simulations of the second equation in (2.3) and (2.6), respectively. For the bilinear rectifier, the simulated average velocities are close to $v = -0.1$ m/s at which the optimal gaits are calculated, despite the fact that oscillations of v around this value are ignored during the optimization. On the other hand, the higher order nonlinearity tends to reduce the actual swim speed. The gaits found from the bilinear rectifier equations may be away from optimality for the original fully nonlinear equations of motion. Nevertheless, the basic gaits thus found do lead to reasonable locomotion of the original system, and may be used as the initial condition for further optimizations that would necessarily be local due to the system complexity.

Table 3.3: Optimal frequencies [rad/s] and simulated velocities [mm/s]

Quantity	Optimal ω	Nonlinear v	Bilinear v
Power	39.7	-69.8	-100.7
Shape Derivative	30.5	-82.8	-107.9
Torque Rate	83.9	-67.4	-100.3

Chapter 4

Flapping-Wing Rectifier

4.1 Flapping-Wing Model

In this section we describe a simple model for flapping-wing rectifiers, develop the equations of motion following the form of the general mechanical rectifier developed in section 2.1.1, and illustrate the biological parameters used in the model.

4.1.1 Overview

The model consists of a main body featuring full rigid-body rotational and translational dynamics, with independent discretized wings. Each wing is described by the displacement of n_p discrete points, located at the intersections of a body-fixed grid and representing the joints between neighboring segments, which can be seen in Fig. 4.1. The coordinate system is defined so that, at the nominal condition, the body lies on the (x,y) plane with the y -axis being the direction of swimming and the z -axis being vertical. We define $\phi_b \in \mathbb{R}^3$ as the vector of body orientation variables, which are Euler angles relating the inertial axes to the principle axes of the main body in the $(z-y-x)$ convention, describing yaw α_b , roll β_b , and pitch γ_b , as depicted in Fig. 4.2. Lastly, we define $r_b \in \mathbb{R}^3$ as the Cartesian coordinates of the main body in the global frame.

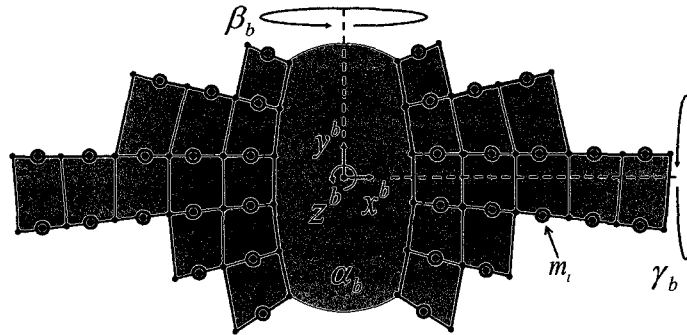


Figure 4.1: Flapping-wing system with point mass wings.

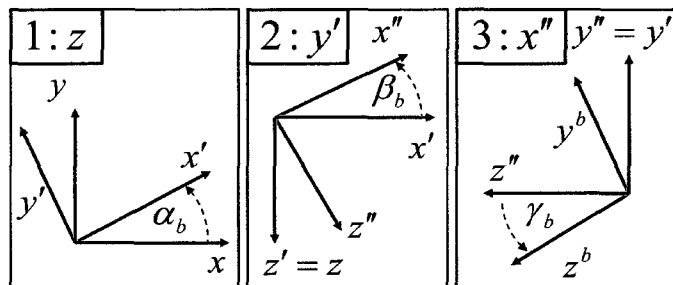


Figure 4.2: Euler angle convention.

There are several notations in the following sections describing the coordinate systems and variable structures: a superscript of b denotes that the quantity is being described in the body-fixed Cartesian coordinate system, denoted by (x^b, y^b, z^b) ; a subscript of i, j denotes the two-dimensional index of a point on a wing in the i^{th} row and j^{th} column, with $j = 0$ indicating the joints connecting the body and wing; a single subscript of i denotes the general index of a point, ranging from 1 to n_p . The position of the i^{th} joint in the body frame is thus given by $r_i^b := (x_i^b, y_i^b, z_i^b)$, with the collection of all joint positions given by $r^b := \text{col}(x^b, y^b, z^b) \in \mathbb{R}^{3n_p}$ in the body frame and $r := \text{col}(x, y, z) \in \mathbb{R}^{3n_p}$ in the inertial frame.

We approximate each segment with a point mass placed half way between the neighboring joints, and through small angle approximation, constrain the joints and point masses to move in the z^b direction only (i.e. x^b and y^b are constant), as shown in Fig. 4.3. The position

of the $(i, j)^{\text{th}}$ point mass in the body frame is thus given by $r_{p_{i,j}}^b := (r_{i,j}^b + r_{i,j-1}^b)/2$, while r_p^b is the collection over i and j , similar to r^b above. Similarly, we capture the actuation through linear force couples aligned in the z^b direction which act on the curvature of the surface, as shown in Fig. 4.3.

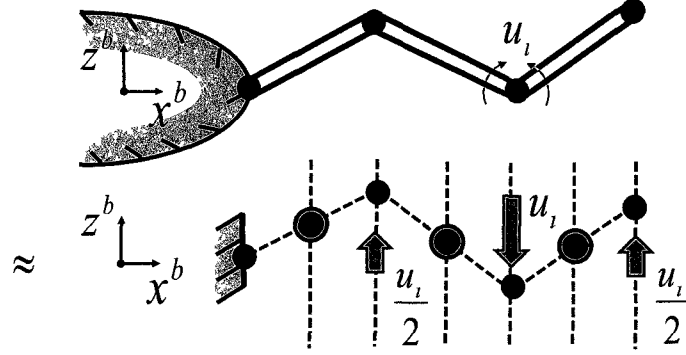


Figure 4.3: Torque approximation.

4.1.2 Equations of motion

We follow the form of the general mechanical rectifier developed in section 2.1.1, where $n := n_p + 6$, $\ell := n_p$, and $\theta := \text{col}(z^b, \phi_b)$.

Kinetic and potential energy

To express the kinetic (rotational and translational) and potential energies in the generalized coordinates q , we first note that the coordinates of a general three dimensional point expressed in the body frame, p_i^b , are expressed in the inertial frame as

$$p_i = R_{\phi_b}^T p_i^b + r_b, \quad R_{\phi_b}^T := R_z(\alpha_b) R_y(\beta_b) R_x(\gamma_b),$$

where R_x , R_y , and R_z are rotation matrix functions given by

$$R_x := \begin{bmatrix} 1 & 0 & 0 \\ 0 & \cos & -\sin \\ 0 & \sin & \cos \end{bmatrix} \quad R_y := \begin{bmatrix} \cos & 0 & \sin \\ 0 & 1 & 0 \\ -\sin & 0 & \cos \end{bmatrix} \quad R_z := \begin{bmatrix} \cos & -\sin & 0 \\ \sin & \cos & 0 \\ 0 & 0 & 1 \end{bmatrix}.$$

We can then express the angular velocity of the body in the body frame as

$$\omega_b^b = \dot{\alpha}_b R_{\phi_b} \bar{e}_3 + \dot{\beta}_b R_x(\gamma_b)^\top R_y(\beta_b)^\top \bar{e}_2 + \dot{\gamma}_b R_x(\gamma_b)^\top \bar{e}_1 = R_{\omega_b^b} \dot{\phi}_b,$$

$$R_{\omega_b^b} := \begin{bmatrix} -\sin \beta_b & 0 & 1 \\ \cos \beta_b \sin \gamma_b & \cos \gamma_b & 0 \\ \cos \beta_b \cos \gamma_b & -\sin \gamma_b & 0 \end{bmatrix},$$

where $\bar{e}_i \in \mathbb{R}^3$ is a vector of zeros with a 1 in the i^{th} location. We note that center of mass is given by

$$mw = m_b r_b + \sum_{i=1}^{n_p} m_i r_{p_i},$$

where m_i is the mass of point mass i and m_b is the mass of the main body. The body and point mass coordinates in terms of the center of mass are then given by

$$r_b = r_t - \frac{1}{m} (I_3 \otimes m_p^\top) (R_{\phi_b} \otimes I_{n_p}) r_p^b, \quad (4.1)$$

and

$$r_p = E_m (R_{\phi_b} \otimes I_{n_p}) r_p^b + (I_3 \otimes e) w, \quad (4.2)$$

where $I_x \in \mathbb{R}^{x \times x}$ is an identity matrix and

$$E_m := I_{3n_p} - \frac{1}{m} (I_3 \otimes e) (I_3 \otimes m_p^\top), \quad m := m_b + \sum_{i=1}^{n_p} m_i$$

$$e := \text{col}(1, \dots, 1) \in \mathbb{R}^{n_p}, \quad m_p := \text{col}(m_1, \dots, m_{n_p}).$$

Finally, we may now express the kinetic and potential energies as

$$\begin{aligned}
T &= \frac{1}{2} \left((\omega_b^b)^\top J_b^b \omega_b^b + m_b \dot{r}_b^\top \dot{r}_b + \sum_{i=1}^{n_p} m_i \dot{r}_{p_i}^\top \dot{r}_{p_i} \right) \\
&= \begin{bmatrix} \dot{\theta} \\ \dot{w} \end{bmatrix}^\top \begin{bmatrix} J(\theta) & 0 \\ 0 & mI_3 \end{bmatrix} \begin{bmatrix} \dot{\theta} \\ \dot{w} \end{bmatrix} \\
V &= \frac{1}{2} z^{b^\top} K z^b,
\end{aligned} \tag{4.3}$$

where we assumed that the system is neutrally buoyant and thus ignored potential energy due to gravity, and $J_b^b = \text{diag}(J_x, J_y, J_z)$ is the diagonal inertia matrix of the body about the principal axes. The stiffness matrix K is derived below, as it relies on the surface normal definition.

Surface normal and environmental force

We approximate the forces exerted by the environment on the wings as static functions of the normal and tangential velocity of the wing surface, and make linear approximations of the static force functions to capture, at least qualitatively, the anisotropy property (easier to slide in the tangential direction than in the normal direction), which was discussed in Chapter 2 to be important for mechanical rectification. Added mass and vorticity effects, which could also be important, are not captured by the current model.

For each mass, the plane normal to the wing surface is determined from the coordinates of the surrounding masses as the sum of the surrounding triangular areas shown in Fig. 4.4. The normal vector for point mass i, j is thus given by

$$n_{i,j}^b := \frac{n_r \times n_u + n_u \times n_\ell + n_\ell \times n_d + n_d \times n_r}{|n_r \times n_u + n_u \times n_\ell + n_\ell \times n_d + n_d \times n_r|}, \tag{4.4}$$

where

$$n_u := r_{p_{i-1,j}}^b - r_{p_{i,j}}^b, \quad n_d := r_{p_{i+1,j}}^b - r_{p_{i,j}}^b, \quad n_\ell := r_{i,j-1}^b - r_{p_{i,j}}^b, \quad n_r := r_{i,j}^b - r_{p_{i,j}}^b.$$

For a point mass on the edge of the wing where n_d or n_u does not exist, we substitute $-n_u$ or $-n_d$, respectively.

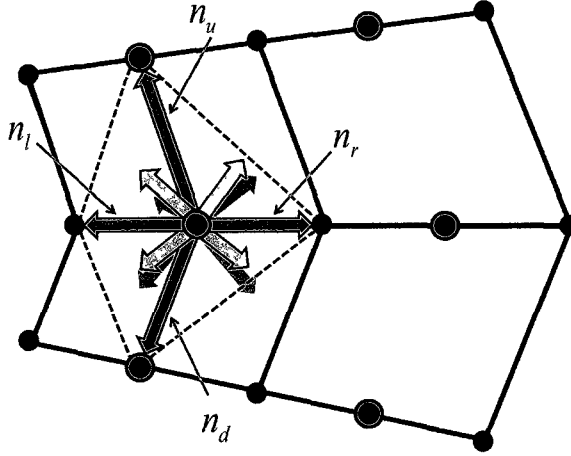


Figure 4.4: Normal vectors for point mass i .

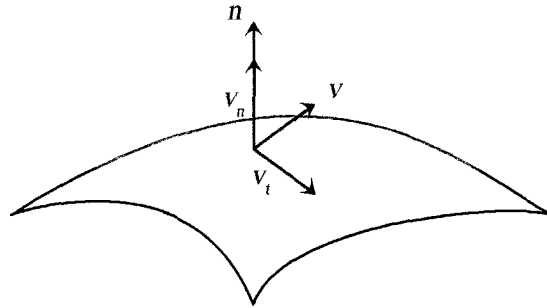


Figure 4.5: Surface normal and velocity projections.

The velocity vector for each mass is projected into the normal and tangential directions as shown in Fig. 4.5, and then multiplied by the normal and tangential coefficient to obtain

the fluid force acting on each mass in the normal and tangential directions, respectively.

The virtual work due to the environmental fluid force is thus

$$\begin{aligned}
\delta W_e &= \sum_{i=1}^{n_p} (\delta q)^\top \left(\frac{\partial r_{p_i}}{\partial q} \right)^\top f_i, \quad f_i := f_{n_i} + f_{t_i}, \\
f_{n_i} &:= -c_{n_i} v_{n_i}, \quad f_{t_i} := -c_{t_i} v_{t_i}, \\
v_{n_i} &:= R_{\phi_b}^\top P_{n_i}^b R_{\phi_b} \dot{r}_{p_i}, \quad v_{t_i} := R_{\phi_b}^\top (I_3 - P_{n_i}^b) R_{\phi_b} \dot{r}_{p_i}, \\
P_{n_i}^b &:= n_i^b (n_i^b)^\top / (n_i^b)^\top n_i^b,
\end{aligned} \tag{4.5}$$

where, for point mass i , $f_i \in \mathbb{R}^3$ is the vector of (x,y,z) force components, $f_{n_i} \in \mathbb{R}^3$ and $f_{t_i} \in \mathbb{R}^3$ are the normal and tangential environmental force components, $v_{n_i} \in \mathbb{R}^3$ and $v_{t_i} \in \mathbb{R}^3$ are the normal and tangential velocities, c_{n_i} and c_{t_i} are the normal and tangential coefficients, and $P_{n_i}^b \in \mathbb{R}^{3 \times 3}$ is the surface normal projection matrix in the body frame.

The environmental force is thus approximated as

$$\sum_{i=1}^{n_p} \left(\frac{\partial r_{p_i}}{\partial q} \right)^\top f_i \approx \begin{bmatrix} D_1 & A(\vartheta) \\ A(\vartheta)^\top & Q(\vartheta) \end{bmatrix} \begin{bmatrix} \dot{\vartheta} \\ \dot{w} \end{bmatrix}$$

through the Taylor series expansion and summation of each term over i .

Stiffness and damping

The slope of the surface at each point mass is determined from the normal vector through normalization so that the third entry is -1 . The linearized surface slope of point mass i, j in the x and y directions are thus given by the first and second entries of

$$n_{s_{i,j}}^b \approx \begin{bmatrix} \frac{(y_d - y_u)(z_\ell - z_r) + (y_r - y_\ell)(z_d - z_u)}{(x_u - x_d)(y_\ell - y_r) + (x_\ell - x_r)(y_d - y_u)} \\ \frac{(x_u - x_d)(z_\ell - z_r) + (x_\ell - x_r)(z_d - z_u)}{(x_u - x_d)(y_\ell - y_r) + (x_\ell - x_r)(y_d - y_u)} \\ -1 \end{bmatrix}, \tag{4.6}$$

where x_u, x_d, x_ℓ , and x_r , and similarly for y_* and z_* , correspond to the x, y , and z , entries of the n_u, n_d, n_ℓ , and n_r vectors given by equation 4.4. The curvature is measured using the second derivatives of the surface (due to the small angle approximations), between two neighboring point masses. For point mass (i, j) , the curvature is calculated along row i by comparison with point $(i, j - 1)$, and is calculated along column j by comparison with point $(i - 1, j)$. The surface curvatures for point mass (i, j) are thus given by

$$c_{i,j,a,b} := c_{xx} + c_{xy} + c_{yx} + c_{yy},$$

where $(a, b) := (i, j - 1)$ and $(i - 1, j)$ for calculating the row and column curvatures, respectively, and

$$c_{xx} := \frac{s_{x_{i,j}} - s_{x_{a,b}}}{x_{i,j} - x_{a,b}}, \quad c_{xy} := \frac{s_{x_{i,j}} - s_{x_{a,b}}}{y_{i,j} - y_{a,b}},$$

$$c_{yx} := \frac{s_{y_{i,j}} - s_{y_{a,b}}}{x_{i,j} - x_{a,b}}, \quad c_{yy} := \frac{s_{y_{i,j}} - s_{y_{a,b}}}{y_{i,j} - y_{a,b}},$$

$$s_{x_{i,j}} := n_{s_{i,j}}^b(1), \quad s_{y_{i,j}} := n_{s_{i,j}}^b(2), \quad x_{i,j} := r_{i,j}^b(1), \quad y_{i,j} := r_{i,j}^b(2),$$

and the slopes s for $j = 0$ are defined to be zero.

The potential energies due to the curvatures along the rows and columns are similarly given by

$$PE_{i,j,a,b} := \frac{1}{2}k(x_{i,j,a,b}, y_{i,j,a,b})c_{i,j,a,b}, \quad (4.7)$$

where $k(x_{i,j,a,b}, y_{i,j,a,b})$ is the stiffness of the wing between point (i, j) and (a, b) (value determined in the following section), and

$$x_{i,j,a,b} := (x_{i,j} - x_{a,b})/2, \quad y_{i,j,a,b} := (y_{i,j} - y_{a,b})/2.$$

Finally, the matrix K in equation 4.3 is obtained by summation over i and j of the potential

energy coefficients, due to surface curvature along the row and column, given by

$$K := \sum_{i,j} \frac{\partial^2 PE_{i,j,i,j-1}}{\partial z^b \partial z^b} + \sum_{i,j} \frac{\partial^2 PE_{i,j,i-1,j}}{\partial z^b \partial z^b}. \quad (4.8)$$

The curvature damping matrix $D_2 := d_2 K$ is proportional to K through the constant d_2 .

Actuation

The internal forces as depicted in Fig. 4.3 act on the curvature measured along each row i given by

$$c_{rr} := TTz^b, \quad T := \text{diag}(T_1, \dots, T_{n_r}), \quad T_i := I_{n_{r_i}} - \begin{bmatrix} 0 \\ I_{(n_{r_i}-1)} \end{bmatrix},$$

where n_r is the number of rows and n_{r_i} is the number of point masses in row i . The virtual work due to internal actuation is thus

$$\delta W_a = (\delta\theta)^\top \left(\frac{\partial c_{rr}}{\partial \theta} \right)^\top u = (\delta\theta)^\top B u, \quad B := \begin{bmatrix} T^\top T^\top \\ 0 \end{bmatrix}. \quad (4.9)$$

4.1.3 Model parameters

The fluid forces are approximated based on theory by [89], adjusted for undulator swimming by [97], with separate coefficients for the tangential and normal directions. We examine five systems, a high-aspect-ratio and low-aspect-ratio rectangular wing, and an Atlantic, Butterfly, and Cownose ray. The wing and body density is approximated as the density of water. The wing shapes and thicknesses for the batoid models were mapped using provided data [80]. The nominal model parameters are given by

$$\begin{aligned}
c_{n_i} &= \frac{3\rho v_z d^2}{2} \text{ Ns/m} & c_{t_i} &= \frac{2.7d\sqrt{\rho\mu d v_z}}{2} \text{ Ns/m} & \rho &= 1000 \text{ kg/m}^3 \\
a_b &= \frac{0.003\rho v_y A_b}{2} \text{ Ns/m} & m_i &= \rho d^2 t(x_{p_i}^b, y_{p_i}^b) \text{ kg} & \mu &= 10^{-3} \text{ Ns/m}^2 \\
v_z &= 0.4 \text{ m/s} & w_b &= 0.06 \text{ m} & v_y &= 2\ell_b \text{ m/s} \\
d &= 0.01 \text{ m} & A_b &= w_b \ell_b \text{ m}^2
\end{aligned}$$

where $\ell_b = 0.2 \text{ m}$, 0.15 m , and 0.15 m , is the approximate length of the main body for the Atlantic, Butterfly, and Cownose rays, respectively, c_{n_i} and c_{t_i} is the normal and tangential coefficient of friction for point mass i , a_b is the drag coefficient for the main body, m_i is the mass of point mass i , ρ is the density of water, μ is the viscosity of water, d is the distance between point masses, A_b is the main body area, v_z is the approximate operating region for the normal wing velocity, t_w is the wing thickness, w_b is the body width, and v_y is the average steady-state velocity.

Joint locations

Figure 4.6 shows the locations of the wing joints measured from biology for the three batoid species. We use two gridding schemes: a rectangular grid and a more realistic radial grid. The starting joint positions and point mass counts for the rectangular grid are listed in Table. 4.1, where $x_{i,0}^b = 3 \text{ cm}$ for all rows. The starting joint positions, point mass counts, and row angles for the radial grid are listed in Table. 4.2. Additionally, we generate a slightly shifted grid for the Cownose ray so that the joint staggering pattern more closely matches biology, in that the j^{th} joint in the i^{th} row is closer to the body than the corresponding joint in row $i - 1$. Figure 4.7 depicts the resulting batoid grids.

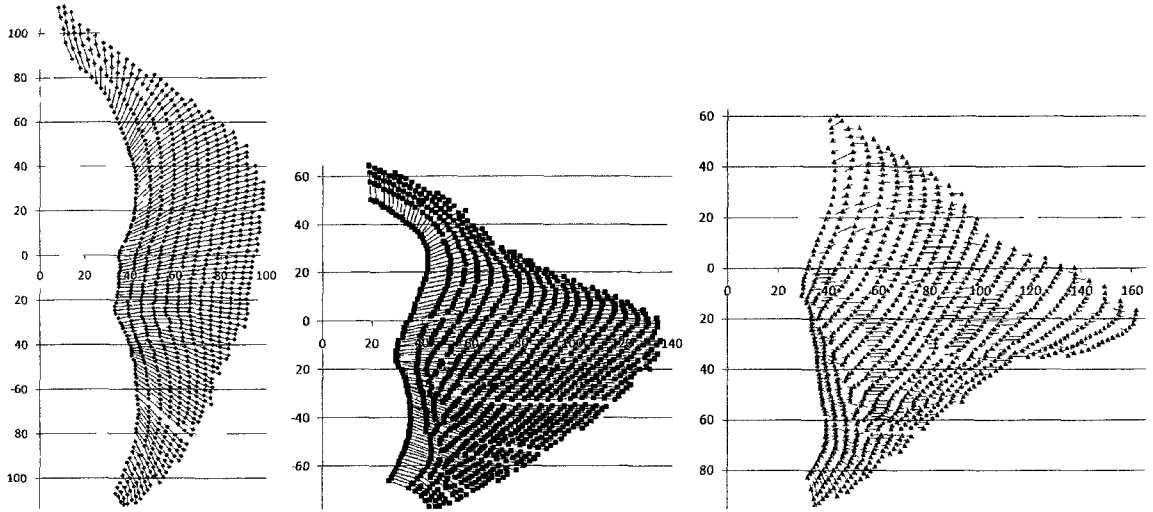


Figure 4.6: Atlantic, Butterfly, and Cownose joint locations, [mm].

$y_{i,0}^b$ [mm]	n_{r_i}		
	Atlantic	Butterfly	Cownose
90	1		
80	2		
70	4		
60	5	1	1
50	6	2	3
40	7	3	4
30	7	4	6
20	7	6	7
10	7	9	8
0	6	10	11
-10	6	10	12
-20	6	10	13
-30	6	9	13
-40	5	8	8
-50	5	7	6
-60	5	5	5
-70	4	3	4
-80	4	1	3
-90	3		2
-100	2		
-110	1		

Table 4.1: Starting joint positions and point mass counts for rectangular wing grids.

$y_{i,0}^b$ [mm]	$x_{i,0}^b$ [mm]		n_{r_i}		Row angle, θ_i [rad]	
	Atlantic	Cownose	Atlantic	Cownose	Atlantic	Cownose
90	10		2		1.57	
80	20		2		1.57	
70	30		3		1.33	
60	35	40	3	1	1.11	0.79
50	40	41	4	2	0.79	0.00
40	40	42	5	3	0.46	0.11
30	40	42	6	4	0.38	0.20
20	40	40	6	6	0.32	0.17
10	40	35	7	7	0.32	0.12
0	35	32	7	11	0.24	0.00
-10	35	30	7	13	0.14	-0.07
-20	35	33	6	13	0.00	-0.07
-30	35	35	5	11	-0.10	-0.03
-40	40	36	4	7	-0.24	0.00
-50	40	38	4	6	-0.46	0.00
-60	40	40	3	3	-0.59	-0.17
-70	40	38	3	2	-0.79	-0.59
-80	40	33	2	1	-1.11	-1.25
-90	40		2		-1.25	
-100	35		1		-1.33	

Table 4.2: Starting joint positions, point mass counts, and row angles for radial wing grids.

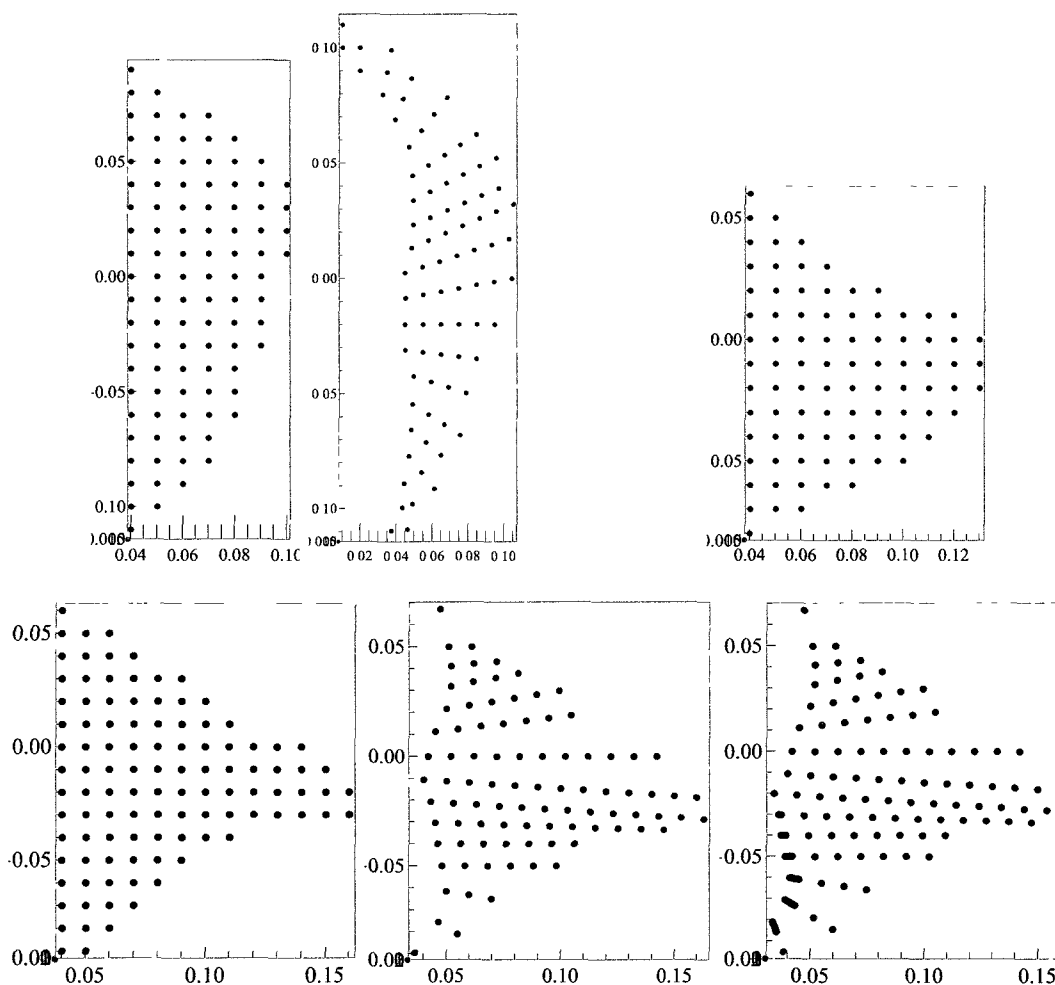


Figure 4.7: Atlantic (rectangular, radial), Butterfly (rectangular), and Cownose (rectangular, radial, and shifted radial) grids.

Wing thickness

Figure 6.1, 6.2, and 6.3 shows the cross sections used to measure the wing thicknesses for the Atlantic, Butterfly, and Cownose rays, respectively, which are summarized in Table 6.1, 6.2, 6.3, 6.4, 6.5, and 6.6. A scaling factor of 0.75, 0.9, and 0.7 was applied to the Atlantic, Butterfly, and Cownose thickness data, respectively, to fit the data to the samples used for the joint data. A function of the form

$$t(x, y) := a_{xx}x^2 + a_{xy}xy + a_{yy}y^2 + a_x x + a_y y + a$$

was then fit to the thickness data (in meters), where the coefficients are given in Table 4.3.

	a_{xx}	a_{xy}	a_{yy}	a_x	a_y	a
Atlantic	2.5524	0.1753	-1.3138	-0.5488	-0.0231	0.0348
Butterfly	0.3345	-0.1943	-1.8787	-0.1591	-0.0101	0.0167
Cownose	1.7524	0.2228	-3.9812	-0.5528	-0.0971	0.0467

Table 4.3: Thickness function coefficients.

Wing stiffness

The stiffness of the body is determined by comparison with a bending test performed on an Atlantic ray [79] shown in Fig. 4.8. The body of the ray is fixed with the wing hanging free to remove the influence of gravity. The tip of the wing is then pulled upward and the force and deflection are measured. We repeat this test numerically on the model using the rectangular grid as shown in Fig. 4.9, and determine a uniform stiffness value, $k(x, y) = 2.2 \times 10^{-7}$ N/m, and a stiffness value proportional to thickness, $k(x, y) = 2.6t(x, y) \times 10^{-5}$ N/m. The thickness-proportional stiffness result is slightly closer to the biology, with slightly steeper deflection near the wing tip, so we use this value for all rectangular grid cases. We repeat the test again using the radial grid as shown in Fig. 4.10, and again determine a uniform stiffness value, $k(x, y) = 9.0 \times 10^{-9}$ N/m, and a stiffness value proportional to thickness, $k(x, y) = 9.2t(x, y) \times 10^{-7}$ N/m, which is used for all radial grid cases. The optimal gait results in the following sections end up being insensitive to the precise stiffness values used. Nearly (and sometimes exactly) identical optimal gaits are produced for stiffness values that are many times higher or lower, due to a combination of the objective functions being independent of stiffness and the requirement that the velocity constraint is satisfied.

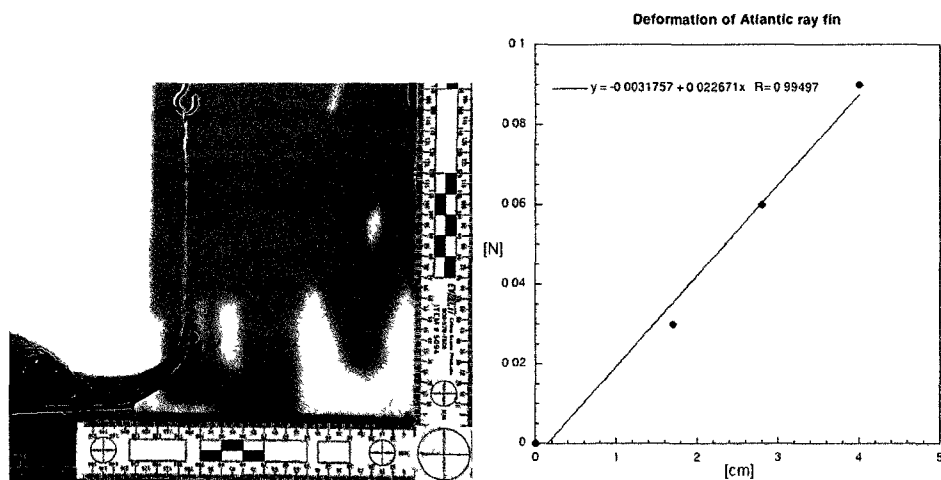


Figure 4.8: Atlantic bending test, gravity is to the right.

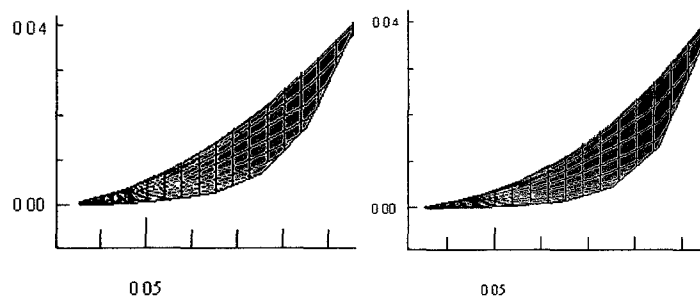


Figure 4.9: Simulated bending test for uniform and thickness-proportional stiffness, rectangular grid.

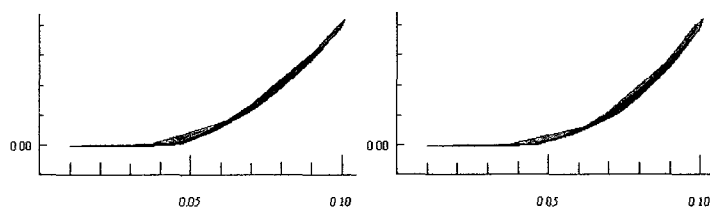


Figure 4.10: Simulated bending test for uniform and thickness-proportional stiffness, radial grid.

4.2 Flapping Gait Analysis

4.2.1 Observed and perturbed gait

The observed biological gaits for each batoid, consisting of oscillation frequency, tip amplitude (measured from the neutral plane), and phase lag down the wing, are summarized in Tab. 4.4 [68].

	ω [rad/s]	Tip Amp. [cm]	Phase Lag [rad]
Atlantic	15.7	3	8
Butterfly	8.38	5	3.8
Cownose	7.85	9	2.5

Table 4.4: Observed gait metrics

We now check the model by imposing an observed body motion and calculating the average steady state velocity. We calculate the average steady state velocity v , for a given motion (ϑ, ω) , from the velocity constraint given by the second line in (3.4), using phasor form and variable definitions in (3.5), as

$$v = \frac{\vartheta^* S(\omega) \vartheta}{\vartheta^* Q_1 \vartheta + 2a_1}. \quad (4.10)$$

Using the data for the Atlantic ray, where we assume a straight phase lag from head to tail and a wing amplitude increasing proportional to x^2 , we calculate the steady state velocity to be 0.27 m/s, which is verified by simulation. This value is roughly half of the observed biological velocity of $v_y = 0.4$ m/s (two body lengths per second), and is insensitive to the value of the fluid coefficients. This is because the dominant terms in both S and Q_1 scale with the normal fluid friction coefficients c_{n_i} , so the ratio of the numerator to the denominator of v is relatively unchanged for any reasonable values of c_n and c_t for a given motion. The observed biological measurements are statistical averages, however, so there

is some freedom in the precise value of the observed ϑ_o vector. To verify that the model is capable of producing the observed biological velocity with a gait that is close to the observed gait, we solve the minimum perturbation problem given by

$$\min_u \|\vartheta - \vartheta_o\|^2 \quad \text{s.t.} \quad \mathbf{v} = v_y, \quad (4.11)$$

with solution given by Lem. 5.

Lemma 5 *Consider the problem (4.11), and variable definitions given by (1). The problem is equivalent to*

$$\min_u \|P(\omega)u - \vartheta_o\|^2 \quad \text{s.t.} \quad u^*Y(\omega)u = 1, \quad (4.12)$$

with solution given by

$$u = (P(\omega)^*P(\omega) + \lambda Y(\omega))^{-1} P(\omega)^*\vartheta_o,$$

where $\lambda \in \mathbb{R}$ is the smallest value found by line search to satisfy $u^*Y(\omega)u = 1$.

Proof. We define the Lagrangian as

$$L := \|P(j\omega)u - \vartheta_o\|^2 + \lambda(u^*Y(\omega)u - 1).$$

The partial derivative is given by

$$\frac{\partial L}{\partial u} = 2P(j\omega)^*(P(j\omega)u - \vartheta_o) + 2\lambda R(j\omega)u,$$

which must equal zero at a local extrema. The solution u is thus obtained as a function of the Lagrange multiplier λ , which is found by line search to satisfy the constraint. ■

The original biological gait and the minimum perturbed gait are shown in Fig. 4.11.

The perturbed gait is able to achieve the observed 2 body lengths per second with minimal changes to the overall gait. The tip amplitude increased slightly from 3 cm to 3.5 cm while the phase lag down the wing changed from a straight phase lag of 8 radians to a more circular phase lag around the wing from head to tail of 8 radians. This circular phase lag is actually more realistic for the Atlantic ray than the original straight phase lag since it more closely matches the actual circular undulation seen in biology.

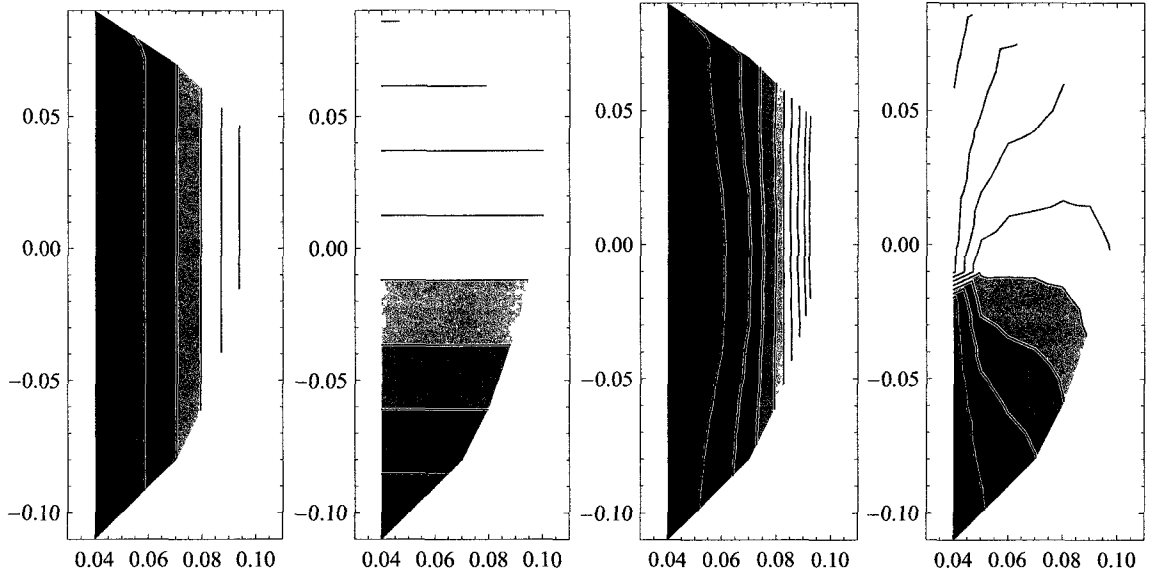


Figure 4.11: Biological gait amplitude and phase contour and perturbed gait amplitude and phase contour for the Atlantic ray.

4.2.2 Effects of wing geometry on basic flapping gaits

In this section we examine the effect of wing aspect ratio on the basic gait for simple flapping-wing rectifiers. We examine each ray with the body fixed to translate only in the y -direction with no rotation, and we apply (2.8) with $\hat{v} := \text{col}(z^b, 0, 0, 0)$, where the denominator is chosen to be a measure of the wing curvature given by

$$\|\hat{\varphi}\|^2 := \hat{v}^* \begin{bmatrix} T_c & 0 \\ 0 & 0 \end{bmatrix} \hat{v},$$

where T_c is similar to the stiffness matrix K , and is given by

$$T_c := \sum_{i,j} \frac{\partial^2 c_{i,j,i,j-1}}{\partial z^b \partial z^b} + \sum_{i,j} \frac{\partial^2 c_{i,j,i-1,j}}{\partial z^b \partial z^b}. \quad (4.13)$$

Figure 4.12 shows four snapshots of the basic gait for the Cownose ray, where each plot corresponds to equally spaced time instants $t = 0$ to $3T/4$. All batoid cases result in similar basic gaits, with amplitudes and phases shown in Fig. 4.13, with additional figures for each case in the appendix ¹. We generally see a flapping gait with a relatively small number of waves down the wing. The amplitude of wing deflection smoothly increases as distance from the body increases, while a traveling wave (as indicated by the phase lag) progresses down the wing from head to tail in a circular fashion, agreeing with the perturbed gait in the previous section. The measured phase lag for each case is summarized in Tab. 4.5. The general trend from the low-aspect Atlantic ray to the high-aspect Cownose rays is a decrease in the phase lag, from 4 radians for the rectangularly gridded Atlantic ray to 1.5 radians for the rectangularly gridded Cownose ray. The radially gridded wings for the Atlantic and Cownose rays were similar at 3 and 2 radians of phase lag, respectively, while the adjusted radially gridded Cownose wing increased slightly to 4 radians.

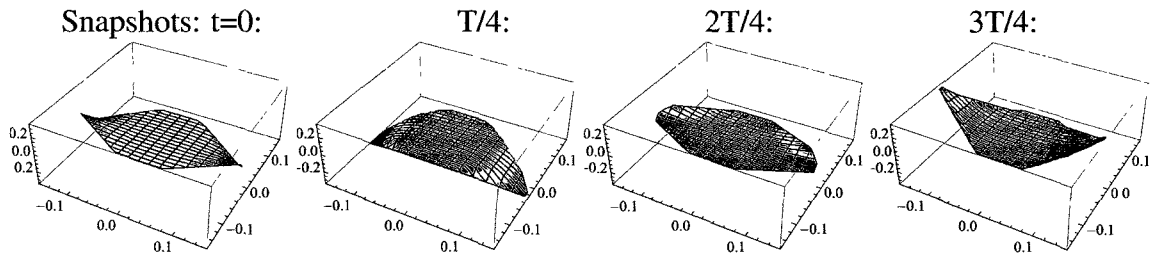


Figure 4.12: Basic gait snapshots for the Cownose ray.

¹Note that due to the fixed body orientation, the wings are independent so the maximum eigenvalue is degenerate and both symmetric and antisymmetric results are equal.

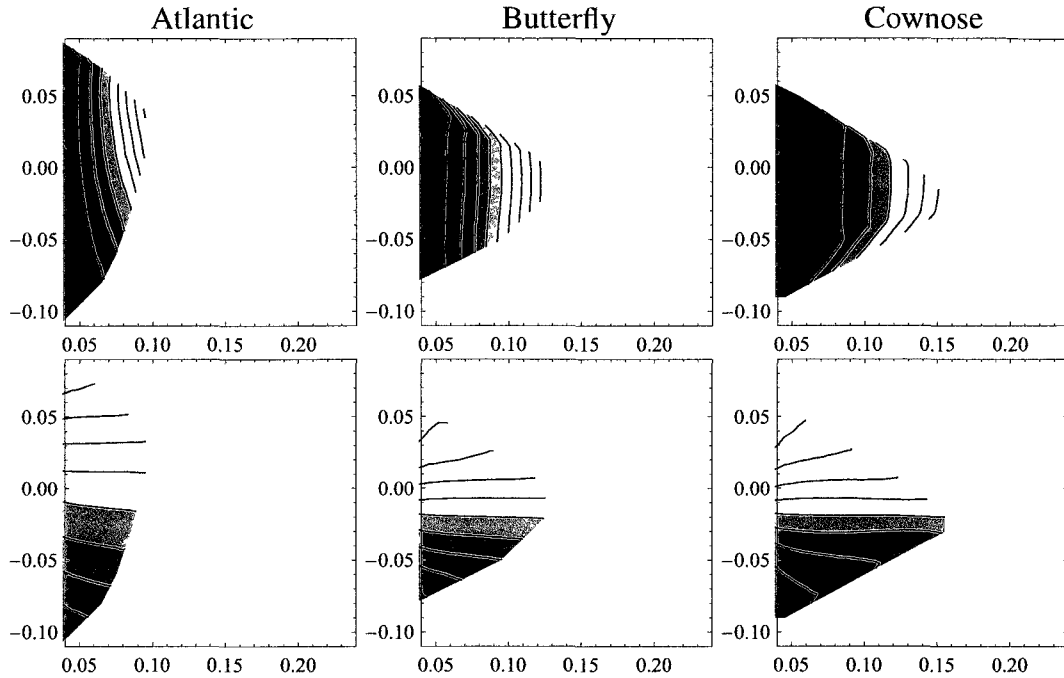


Figure 4.13: Basic gait amplitudes (top) and phases (bottom).

	Atlantic		Butterfly	Cownose		
	Rect.	Radial	Rect.	Rect.	Radial	Radial Shifted
Phase Lag [rad]	4	3	2	1.5	2	4

Table 4.5: Basic gait wing phase lags.

This general trend of decreasing phase lag as wing aspect ratio increases is also seen in the following simple rectangular wing example, where only the c_{xx} and c_{yy} curvatures were retained in the definition of T_c (i.e. ignoring the c_{xy} and c_{yx} terms). Figure 4.14 shows four snapshots of the basic gait for the high aspect ratio case, where each plot corresponds to equally spaced time instants $t = 0$ to $3T/4$. The wing is connected to the body along the lower-left edge (parallel with the y -axis) and the system locomotes in the positive y direction. Similarly, Figs. 4.15 shows the basic gait snapshots for the low aspect ratio case. Figure 4.16 shows the associated amplitude and phase contours for both the high and low aspect cases, with units of meters for amplitude and 2π radians for the phase (i.e. a phase

of 0.5 corresponds to π radians). In the higher aspect ratio plots we see a flapping gait with a relatively small number of waves down the wing. The amplitude of wing deflection smoothly increases as distance from the body increases and a traveling wave progresses from head to tail in a straight fashion, due to the lack of c_{xy} and c_{yx} curvatures in T_c . In the lower aspect ratio plots we see a more undulatory gait with a larger number of waves down the wing, and the general shapes of the amplitude and phase contours are similar between the two cases. We thus observe that a short, low-aspect-ratio wing tends to undulate while a long, high-aspect-ratio wing tends to flap.

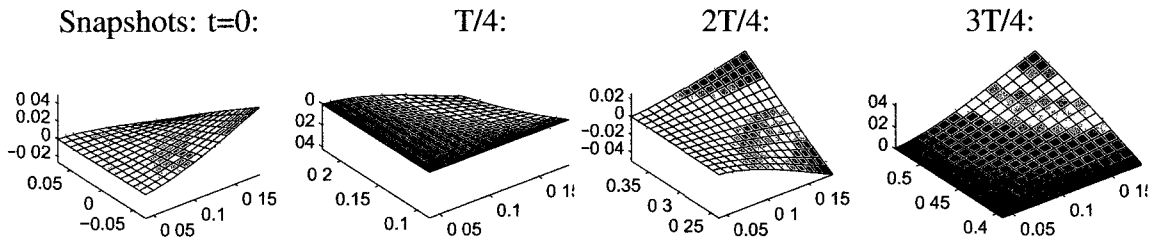


Figure 4.14: High-aspect rectangular wing basic gait snapshots.

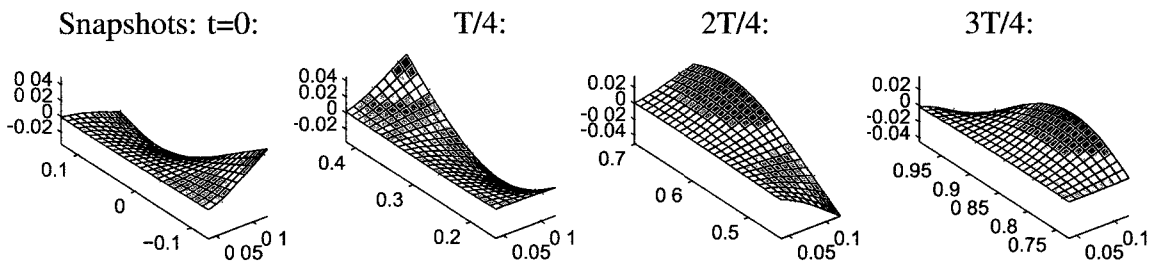


Figure 4.15: Low-aspect rectangular wing basic gait snapshots.

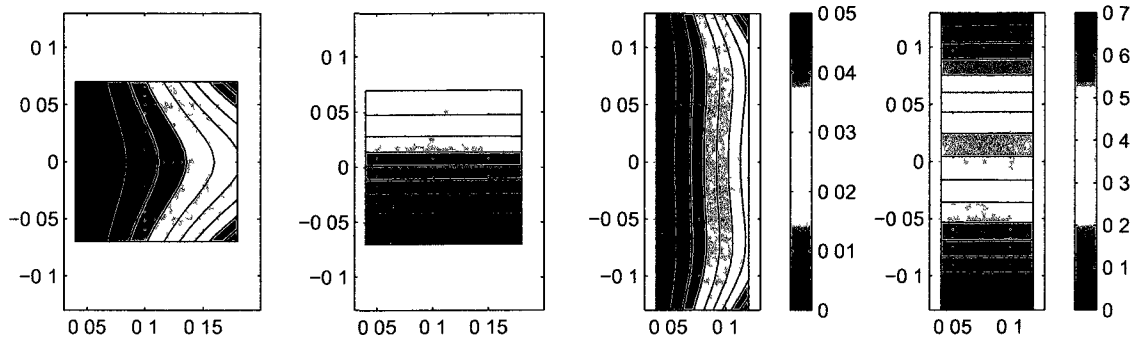


Figure 4.16: High and low-aspect rectangular wing basic gaits (amplitude and phase)

4.2.3 Optimal Gaits

We now examine the optimal gaits for each batoid system by solving (3.4) where we choose the objective functions to be a measure of the wing curvature, curvature rate, power, actuation, or actuation rate, through the choice of Π following Tab. 3.1, where $W^T W = T_c$ following (4.13). We first impose the observed biological oscillation frequency and calculate the gaits which minimize each objective function at that frequency. We then allow the frequency to vary and find the globally optimal frequency and examine the resulting gaits. Key figures are shown below for clarity, while additional plots of the objective functions vs frequency, amplitude, phase, and motion snapshots for each case are shown in the appendix, with Tables 6.8 to 6.19 listing the measured optimal frequency, tip amplitude, and phase lag down the wing for each case.

Observed biological oscillation frequency

We now set the oscillation frequency for each case to the observed biological oscillation frequency (biological gait measurements are listed in Tab. 4.4), and recalculate the curvature, power, and actuation minimizing gaits. Figure 4.17 shows four snapshots of the minimum curvature gaits for the rectangularly gridded Atlantic, Butterfly, and Cownose rays, where each plot corresponds to equally spaced time instants $t = 0$ to $3T/4$, while Fig. 4.19 and Fig. 4.20 show the gait snapshots for the minimum power and actuation gaits,

respectively, and Fig. 4.18 shows the associated amplitude and phase contour plots for the minimum curvature gait.

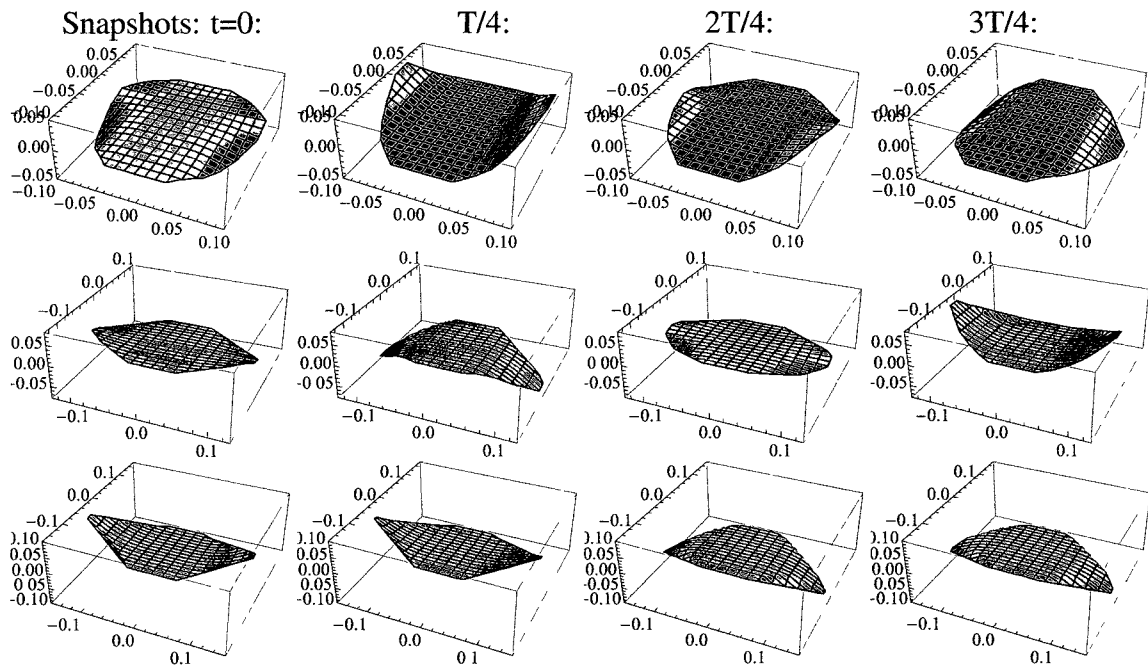


Figure 4.17: Minimum curvature gait snapshots for the Atlantic (top), Butterfly (mid), and Cownose (bottom) rays, rectangular grid.

All plots are in the body frame. The resulting gaits show symmetric, oscillatory (or flapping), motion with some slight body pitching (not shown), due to the heaving motion of the wings. Rolling is not observed due to the symmetric flapping. The general shape of the phases and amplitudes for the minimum curvature case are similar to the basic gait results, with a phase lag (or wave) propagating from head to tail along each wing in a roughly circular fashion. The tip amplitudes for all three objective functions are roughly 4-4.5 cm, 7-9 cm, and 8-10 cm, for the Atlantic, Butterfly, and Cownose rays, respectively, which is in reasonably good agreement with the 3 cm, 5 cm, and 9 cm tip amplitudes observed in biology. All of the gaits are oscillatory, with fairly small phase lags down the wing of 1.5-2.5 radians, 1-1.5 radians, and 0.5-1 radians, respectively, which are less than the 8 radians (undulatory), 3.8 radians (oscillatory), and 2.5 radians (oscillatory) observed in biology.

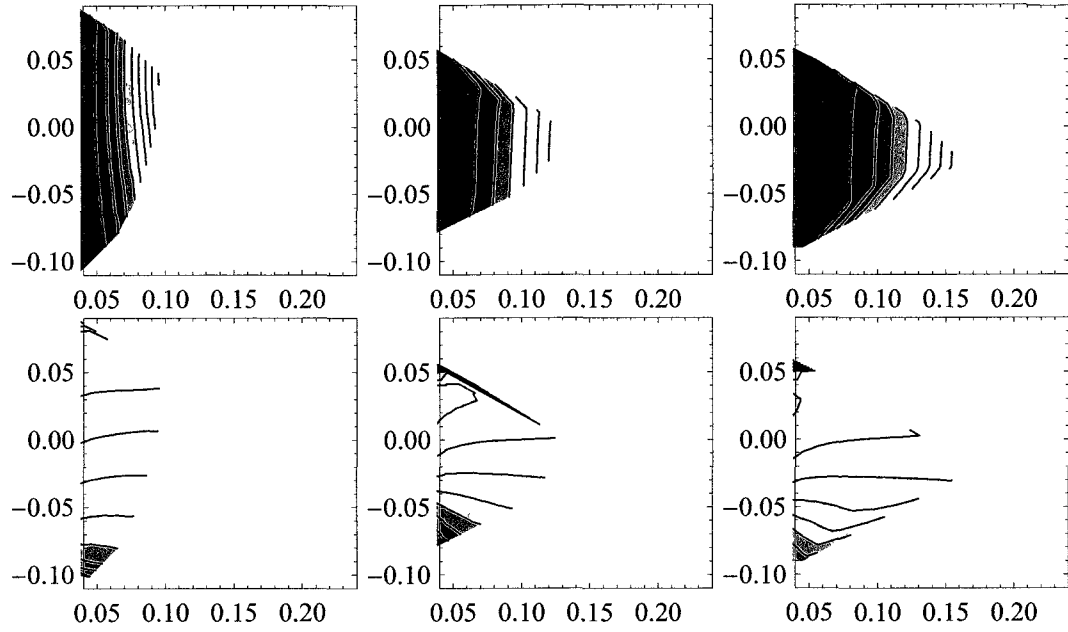


Figure 4.18: Minimum curvature gait amplitude (top) and phase (bottom) contour plots for the Atlantic (left), Butterfly (mid), and Cownose (right) rays, rectangular grid.

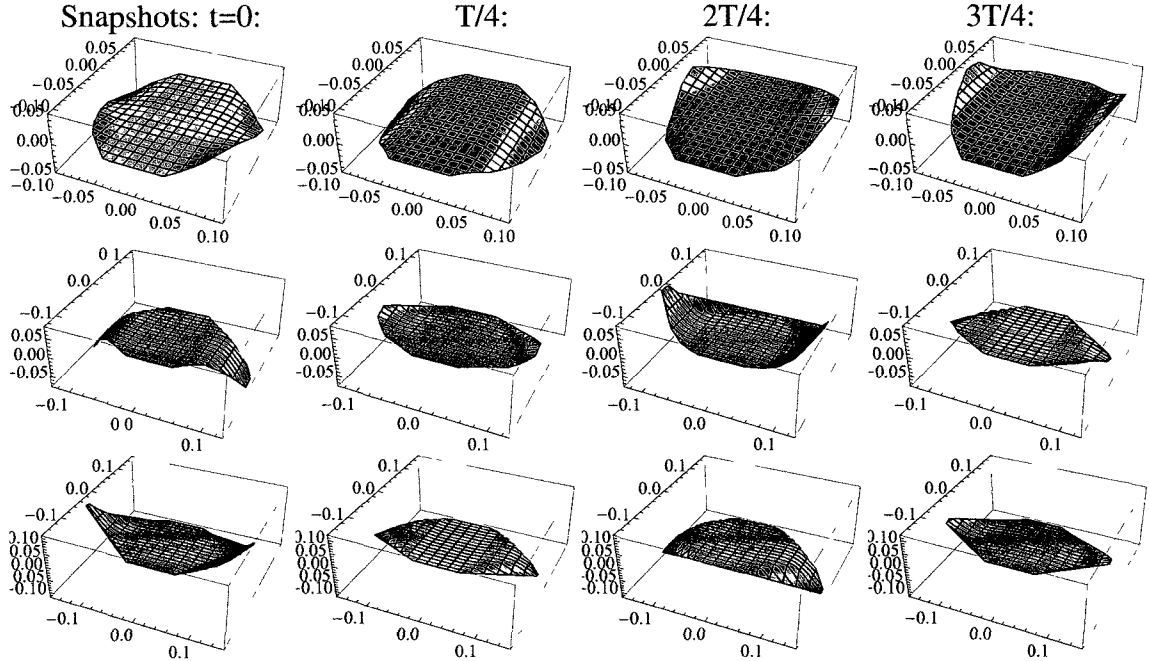


Figure 4.19: Minimum power gait snapshots for the Atlantic (top), Butterfly (mid), and Cownose (bottom) rays, rectangular grid.

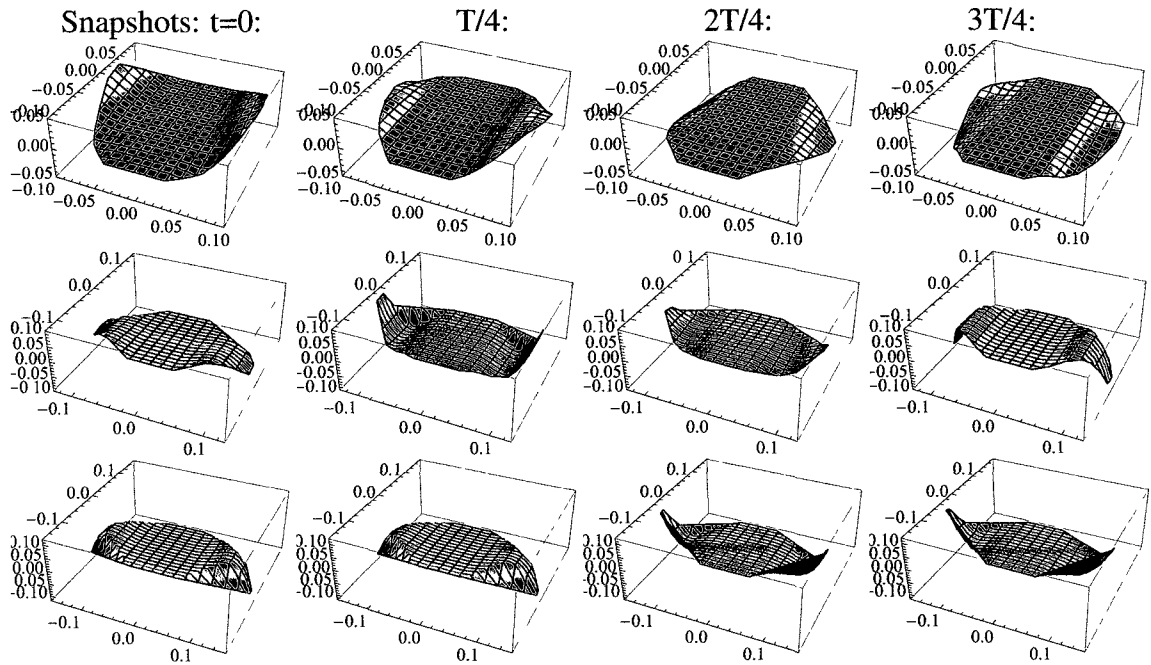


Figure 4.20: Minimum actuation gait snapshots for the Atlantic (top), Butterfly (mid), and Cownose (bottom) rays, rectangular grid.

Of particular interest are the minimum actuation gaits, where we can see that different natural modes are being excited to generate the flapping motion. Figure 4.21 shows two snapshots of the first and fifth natural modes for the Atlantic ray and Butterfly ray, and the associated minimum actuation snapshots, respectively. We can see that, for the Butterfly and Cownose rays, the actuation is taking advantage of the stiffness in the wing to excite the fifth natural mode to produce most of the flapping motion, where the body of the wing and the tip of the wing are mostly out of phase. For the Atlantic ray, with the lower aspect ratio wings, we see that the first natural mode is being excited. For those further interested, a full list of the first ten natural modes of each system is included in the appendix.

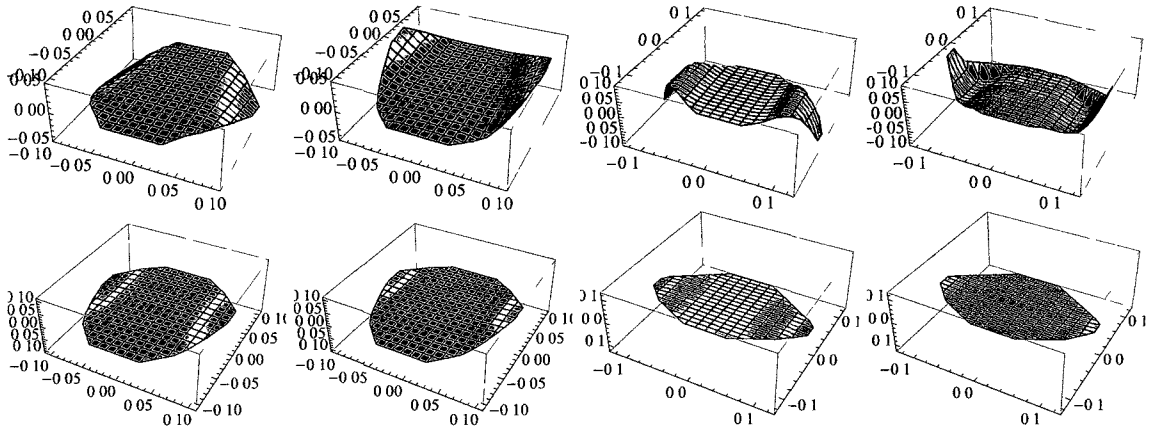


Figure 4.21: Two snapshots of the minimum actuation gait (top) and associated natural mode (bottom), 1st mode Atlantic ray (left), 5th mode Butterfly ray (right).

We now examine the radially gridded cases. For the curvature and power cases, for the Atlantic ray, we obtain slightly larger tip amplitudes than the rectangularly gridded case, increasing to approximately 5 cm, with slightly smaller wing phase lags of 0.5 to 1.5 radians. For the curvature rate and power cases, for the Cownose ray, we obtain similar tip amplitudes of 8 cm, with slightly larger phase lags of approximately 2 radians. The most interesting case, however, is the actuation, where we obtain a sudden change from symmetric to anti-symmetric motion, with an associated increase in tip amplitude to 10 cm and 15 cm for the Atlantic and Cownose rays, respectively, and a decrease in the wing phase lag to almost zero. Figure 4.22 shows four snapshots of the minimum curvature gaits for the radially gridded Atlantic and Cownose rays, where each plot corresponds to equally spaced time instants $t = 0$ to $3T/4$. Furthermore, these gaits also correspond to natural modes, in this case the second natural mode is being excited.

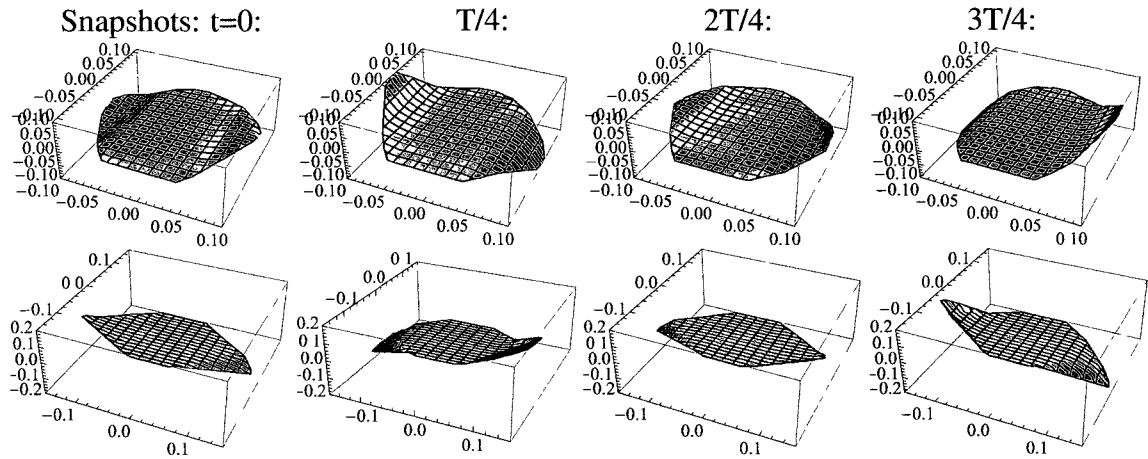


Figure 4.22: Minimum actuation gait snapshots for the Atlantic ray (top) and Cownose ray (bottom), radial grid.

Globally optimal oscillation frequency

For all systems, wing curvature goes to zero as the frequency of oscillation goes to infinity, while the minimum actuation results in a globally optimal frequency many times higher (>50 rad/sec) than the observed biological oscillation frequency. Minimum actuation rate, however, results in very small globally optimal frequencies (roughly 0.5 to 4.5 rad/sec) with very large amplitude (200 to 20 cm, respectively). This indicates that these objective values are unlikely candidates for actual batoid swimming.

For the rectangularly gridded systems, the minimum curvature rate and minimum power cases result in optimal frequencies of approximately 9 to 12 rad/s and 17 to 21 rad/s, respectively. These values are fairly close to the approximate 8 to 15 rad/s oscillation frequency observed in biology for the Atlantic and Cownose rays, respectively. Figure 4.23 shows four snapshots of the minimum curvature rate gait for the Cownose system, where each plot corresponds to equally spaced time instants $t = 0$ to $3T/4$, while Figure 4.24 shows the associated amplitude and phase contour plots.

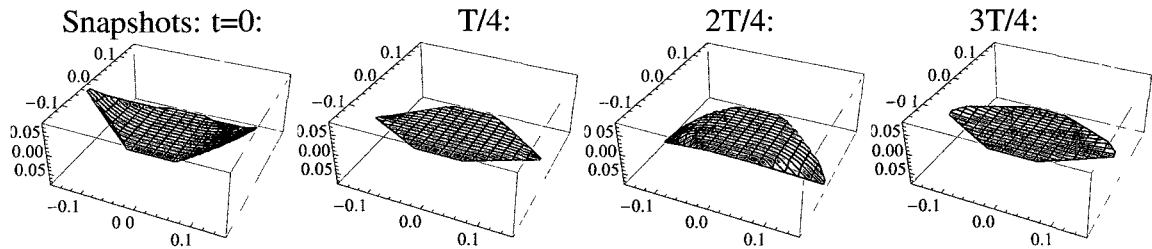


Figure 4.23: Minimum curvature rate gait snapshots, Cownose, rectangular grid.

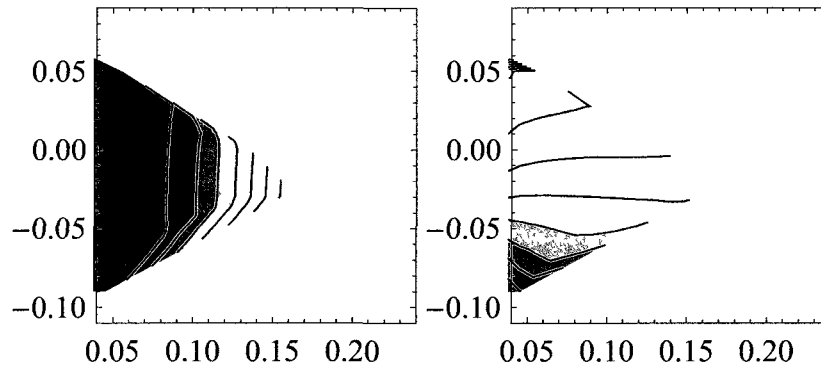


Figure 4.24: Amplitude and phase contour plots for the minimum curvature rate gait, Cownose, rectangular grid.

All plots are in the body frame. The optimal gait is a symmetric, oscillatory (or flapping), motion with some slight body pitching (not shown), due to the heaving motion of the wings. Rolling is not observed due to the symmetric gait. The general shape of the phases and amplitudes are similar to the basic gait results, with a phase lag (or wave) propagating from head to tail along each wing in a circular fashion. These plots are also representative of the Butterfly ray optimal gait, since both systems share a similar high aspect ratio wing. For both cases, the minimum power objectives result in phase lags down the wing of approximately 2 radians with tip amplitudes of 2.5 to 3.5 cm, while the minimum curvature rate case results in phase lags of 1.5 radians with tip amplitudes of 5 cm. These results are oscillatory and fairly close to the observed phases and amplitudes of 3.8 radians and 5 cm for the Butterfly and 2.5 radians and 9 cm for the Cownose.

We now examine the low aspect ratio, rectangularly gridded Atlantic system. Fig-

Figure 4.25 shows four snapshots of the minimum power gait for the Atlantic system, where each plot corresponds to equally spaced time instants $t = 0$ to $3T/4$, while Figure 4.26 shows the associated amplitude and phase contour plots.

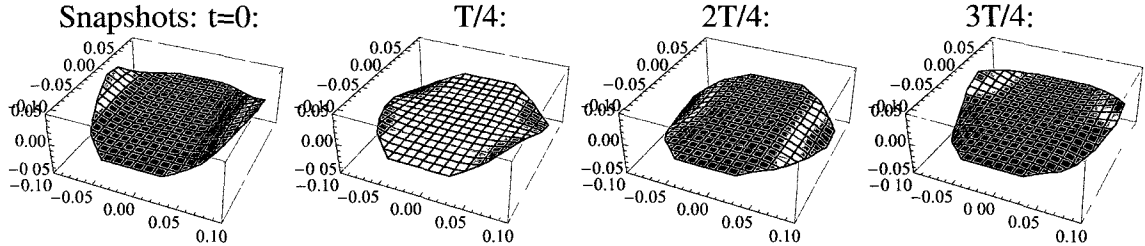


Figure 4.25: Minimum power gait snapshots, Atlantic, rectangular grid.

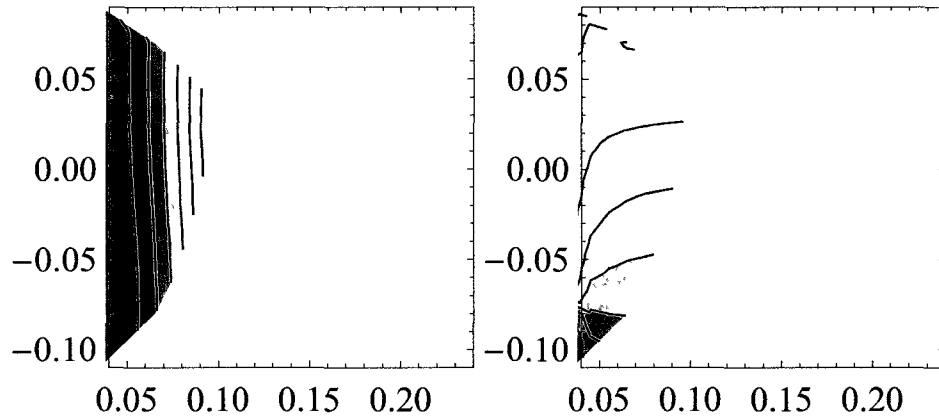


Figure 4.26: Amplitude and phase contour plots for the minimum power gait, Atlantic, rectangular grid.

The minimum power case results in a 2 radians phase lag down the wing and 3 cm tip amplitude, while the minimum curvature rate case results in 1 radian phase lag and 6 cm tip amplitude. While the optimal tip amplitudes are close to the observed biological tip amplitude of 3 cm, the optimal phase lag is much more oscillatory than the observed undulation of 8 radians.

Varying the internal structure to more closely match the biological radial angles, the tip amplitudes for the Atlantic ray increase to 20 cm and 8 cm for the minimum curvature rate and minimum power gaits, respectively, while the phase lag decreases to roughly 0.25 to

0.5 radians, which is even more oscillatory than the rectangular gridding. This is due to the optimal frequency reducing to 4 rad/s and 10 rad/s, respectively, requiring the subsequent increase in amplitude to maintain velocity. The Cownose case is relatively insensitive to the change, as the radial angles are mostly aligned along the local x axis, and so the optimal frequency, amplitudes, and phases are mostly unchanged.

Hypothesizing that there may be structural limitations in biology that could be captured through an amplitude constraint to improve the optimal gaits, we return to the minimum actuation rate case where originally a large amplitude optimal gait was obtained. We now impose a tip amplitude constraint of 3 cm on the Atlantic ray, using the Pareto-optimal method given by (3.2), and obtain the amplitude (3d plot for clarity), amplitude contour, and phase contour plot shown in Fig. 4.27.

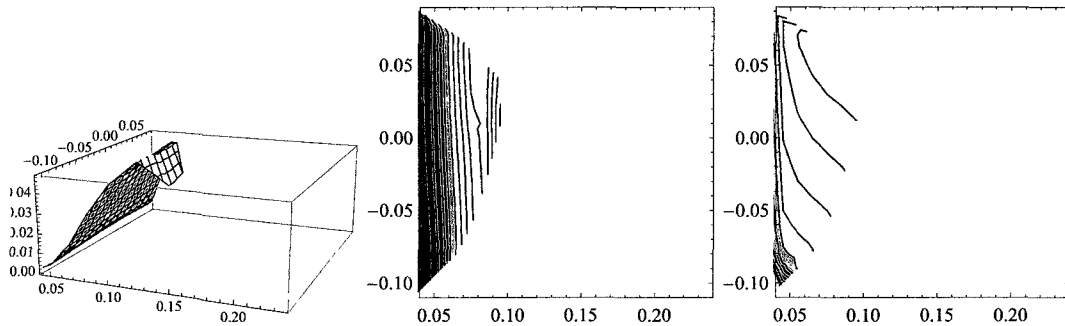


Figure 4.27: Amplitude (3D), amplitude contour, and phase contour plots for the minimum actuation rate gait, Atlantic, rectangular grid.

The resulting optimal frequency increases to 10 rad/s, while the phase lag down the wing increases to approximately 2 radians. The amplitude of the tip is at the constrained limit of 3 cm, while the amplitude of the center of the wing is up to 5 cm to compensate for the decreased tip amplitude. While the frequency and phase lag is now more consistent with the curvature rate and power cases (and biology) than the large amplitude unconstrained actuation rate case, the amplitude shape does not agree well with biology.

Chapter 5

Conclusion

5.1 Summary

We have defined a general class of mechanical rectifier systems that captures the essential dynamics of animal locomotion. An optimal gait problem was formulated to minimize a quadratic cost function while achieving a given speed of locomotion on average. The solution was shown to be purely sinusoidal, and calculated from generalized eigenvalues and eigenvectors of a pair of Hermitian matrices as frequency was varied. This is a very fast and numerically stable method capable of handling underactuated and hyper-redundant systems while ensuring achievability. Unlike most, if not all, of existing approaches, our result provides a globally optimal solution. The key is not to compromise the solution by aiming for local optimality, but to reformulate the problem for tractability, in terms of a simplified model capturing the essential rectifier dynamics. The optimal gait thus obtained can then be used as a reference signal for closed-loop control.

The case studies have shown that the quadratic optimization can produce gaits that closely resemble those seen in biology. In particular, for the link chain rectifier with a straight nominal posture, the gait minimizing the shape derivative was found to be similar to the natural motion exhibited in swimming leeches. However, analytical study of the

simple mechanical rectifier suggested that the leech swimming motion might also minimize the input power and/or torque if the damping effect for body shape change is large. For the link chain rectifier with a curved nominal posture, most optimal gaits were found to be symmetric, agreeing with our intuition based on biological observations of swimming jellyfish-like animals. The gait which minimized the torque derivative was found to be asymmetric, however, indicating that some systems may benefit from unconventional gaits that are not commonly observed in biology and counter to intuition.

We formulated the equations of motion for simple flapping-wing rectifiers, consisting of two independent discretized wings and a six degree of freedom main body (rotation and translation) to which the wings are attached. We generated models for the Atlantic, Butterfly, and Cownose rays, and examined the observed gaits, the minimally perturbed observed gaits, the basic gaits, and the optimal gaits for both fixed and free oscillation frequencies.

For the observed gait with a straight traveling wave down the wing, we initially found that the approximate model was not able to achieve the observed biological velocity. However, we then found that a minimally perturbed gait which possessed a more realistic, circular traveling wave down the wing (from head to tail), was able to achieve the observed velocity with similar amplitudes and phases as biology, which indicated the approximate model is reasonably accurate.

For the basic gait analysis we examined each system with the body fixed to translate only in the y -direction with no rotation. We found that all batoid systems generally produced more flapping gaits than biology; however, we also saw a general trend that as the aspect ratio of the wing changed from high to low, the underlying basic gait changed from oscillatory to undulatory. Additionally, we saw that the general shape of the amplitude and phase plots was similar to the perturbed gait, supporting the idea that biology is indeed taking advantage of the fundamental mechanism of rectification.

The minimum curvature rate optimal gaits and minimum power optimal gaits were

symmetric, with similar oscillation frequencies and tip amplitudes to biology, however possessing a generally more oscillatory motion. This difference is especially pronounced in the Atlantic ray, with a possible explanation being that the undulatory motion takes advantage of (or avoids) the vorticity, added mass, and suction effects involved with closely swimming against the bottom of the ocean. The fixed-frequency minimum actuation optimal gaits were symmetric with body pitching (and no rolling), and anti-symmetric with body rolling (and no pitching), which were also found to corresponded to different natural modes of the systems. The minimum curvature gait tended toward zero curvature at an infinite oscillation frequency, while the minimum actuation gait possessed an oscillation frequency many times higher than biology. The minimum curvature rate gait, on the other hand, possessed a very low oscillation frequency and a very large tip amplitude.

Of the optimal gaits, the minimum power gait was the closest match with biology for the Atlantic ray, while the minimum curvature rate gaits were the closest match with biology for the Butterfly and Cownose rays, due to tip amplitude and oscillation frequency. The phase lags of the basic gaits were closer to biology than the optimal gaits, however, and the perturbed observed gait was the closest match of all. This indicates that there is still room for improvement, and that a more sophisticated objective function or modeling process could possibly result in the perturbed observed gait being optimal. Indeed, an arbitrarily complex objective function could be chosen to force the optimal gait to perfectly match the perturbed observed gait; however, we favored fundamental objective functions in our search to ensure a solid foundation.

5.2 Future Work

There are many possible avenues for future work to build and improve upon these results. First, the mechanical model of each batoid system can be improved by the addition of more accurate muscular, skeletal, and neuronal structures. These can include such effects as

active and passive stiffnesses, three dimensional rotational dynamics for cartilage radials, and chemical costs for muscle activation or signal propagation. Second, a more detailed computational fluid dynamics model can be utilized, ideally capturing the important effects for batoid locomotion not included in this dissertation, such as the added mass effects and vortex shedding. The CFD panel method developed by Moored [98] is particularly well suited to the discretized wing model developed in this dissertation, as it approximates a surface using a small number of large panels to enable a very numerically fast estimation of the fluid forces. At additional computational cost, the globally optimal gait solution method described in this dissertation for the bilinear approximation can be used as the initial condition for one of the existing nonlinear, locally optimal solution methods. The global minimum can then be tracked while the system is slowly varied back to the fully nonlinear system. Lastly, an inverse optimal control problem can be formulated to determine an objective function that produces the observed biological gait for a given system. As mentioned earlier, Russo [80] is currently investigating a similar problem through a numerical structural perturbation method, analyzing various quantities of interest over one period of the observed gait. These methods can then be utilized a linear combination of a large set of possible basis objective functions, with coefficients numerically determined to minimize the overall error over a suitably large set of models.

Each of these improvements come with an associated increase in complexity, and therefore computation time. However, since we have noticed that all optimal gaits so far are either symmetric or anti-symmetric, the dimension of a system can be reduced by half through a symmetric or anti-symmetric constraint, resulting in two models of half complexity. These studies demonstrate that the proposed framework for computing optimal gaits can be very useful not only for robotic locomotor designs but also for increasing our understanding of animal locomotion mechanisms from a biological point of view. The models of rectifier systems can also be used as a basis for further analysis and design of locomotion control systems. Of particular interest is in the limit cycle behaviors of the rectifier systems

driven by biological feedback control systems called central pattern generators [99–103].

Chapter 6

Appendix

6.1 Preliminary lemmas

Lemma 6 *Let $h \in \mathbb{Z}_\infty$, a positive number $T \in \mathbb{R}$, a vector-valued signal $\mu \in \mathbb{P}_T^h$ and a transfer function $\Pi(s) = F(-s)^\top \Phi F(s) \in \mathbb{H}$ be given. Let ξ be the steady state response of $F(s)$ with input μ . Then the following hold:*

$$\hat{\xi} = F^h(j\omega)\hat{\mu}, \quad \hat{\xi}_k = F(j\omega k)\hat{\mu}_k, \quad \forall k \in \mathbb{Z},$$

$$\frac{2}{T} \int_0^T \mu^\top \Pi \mu dt = \sum_{k=1}^h [\hat{\mu}_k^* \Pi(j\omega k) \hat{\mu}_k] = \hat{\mu}^* \Pi^h(j\omega) \hat{\mu},$$

where $\omega := 2\pi/T$.

Proof. The result follows from straightforward calculation using basic properties of linear systems and orthogonality of harmonic basis functions. ■

Lemma 7 (S-procedure [104]) *Let real-valued quadratic functionals σ_0 and σ_1 on a complex linear space \mathbb{X} be given, where each has the form $\sigma(x) = a + \Re[b(x)] + C(x)$ with a real constant a , linear functional $b(x)$ on \mathbb{X} , and Hermitian form $C(x)$. Suppose σ_1 satisfies the regularity condition: there exist $y, z \in \mathbb{X}$ such that $\sigma_1(y) > 0$ and $\sigma_1(z) < 0$.*

Then

$$\sigma_o(x) \geq 0, \quad \forall x \in \mathbb{X} \quad \text{such that} \quad \sigma_1(x) = 0$$

holds if and only if

$$\exists \lambda \in \mathbb{R} \quad \text{such that} \quad \sigma_o(x) \geq \lambda \sigma_1(x), \quad \forall x \in \mathbb{X}.$$

6.2 Link chain rectifier model

The link chain rectifier has been introduced as a model for robotic snake [57], and the equations of motion is given by (2.3) with the following definitions:

$$\begin{aligned}
C(\theta, \dot{\theta})\dot{\theta} &:= (S_\theta H C_\theta - C_\theta H S_\theta)\dot{\theta}^2, \quad J_o := \text{diag}(J_1, \dots, J_n), \\
J(\theta) &:= J_o + S_\theta H S_\theta + C_\theta H C_\theta, \quad M := \text{diag}(m_1, \dots, m_n), \\
F &:= M^{-1}B(B^\top M^{-1}B)^{-1}A^\top L, \quad C_n := \text{diag}(c_{n_1}, \dots, c_{n_n}), \\
C_\theta &:= \text{diag}(\cos \theta_1, \dots, \cos \theta_n), \quad K_o := \text{diag}(k_1, \dots, k_{n-1}), \\
S_\theta &:= \text{diag}(\sin \theta_1, \dots, \sin \theta_n), \quad D_o := \text{diag}(d_1, \dots, d_{n-1}), \\
H &:= LA(B^\top M^{-1}B)^{-1}A^\top L, \quad \Gamma := \text{diag}(C_t, C_n, C_n L^2/3), \\
C_t &:= \text{diag}(c_{t_1}, \dots, c_{t_n}), \quad d(\theta, \dot{\theta}) = BD_o B^\top \dot{\theta}, \quad B(\theta) := B, \\
k(\theta) &= BK_o B^\top \theta, \quad L := \text{diag}(\ell_1, \dots, \ell_n), \quad m := \sum_{i=1}^n m_i, \\
\gamma(x) &:= \Gamma x,
\end{aligned}$$

$$\begin{aligned}
\Omega_\theta &:= \begin{bmatrix} C_\theta & S_\theta \\ -S_\theta & C_\theta \end{bmatrix}, \quad G_\theta := \begin{bmatrix} FS_\theta \\ -FC_\theta \end{bmatrix}, \quad e := \begin{bmatrix} 1 \\ \vdots \\ 1 \end{bmatrix}, \\
R(\theta) &:= \begin{bmatrix} \Omega_\theta G_\theta \\ I \end{bmatrix}, \quad N(\theta) := \begin{bmatrix} \Omega_\theta E \\ 0 \end{bmatrix}, \quad E := \begin{bmatrix} e & 0 \\ 0 & e \end{bmatrix}, \\
A &:= \begin{bmatrix} 1 & 1 & & \\ & \ddots & \ddots & \\ & & & 1 & 1 \end{bmatrix}^\top, \quad B := \begin{bmatrix} 1 & -1 & & \\ & \ddots & \ddots & \\ & & & 1 & -1 \end{bmatrix}^\top,
\end{aligned}$$

where $A, B \in \mathbb{R}^{n \times (n-1)}$, $e \in \mathbb{R}^n$, and $\dot{\theta}^2$ is the vector whose i^{th} entry is $\dot{\theta}_i^2$. Given a nominal posture η , the bilinear rectifier model that approximates the original system is given by (2.6)

with

$$\begin{aligned}
Q(\vartheta) &:= N_\eta^\top \Gamma N_\eta + \Xi \Theta + (\Xi \Theta)^\top + \Theta^\top \Psi \Theta, \quad K := BK_o B^\top, \\
A(\vartheta) &:= R_\eta^\top \Gamma N_\eta + \begin{bmatrix} \Lambda_1 \vartheta & \Lambda_2 \vartheta \end{bmatrix}, \quad \begin{bmatrix} \lambda_1 & \lambda_2 \end{bmatrix} := \dot{R}_1^\top \Gamma N_\eta, \\
D &:= BD_o B^\top + R_\eta^\top \Gamma R_\eta, \quad \Psi := \dot{U}_\eta^\top \Gamma \dot{U}_\eta + \Delta + \Delta^\top, \\
J &:= J(\eta), \quad \Xi := N_\eta^\top \Gamma \dot{U}_\eta, \quad \Theta := \text{diag}(\vartheta, \vartheta), \\
\begin{bmatrix} \Lambda_1 & \Lambda_2 \end{bmatrix} &:= \begin{bmatrix} \text{diag}(\lambda_1) & \text{diag}(\lambda_2) \end{bmatrix} + R_\eta^\top \Gamma \dot{U}_\eta + \dot{R}_2^\top \Gamma \mathcal{U}_\eta, \\
\Delta &:= \begin{bmatrix} \text{diag}(\delta_1) & \text{diag}(\delta_2) \\ \text{diag}(\delta_3) & \text{diag}(\delta_4) \end{bmatrix}, \quad \begin{bmatrix} \delta_1 & \delta_2 \\ \delta_3 & \delta_4 \end{bmatrix} := -N_\eta^\top \Gamma \mathcal{U}_\eta / 2, \\
\dot{R}_1 &:= \begin{bmatrix} \Omega_\eta \dot{G}_\eta \\ 0 \end{bmatrix}, \quad \dot{R}_2 := \begin{bmatrix} \dot{\Omega}_\eta G_\eta \\ 0 \end{bmatrix}, \quad \dot{G}_\eta := \begin{bmatrix} FC_\eta \\ FS_\eta \end{bmatrix}, \\
\dot{\Omega}_\eta &:= \begin{bmatrix} -S_\eta & C_\eta \\ -C_\eta & -S_\eta \end{bmatrix}, \quad \mathcal{U}_\eta := \begin{bmatrix} \Omega_\eta \\ 0 \end{bmatrix}, \quad \dot{\mathcal{U}}_\eta := \begin{bmatrix} \dot{\Omega}_\eta \\ 0 \end{bmatrix},
\end{aligned}$$

where the subscript η is used to indicate that a function is evaluated at $\theta = \eta$, e.g. $N_\eta := N(\eta)$. If the nominal posture is chosen to be straight ($\eta = 0$), then these parameter definitions simplify to

$$\begin{aligned}
J &:= J_o + F^\top M F, \quad D := LC_n L / 3 + F^\top C_n F + BD_o B^\top, \\
\Lambda &:= F^\top C_o + \text{diag}(F^\top C_t e), \quad A(\vartheta) := \begin{bmatrix} \Lambda \vartheta & -F^\top C_n e \end{bmatrix}, \\
Q(\vartheta) &:= \begin{bmatrix} e^\top C_t e + \vartheta^\top C_o \vartheta & -\vartheta^\top C_o e \\ -e^\top C_o \vartheta & e^\top C_n e - \vartheta^\top C_o \vartheta \end{bmatrix}, \quad C_o := C_n - C_t.
\end{aligned}$$

Additionally, if $c_{n_i} := c_n$ and $c_{t_i} := c_t$ for all i , the equations are further reduced by noting that $F^\top e = 0$. The following parameter values are from a typical medicinal leech, and are

used for the model in the numerical study reported here unless otherwise noted:

$$n = 18, \quad m = 0.0011 \text{ kg}, \quad \ell = 0.1073 \text{ m}, \quad m_i = m/n,$$

$$c_{n_i} = 0.8\ell_i \text{ N} \cdot \text{s/m}, \quad c_{t_i} = 0.1\ell_i \text{ N} \cdot \text{s/m},$$

$$\ell_i = \ell/(2n), \quad J_i := m_i\ell_i^2/3, \quad d_i = 0, \quad k_i = 0.$$

6.3 Batoid thickness data

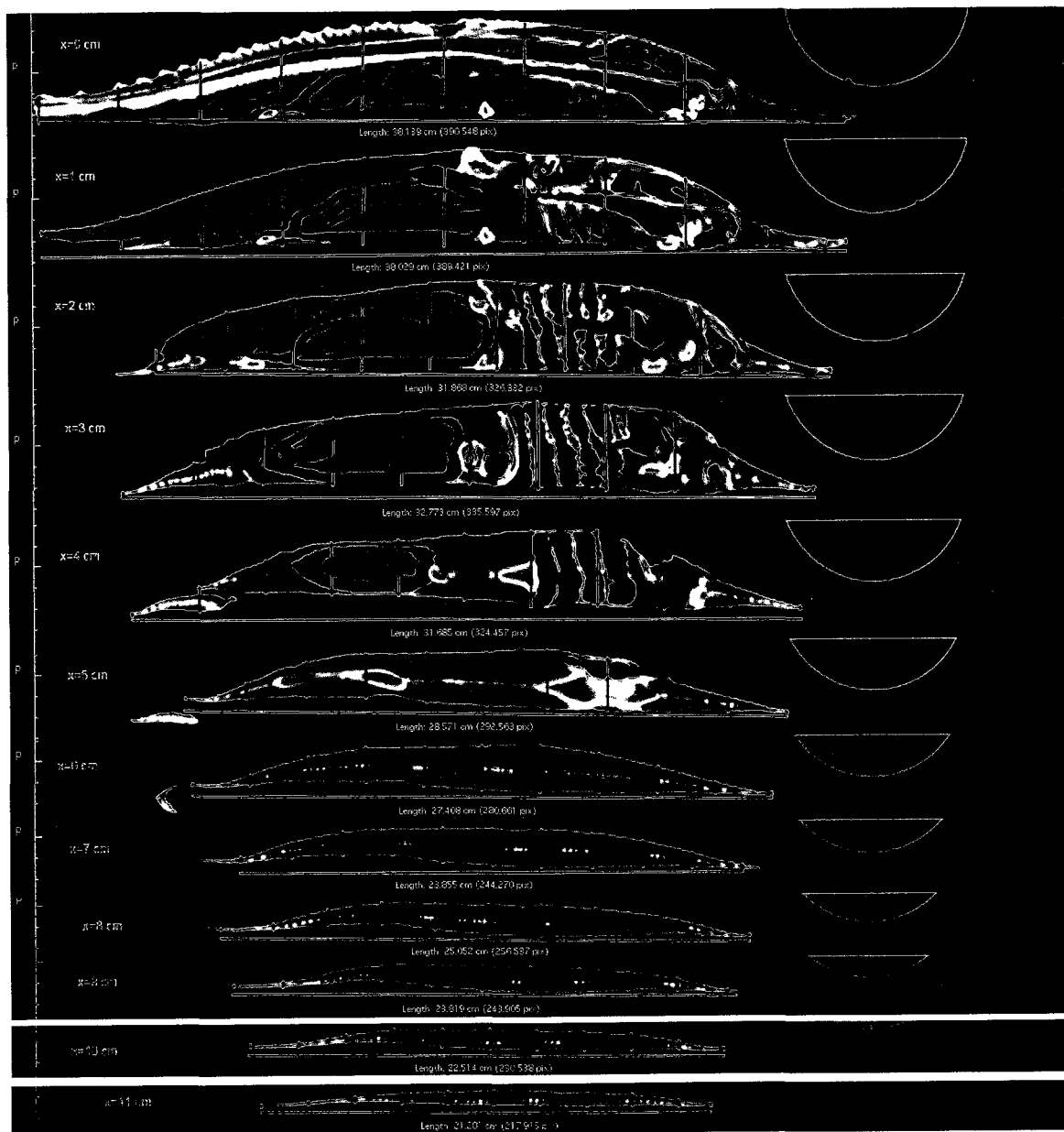


Figure 6.1: Atlantic cross sections for thickness measurements.

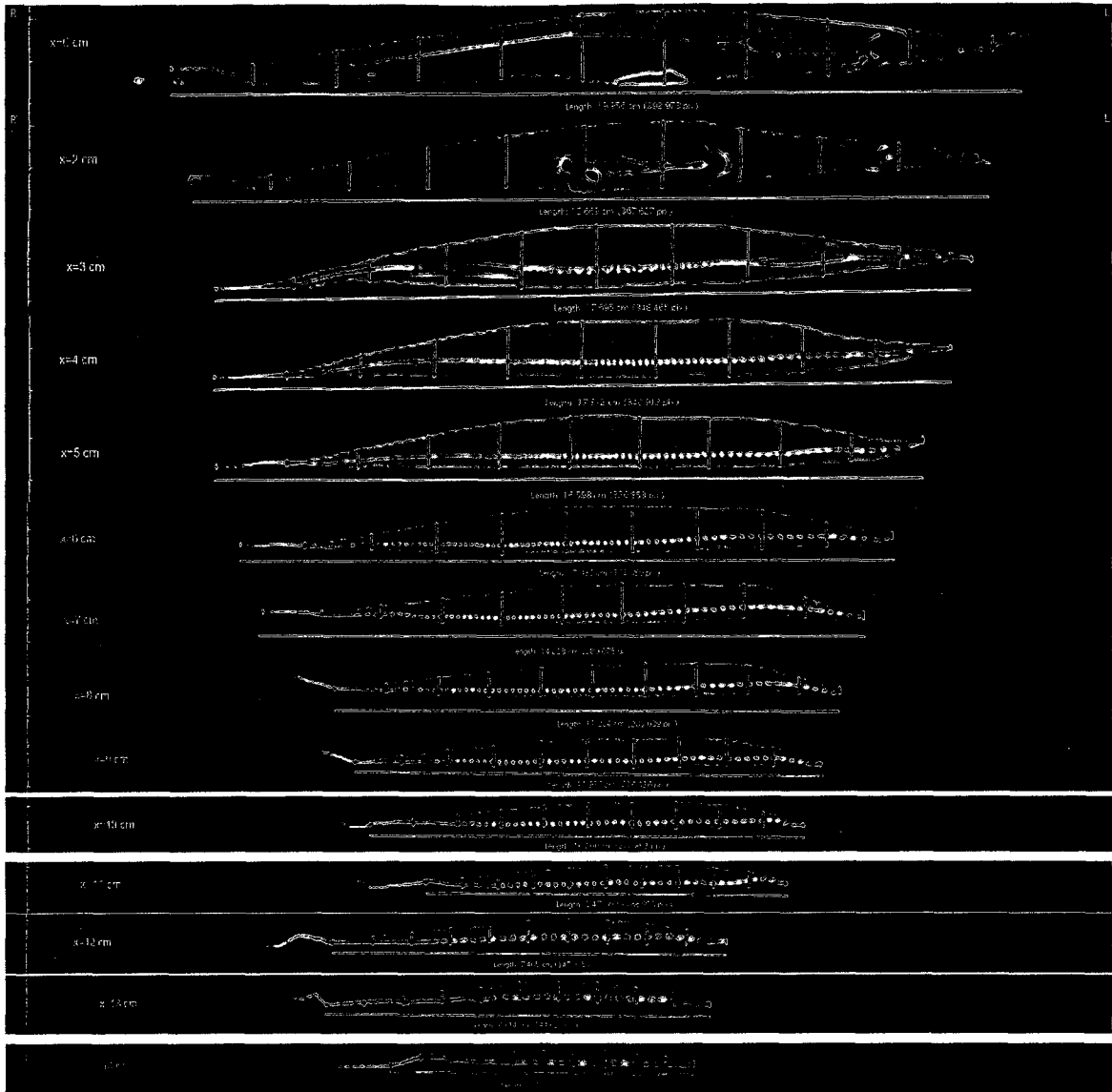


Figure 6.2: Butterfly cross sections for thickness measurements.

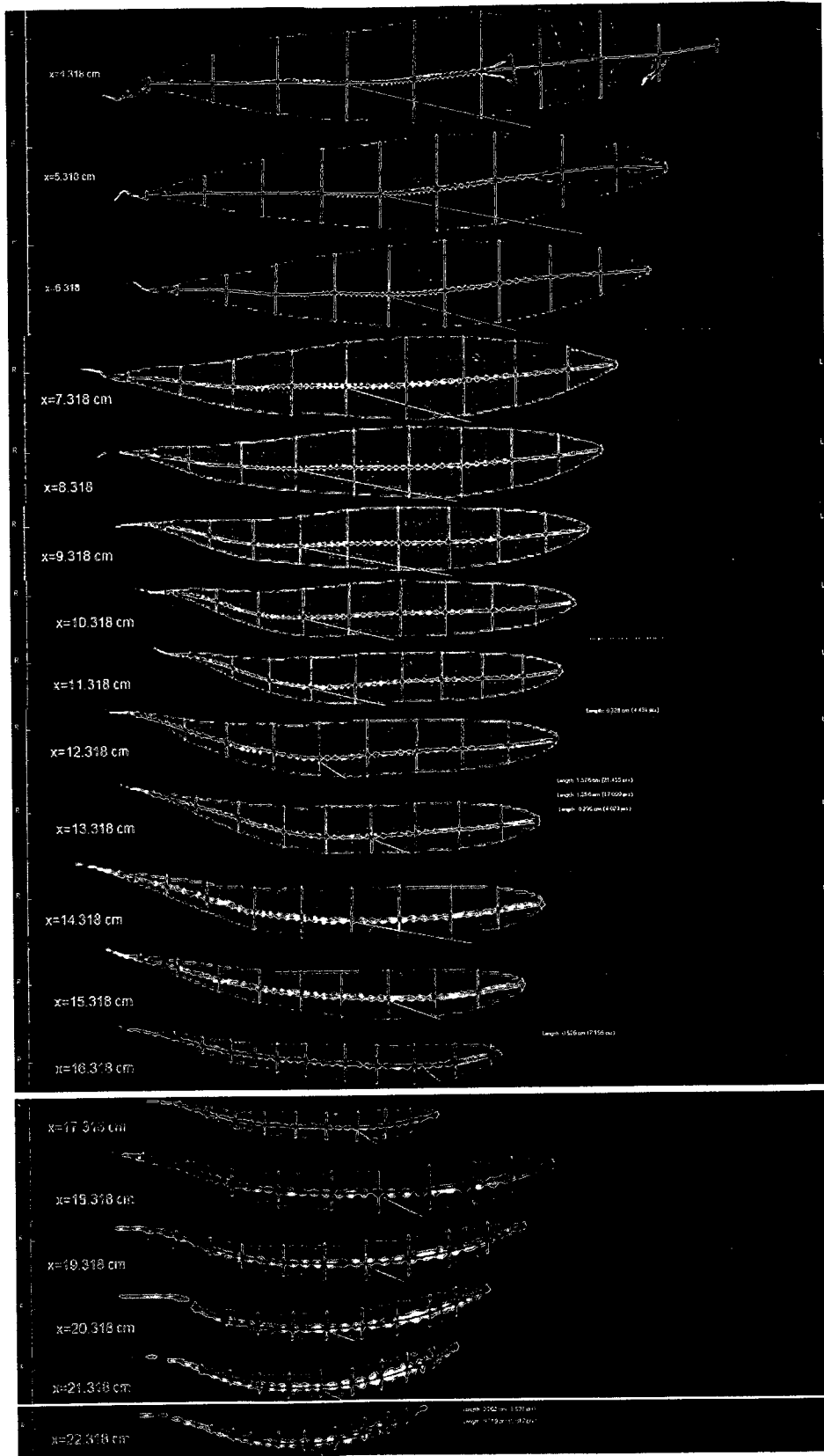


Figure 6.3: Cownose cross sections for thickness measurements.

x, cm:	0	1	2	3	4	5	6	7	8	9	10	11
head:	0.22	0.18	0.26	0.22	0.18	0.15	0.15	0.29	0.15	0.18	0.15	0.15
.	0.83	0.94	0.94	1.27	1.02	0.69	0.58	0.76	0.44	0.62	0.40	0.33
.	3.30	3.48	3.44	3.81	2.28	1.63	1.27	1.27	0.87	0.87	0.80	0.58
.	4.03	4.17	4.17	4.13	3.66	2.57	1.92	1.67	1.34	1.12	0.91	0.65
.	4.35	4.28	4.17	4.24	3.66	2.83	2.28	1.85	1.52	1.23	0.94	0.65
.	3.95	4.53	4.28	3.74	3.19	2.61	2.18	1.78	1.49	1.20	0.98	0.73
.	3.95	4.13	4.13	3.48	2.68	2.39	1.89	1.67	1.27	0.98	0.87	0.62
.	3.84	3.63	3.74	3.26	2.54	2.14	1.74	1.27	1.05	0.73	0.65	0.51
.	2.94	2.65	3.37	2.68	1.60	1.70	1.16	1.16	0.76	0.47	0.40	0.29
.	1.52	1.49	2.79	1.09	1.23	0.76	0.58	0.76	0.33	0.29	0.25	0.18
tail:	1.33	0.22	0.98	0.15	0.18	0.11	0.15	0.29	0.11	0.11	0.18	0.15

Table 6.1: Atlantic thickness measurements, cm

x, cm:	0	1	2	3	4	5	6	7	8	9	10	11
head:	18.1	18.0	14.9	15.4	14.8	13.3	12.7	10.9	11.5	10.9	10.3	9.6
.	14.3	14.2	11.7	12.1	11.7	10.4	10.0	8.5	9.0	8.5	8.0	7.5
.	10.4	10.4	8.6	8.8	8.5	7.6	7.2	6.2	6.5	6.1	5.8	5.4
.	6.6	6.6	5.4	5.6	5.3	4.7	4.5	3.8	4.0	3.8	3.5	3.3
.	2.8	2.8	2.2	2.3	2.2	1.9	1.7	1.4	1.5	1.4	1.3	1.1
.	-1.0	-1.0	-1.0	-1.0	-1.0	-1.0	-1.0	-1.0	-1.0	-1.0	-1.0	-1.0
.	-4.8	-4.8	-4.2	-4.3	-4.2	-3.9	-3.7	-3.4	-3.5	-3.4	-3.3	-3.1
.	-8.6	-8.6	-7.4	-7.6	-7.3	-6.7	-6.5	-5.8	-6.0	-5.8	-5.5	-5.3
.	-12.4	-12.4	-10.6	-10.8	-10.5	-9.6	-9.2	-8.2	-8.5	-8.1	-7.8	-7.4
.	-16.3	-16.2	-13.7	-14.1	-13.7	-12.4	-12.0	-10.5	-11.0	-10.5	-10.0	-9.5
tail:	-20.1	-20.0	-16.9	-17.4	-16.8	-15.3	-14.7	-12.9	-13.5	-12.9	-12.3	-11.6

Table 6.2: y-positions of Atlantic thickness measurements, mm

x, cm:	3	4	5	6	7	8	9	10	11	12	13	14
head:	0.12	0.09	0.16	0.16	0.19	0.17	0.10	0.10	0.09	0.08	0.11	0.11
.	0.51	0.57	0.64	0.58	0.46	0.38	0.44	0.36	0.36	0.31	0.25	0.21
.	0.92	1.10	1.06	0.93	0.79	0.68	0.61	0.55	0.47	0.39	0.31	0.25
.	1.25	1.36	1.22	0.97	0.91	0.77	0.69	0.63	0.49	0.44	0.39	0.31
.	1.43	1.34	1.22	1.10	0.94	0.79	0.68	0.58	0.49	0.43	0.35	0.29
.	1.50	1.34	1.24	1.07	0.88	0.74	0.65	0.58	0.52	0.41	0.34	0.26
.	1.36	1.22	1.06	0.99	0.77	0.66	0.61	0.50	0.46	0.30	0.27	0.26
.	0.99	0.89	0.78	0.71	0.58	0.57	0.47	0.41	0.41	0.31	0.24	0.18
.	0.51	0.54	0.47	0.38	0.30	0.41	0.36	0.25	0.31	0.24	0.17	0.14
.	0.26	0.17	0.16	0.14	0.13	0.22	0.20	0.16	0.22	0.16	0.11	0.11
tail:	0.05	0.07	0.09	0.06	0.08	0.08	0.10	0.08	0.11	0.10	0.06	0.07

Table 6.3: Butterfly thickness measurements, cm

x, cm:	3	4	5	6	7	8	9	10	11	12	13	14
head:	7.8	7.7	7.0	6.2	5.6	4.4	4.0	3.6	2.7	2.5	2.4	1.9
.	6.1	5.9	5.4	4.6	4.2	3.2	2.9	2.6	1.9	1.7	1.7	1.3
.	4.3	4.2	3.7	3.1	2.8	2.1	1.8	1.6	1.0	1.0	0.9	0.7
.	2.5	2.5	2.1	1.6	1.3	0.9	0.7	0.5	0.2	0.2	0.2	0.1
.	0.8	0.7	0.4	0.0	-0.1	-0.3	-0.4	-0.5	-0.7	-0.5	-0.5	-0.4
.	-1.0	-1.0	-1.3	-1.5	-1.5	-1.5	-1.5	-1.5	-1.5	-1.3	-1.3	-1.0
.	-2.8	-2.7	-2.9	-3.0	-2.9	-2.7	-2.6	-2.5	-2.3	-2.0	-2.0	-1.6
.	-4.5	-4.5	-4.6	-4.6	-4.3	-3.9	-3.7	-3.5	-3.2	-2.7	-2.7	-2.1
.	-6.3	-6.2	-6.2	-6.1	-5.8	-5.1	-4.8	-4.6	-4.0	-3.5	-3.4	-2.7
.	-8.1	-7.9	-7.9	-7.6	-7.2	-6.2	-5.9	-5.6	-4.9	-4.2	-4.2	-3.3
tail:	-9.8	-9.7	-9.5	-9.2	-8.6	-7.4	-7.0	-6.6	-5.7	-5.0	-4.9	-3.9

Table 6.4: y-positions of Butterfly thickness measurements, mm

x, cm:	4.3	5.3	6.3	7.3	8.3	9.3	11.3	13.3	15.3	17.3	20.3	22.3
head:	0.57	0.43	0.31	0.31	0.33	0.29	0.40	0.30	0.32	0.18	0.14	0.12
.	2.51	2.11	2.07	1.77	1.61	1.55	1.42	1.26	1.09	0.73	0.55	0.26
.	3.84	3.24	2.97	2.67	2.40	2.21	1.80	1.58	1.29	0.92	0.61	0.39
.	4.46	4.08	3.66	3.24	2.80	2.47	1.92	1.69	1.37	0.94	0.64	0.43
.	4.79	4.33	3.89	3.36	2.92	2.61	2.00	1.96	1.29	0.83	0.60	0.42
.	4.57	3.87	3.61	3.02	2.71	2.36	2.02	1.67	1.07	0.82	0.54	0.37
.	4.00	3.35	3.03	2.65	2.15	1.96	1.78	1.42	0.92	0.61	0.52	0.31
.	3.46	2.57	2.25	1.94	1.65	1.63	1.34	1.06	0.72	0.56	0.40	0.23
.	2.08	1.30	1.34	1.17	1.07	1.11	0.86	0.50	0.48	0.37	0.30	0.22
tail:	0.54	0.35	0.40	0.37	0.29	0.33	0.23	0.17	0.19	0.18	0.18	0.16

Table 6.5: Cownose thickness measurements, cm

x, cm:	4.3	5.3	6.3	7.3	8.3	9.3	11.3	13.3	15.3	17.3	20.3	22.3
head:	10.8	9.7	8.6	7.9	7.4	6.6	5.6	4.7	3.3	2.2	0.8	0.0
.	7.9	7.1	6.2	5.7	5.3	4.7	3.9	3.2	2.2	1.3	0.2	-0.4
.	5.1	4.5	3.9	3.5	3.2	2.8	2.2	1.7	1.0	0.3	-0.4	-0.9
.	2.3	1.9	1.5	1.3	1.1	0.9	0.5	0.2	-0.2	-0.6	-1.1	-1.3
.	-0.6	-0.7	-0.8	-0.9	-1.0	-1.0	-1.2	-1.3	-1.4	-1.5	-1.7	-1.8
.	-3.4	-3.3	-3.2	-3.1	-3.0	-3.0	-2.8	-2.7	-2.6	-2.5	-2.3	-2.2
.	-6.3	-5.9	-5.5	-5.3	-5.1	-4.9	-4.5	-4.2	-3.8	-3.4	-2.9	-2.7
.	-9.1	-8.5	-7.9	-7.5	-7.2	-6.8	-6.2	-5.7	-5.0	-4.3	-3.6	-3.1
.	-11.9	-11.1	-10.2	-9.7	-9.3	-8.7	-7.9	-7.2	-6.2	-5.3	-4.2	-3.6
tail:	-14.8	-13.7	-12.6	-11.9	-11.4	-10.6	-9.6	-8.7	-7.3	-6.2	-4.8	-4.0

Table 6.6: y-positions of Cownose thickness measurements, mm

6.4 Natural modes

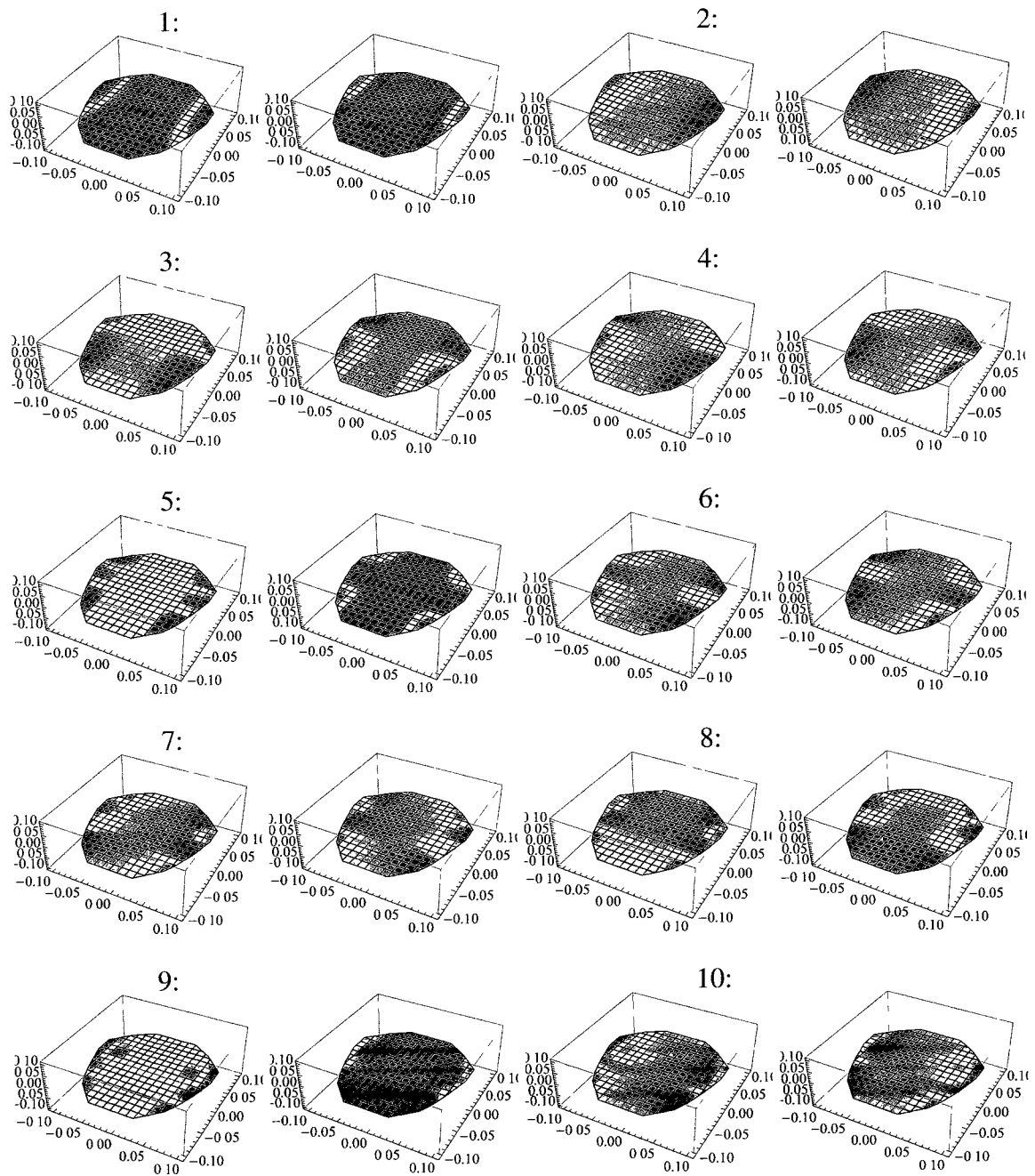


Figure 6.4: First 10 natural modes for Atlantic rectangular grid, two snapshots each.

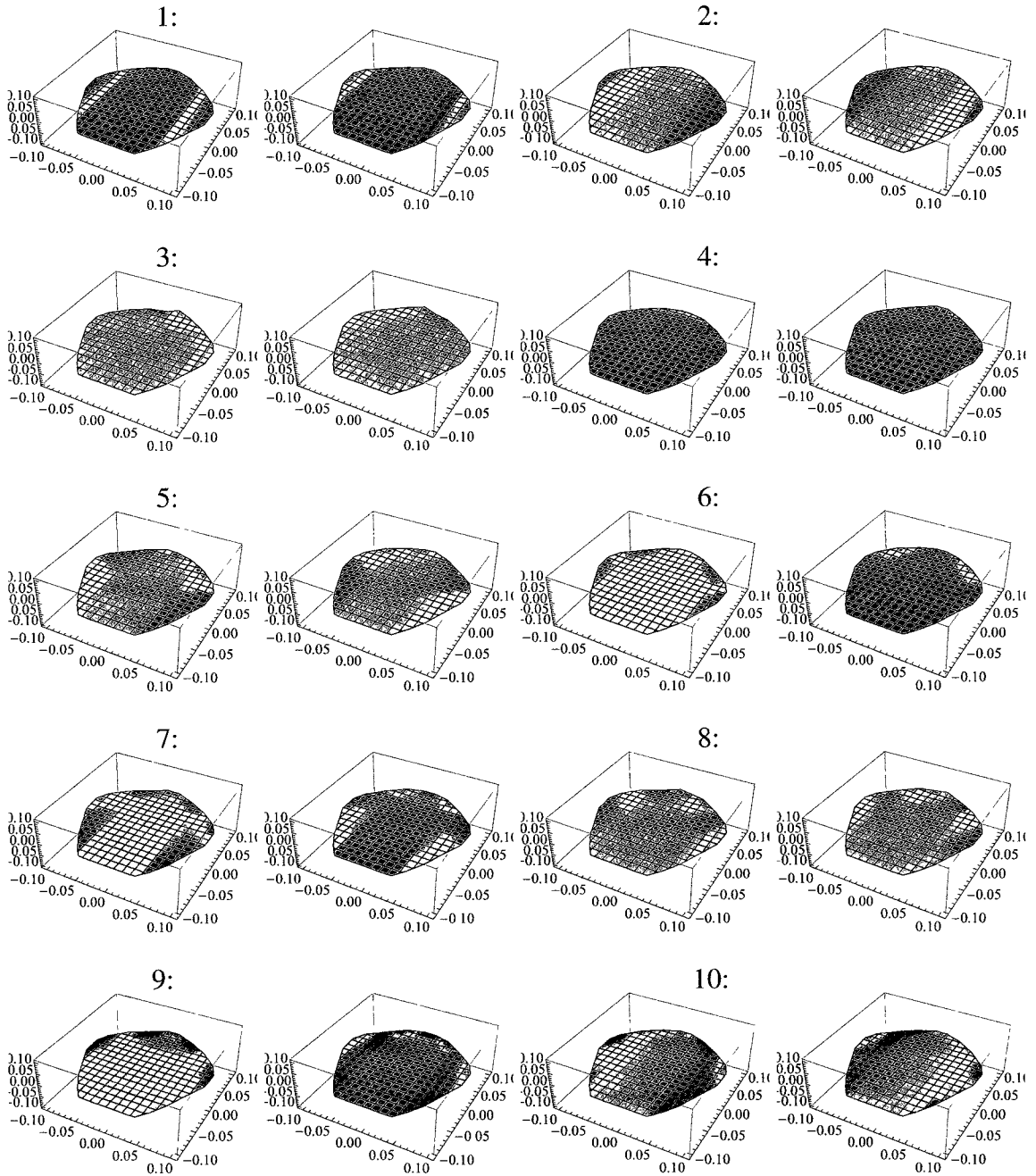


Figure 6.5: First 10 natural modes for Atlantic radial grid, two snapshots each.

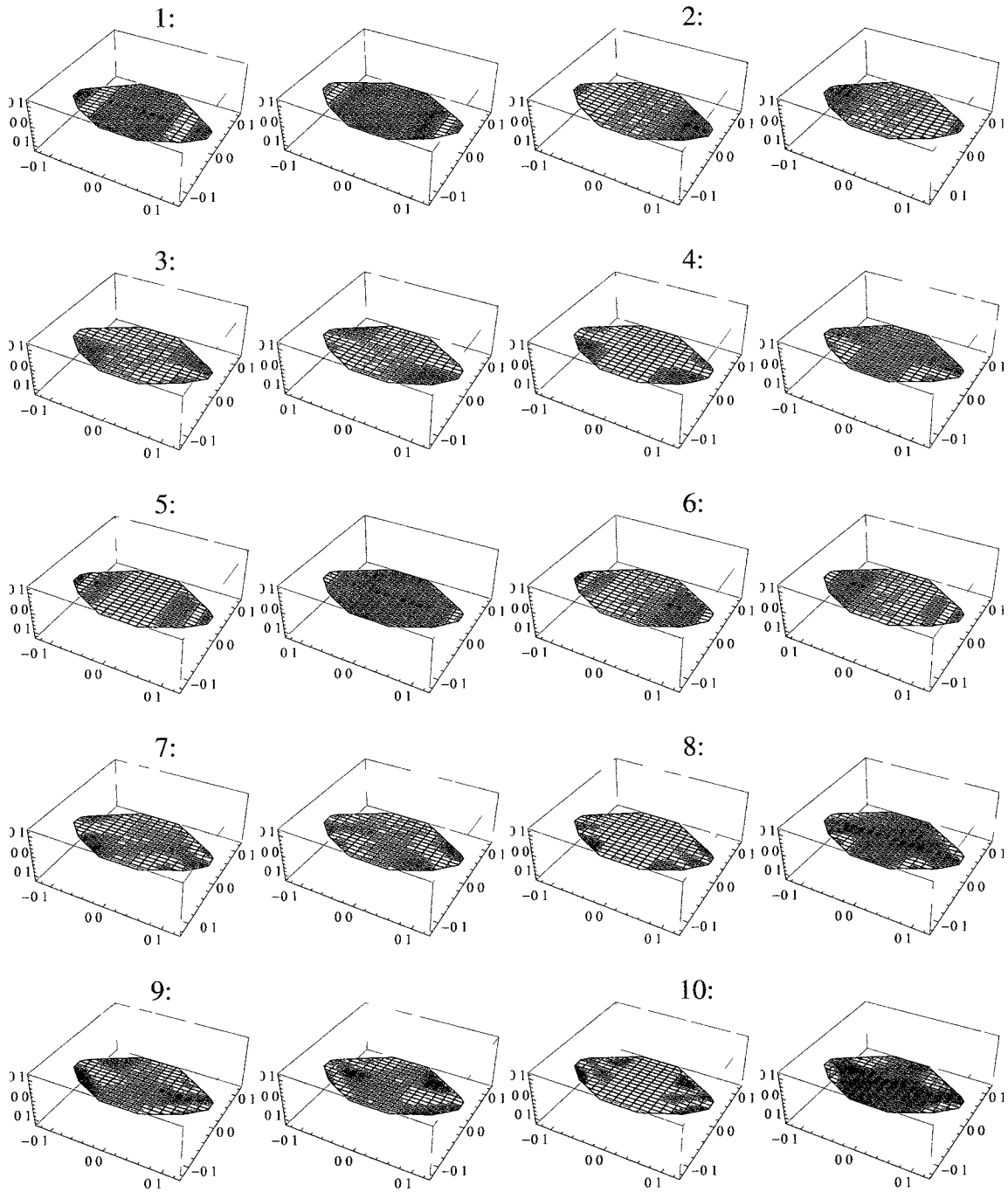


Figure 6.6: First 10 natural modes for Butterfly rectangular grid, two snapshots each.

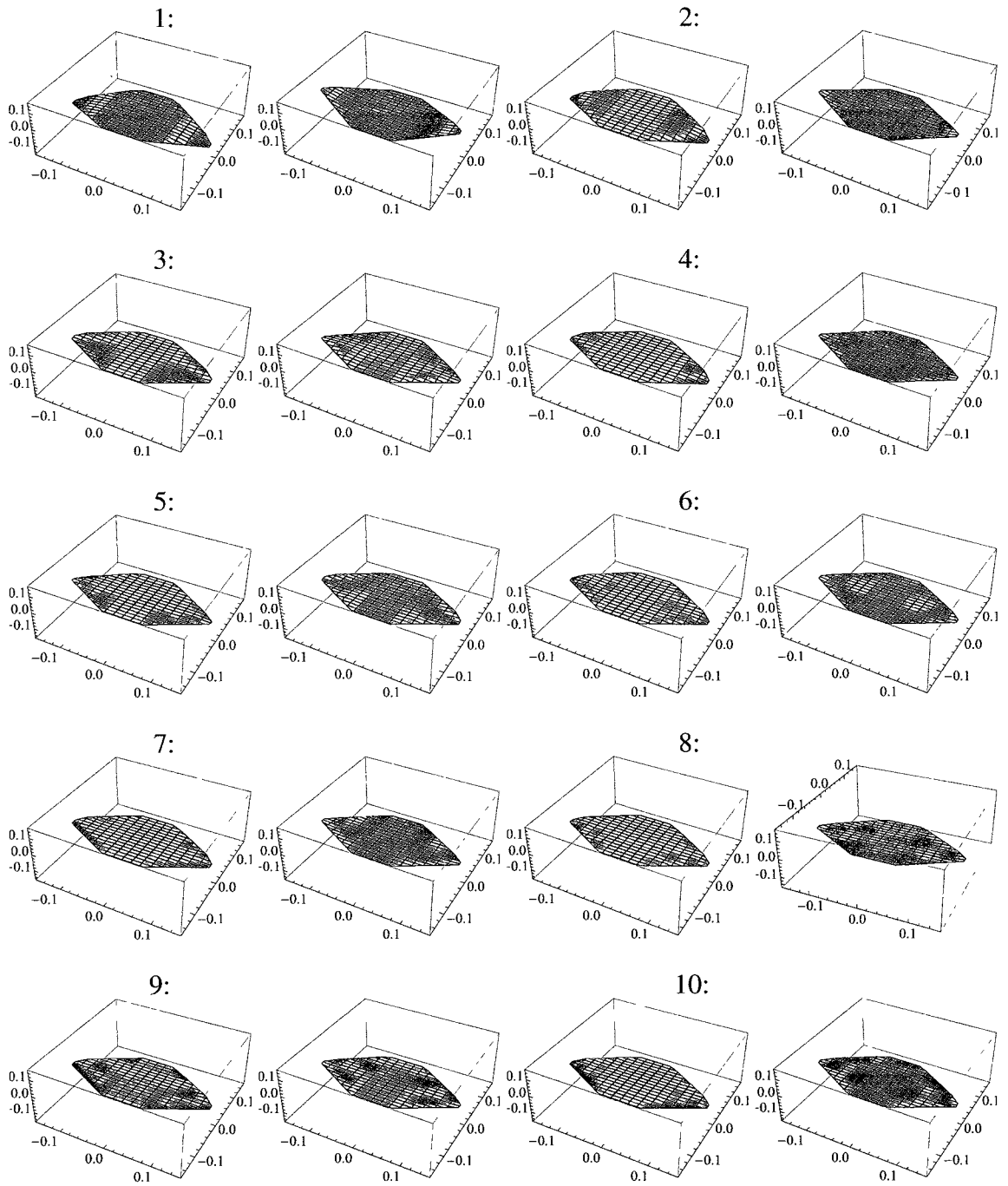


Figure 6.7: First 10 natural modes for Cownose symmetric rectangular grid (symmetric constraint), two snapshots each.

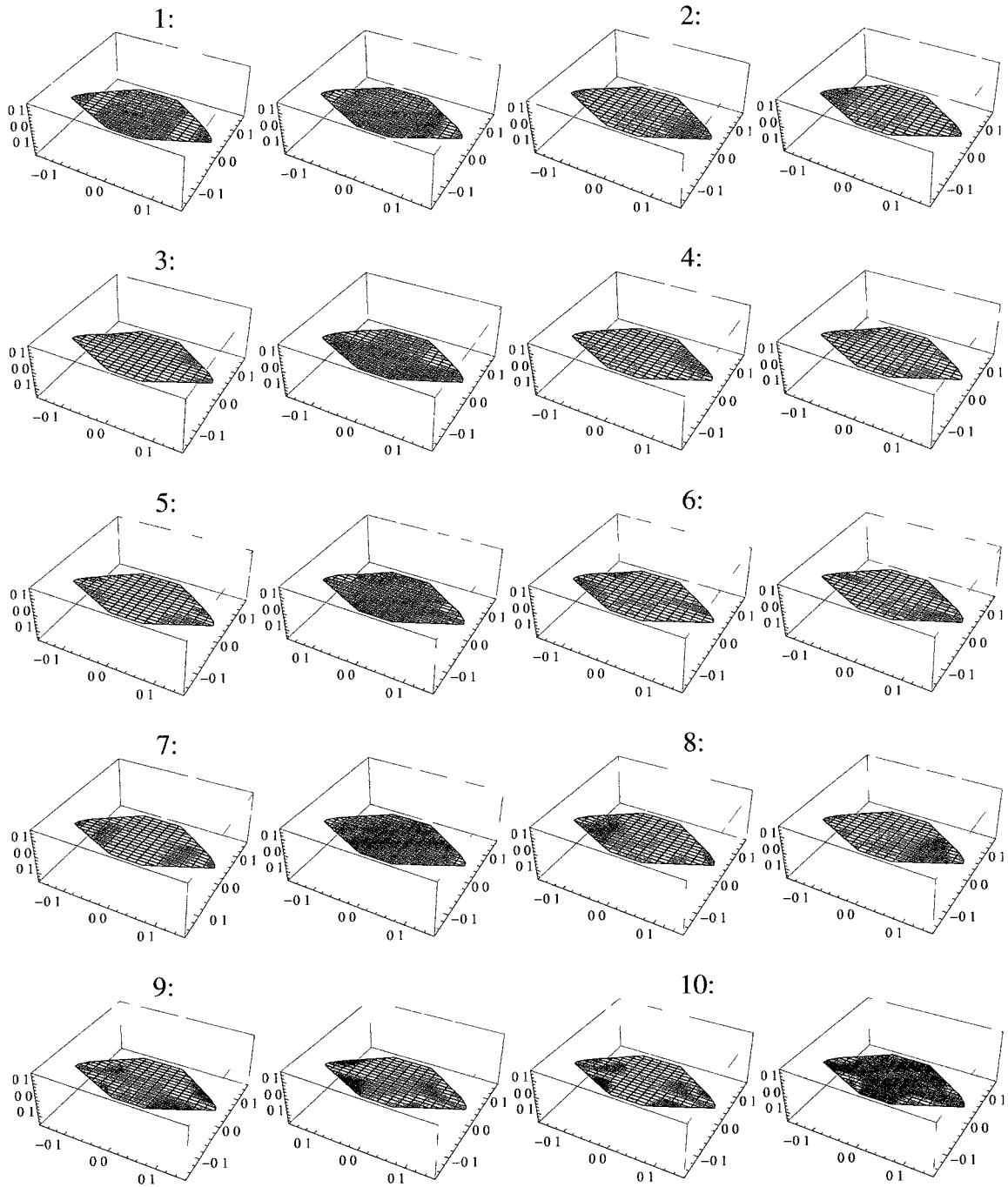


Figure 6.8: First 10 natural modes for Cownose radial grid, two snapshots each.

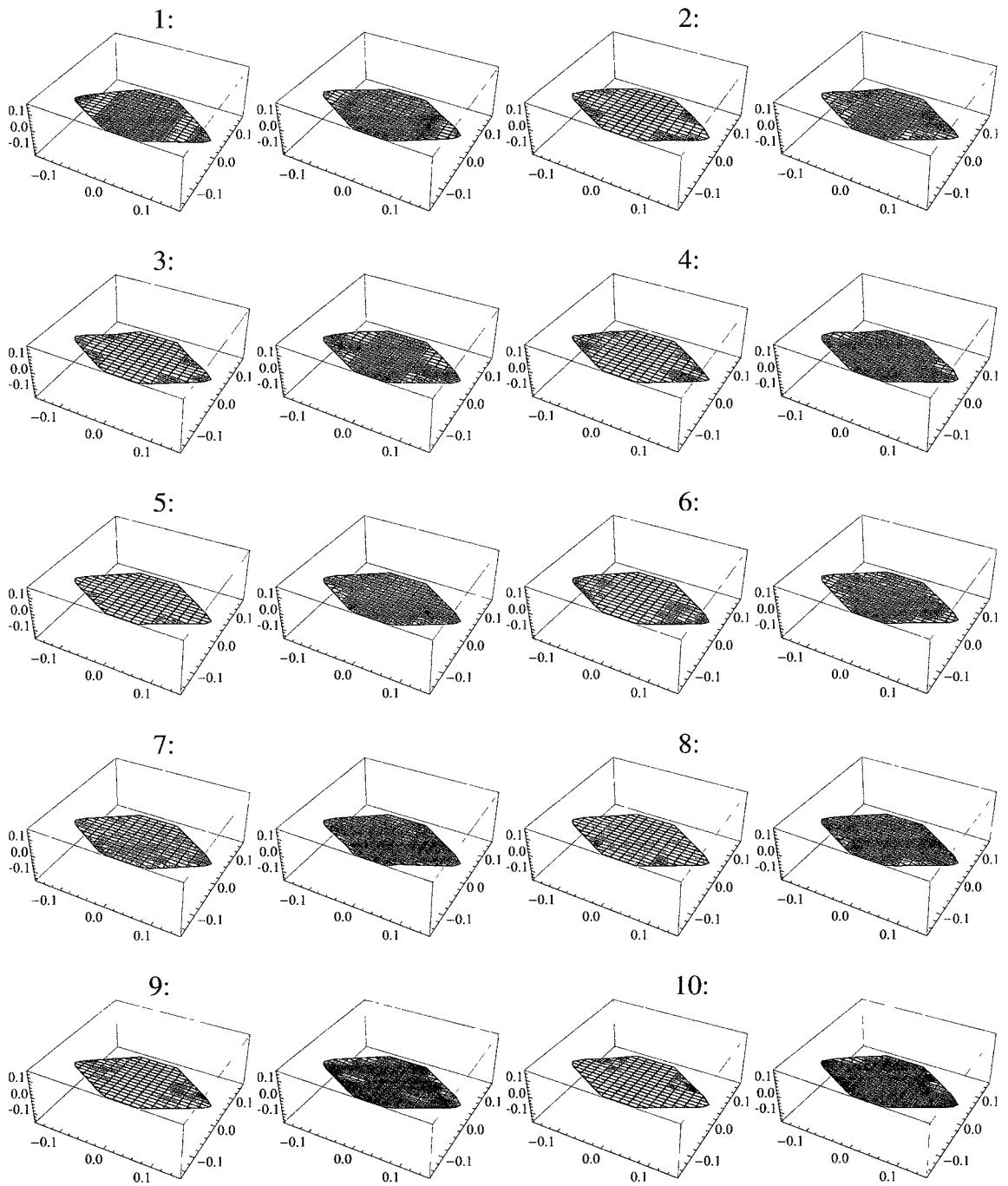


Figure 6.9: First 10 natural modes for Cownose shifted radial grid (symmetric constraint), two snapshots each.

Mode #	Atlantic		Butterfly	Cownose		
	Rect.	Radial	Rect.	Rect.	Radial	Radial Shifted
1	24.25	22.90	13.30	7.82	29.19	21.47
2	30.29	28.75	19.29	21.65	38.13	34.41
3	42.07	57.59	37.22	26.14	53.28	37.72
4	42.28	58.65	38.38	45.71	54.63	57.97
5	64.10	68.06	48.45	53.49	86.82	65.08
6	65.80	69.21	56.61	57.99	89.48	65.99
7	84.38	76.99	84.55	75.66	94.41	69.51
8	84.72	77.57	84.95	87.28	100.93	87.27
9	99.44	78.24	89.55	98.57	125.78	94.77
10	104.57	84.51	90.07	99.71	128.11	99.15

Table 6.7: Undamped natural frequencies.

6.5 Basic gaits

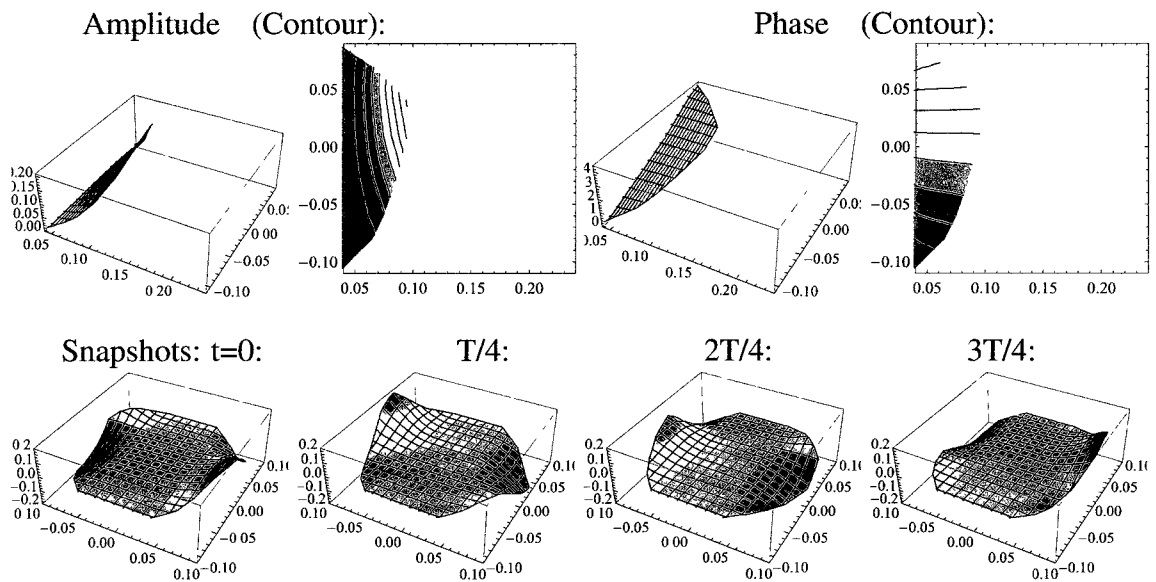


Figure 6.10: Basic gait for Atlantic rectangular grid.

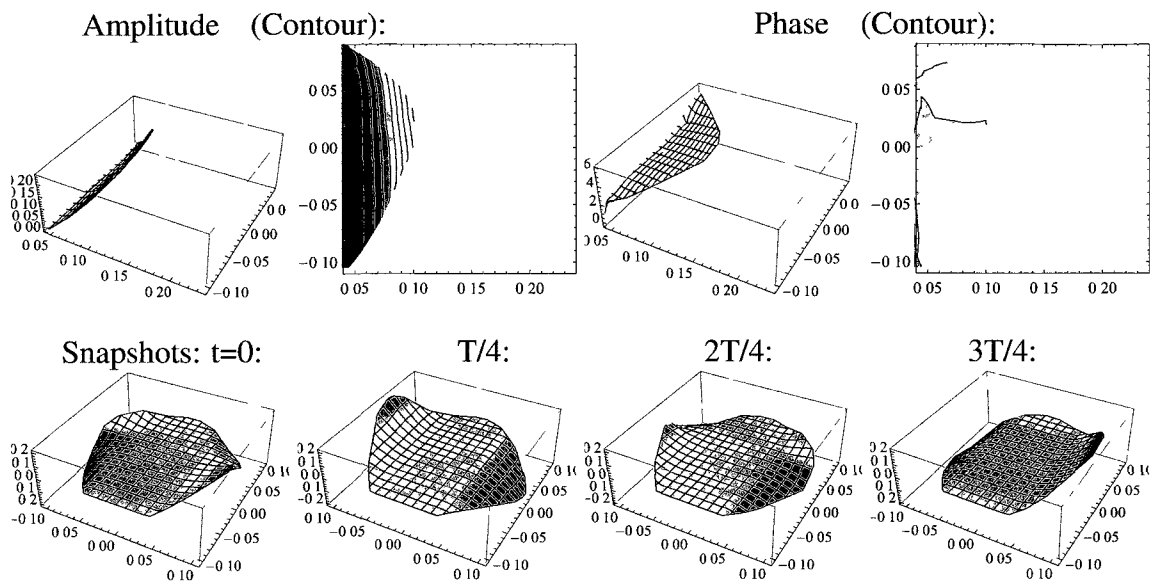


Figure 6.11: Basic gait for Atlantic radial grid.

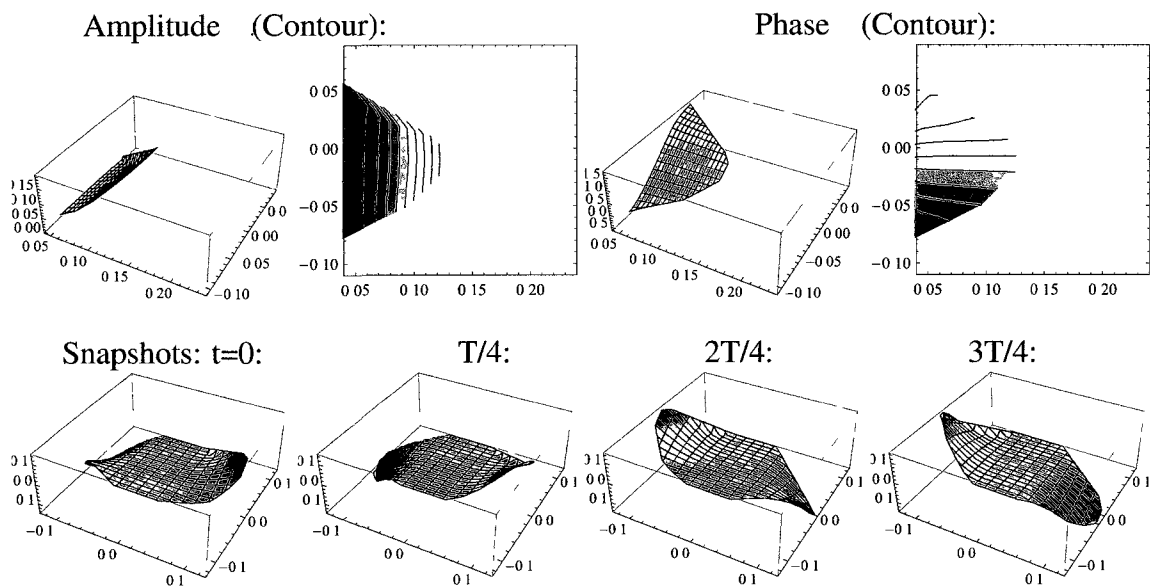


Figure 6.12: Basic gait for Butterfly rectangular grid.

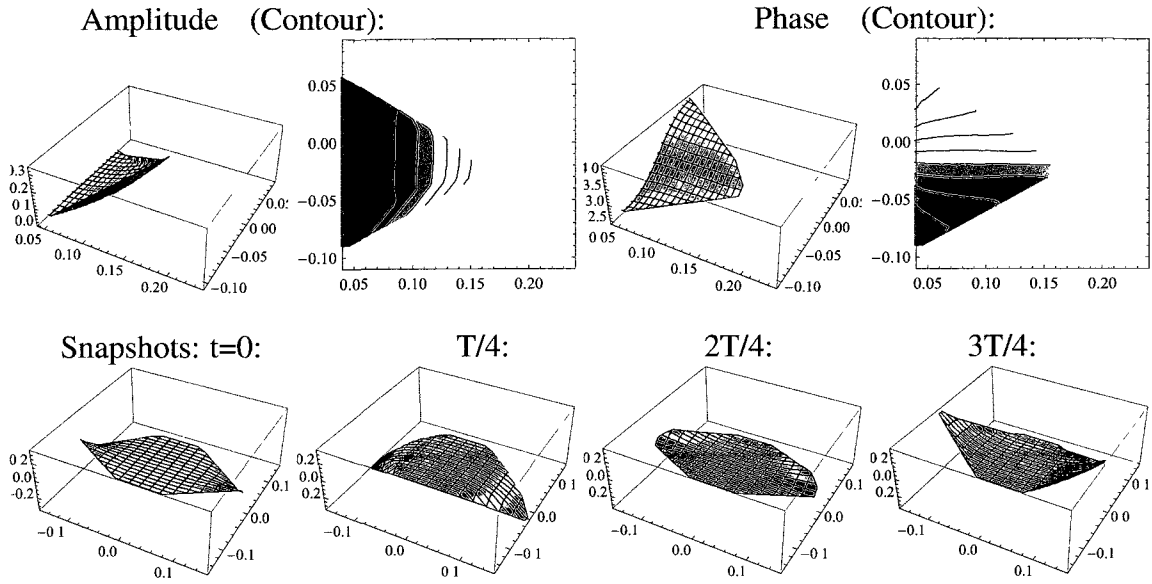


Figure 6.13: Basic gait for Cownose rectangular grid (symmetric constraint).

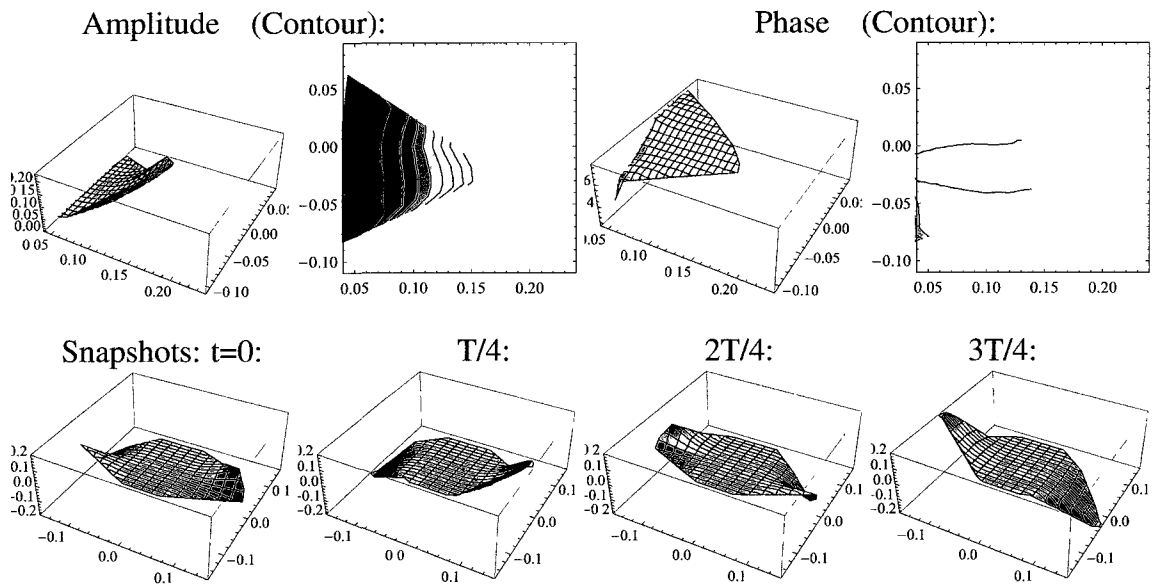


Figure 6.14: Basic gait for Cownose radial grid.

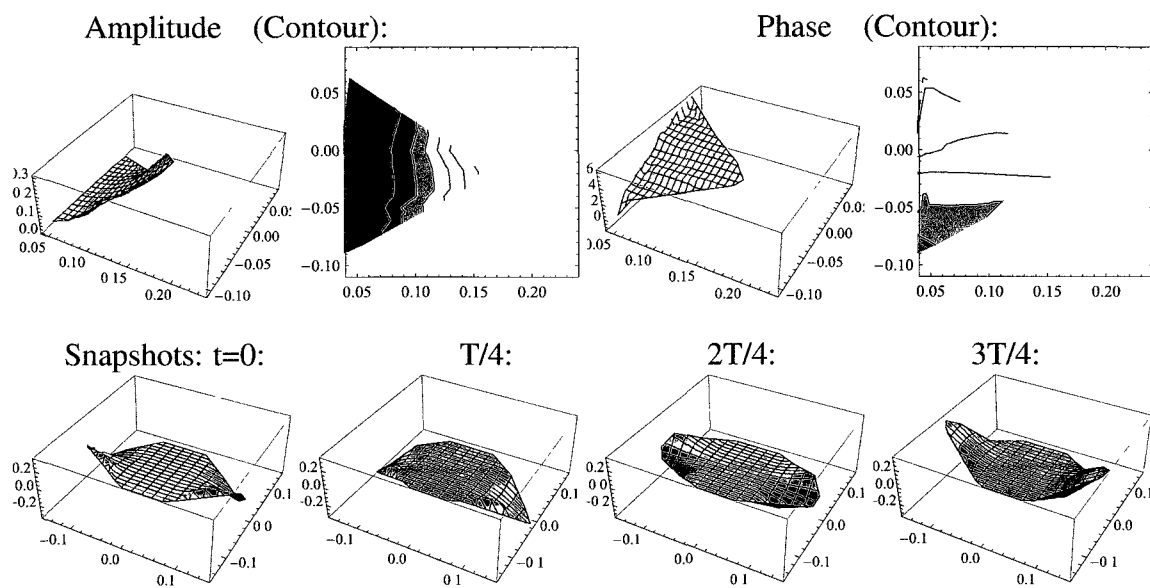


Figure 6.15: Basic gait for Cownose radial shifted grid (symmetric constraint).

6.6 Optimal gaits

6.6.1 Minimum objective values vs. frequency, ω

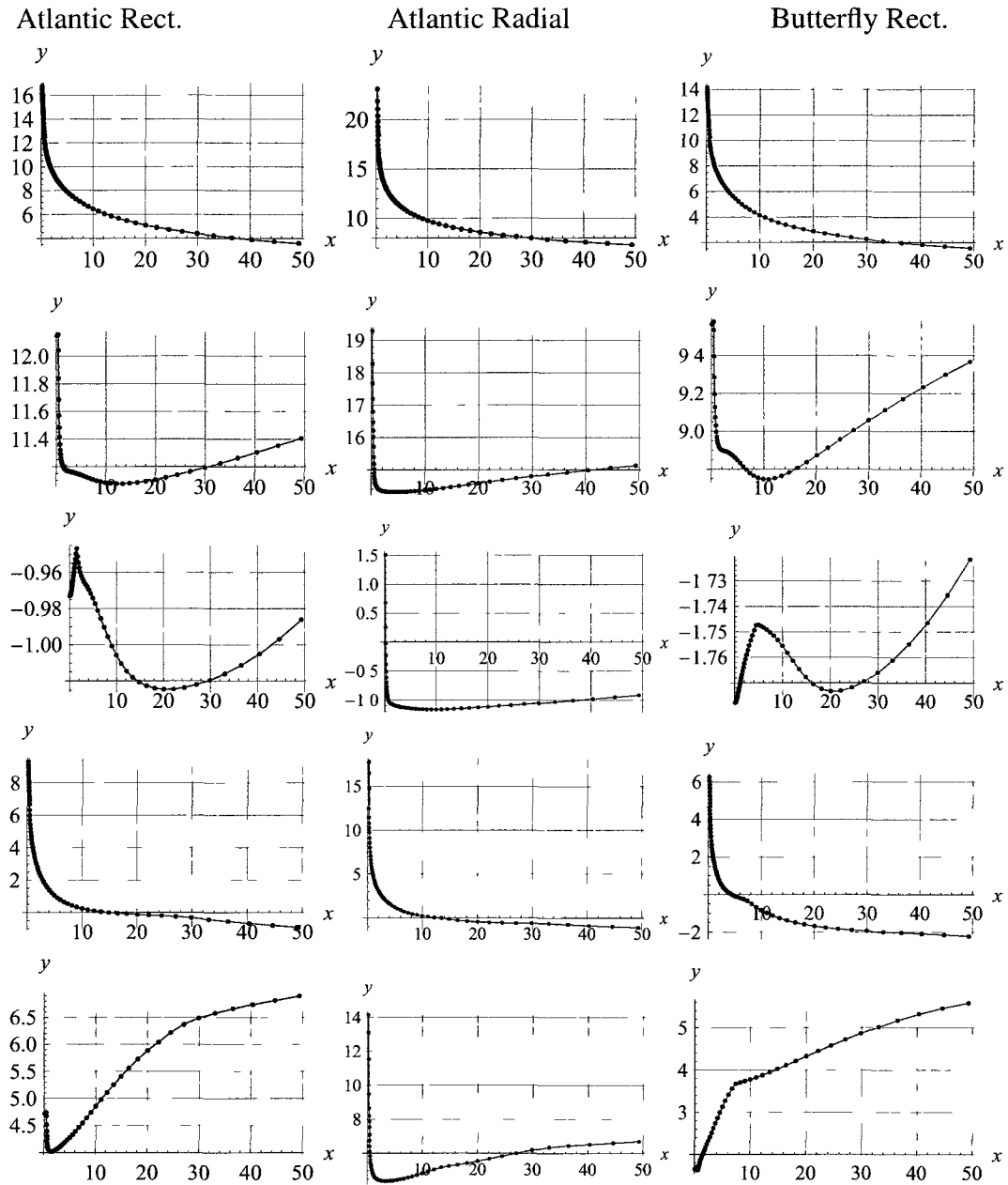


Figure 6.16: Min. obj. vs ω , Top to bottom: Curv., Curv.Rate, Power, Act., Act.Rate

Cownose Rect.

Cownose Radial

Cownose Radial Shifted

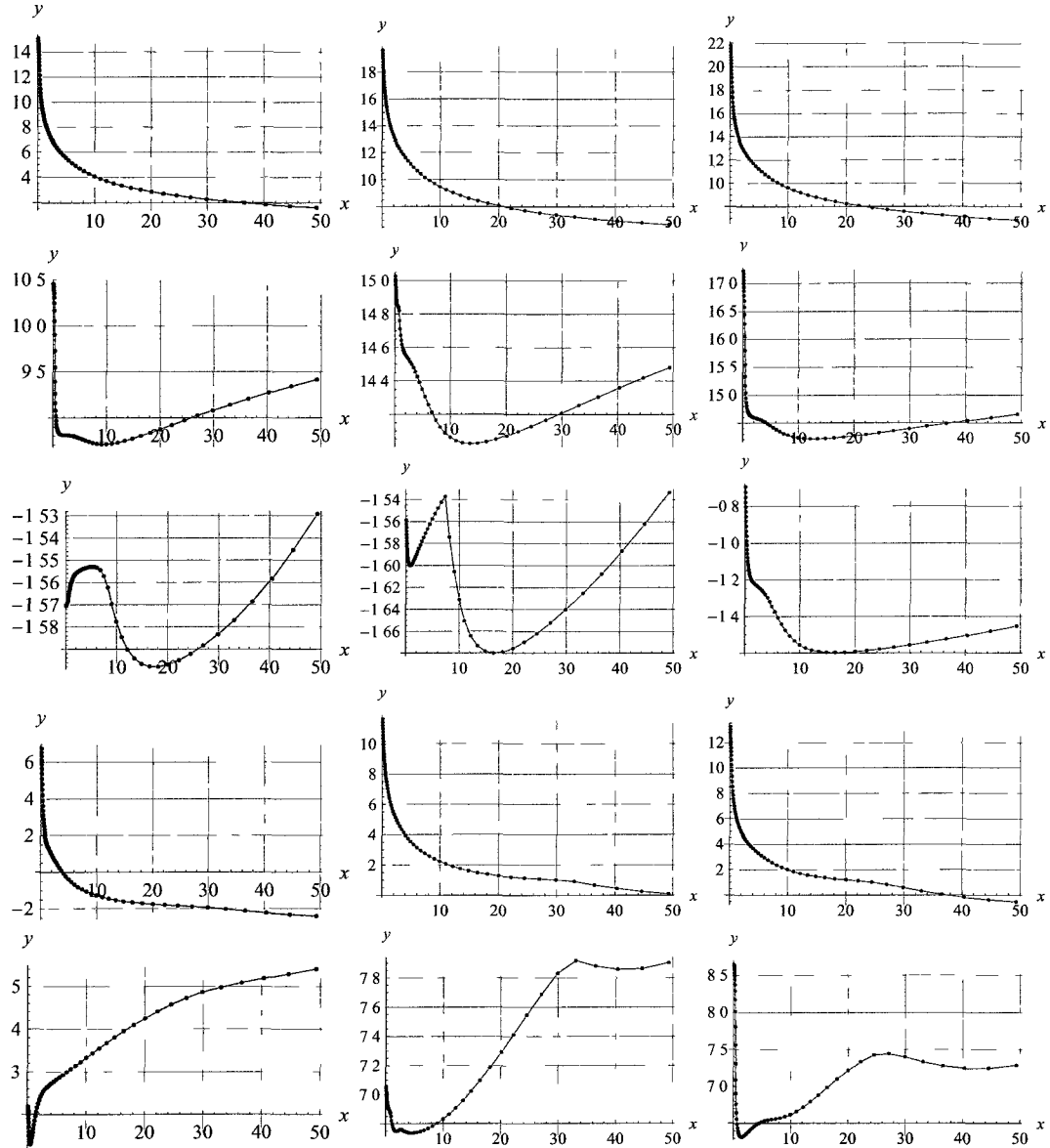


Figure 6.17: Min. obj. vs ω (continued), Top to bottom: Curv., Curv.Rate, Power, Act., Act.Rate

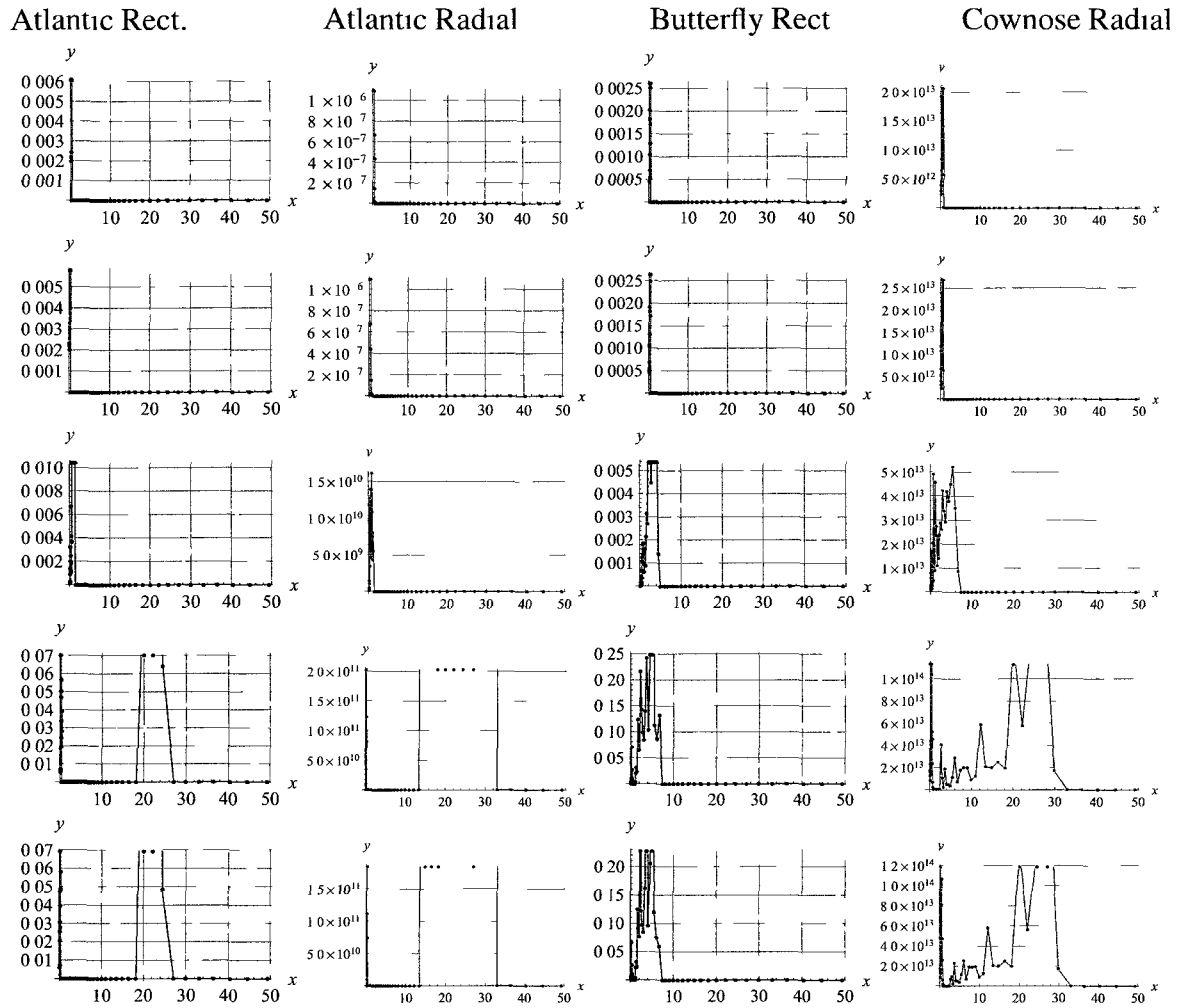


Figure 6.18: Symmetry vs ω (zero:symmetric, nonzero:anti-symmetric), Top to bottom: Curv., Curv.Rate, Power, Act., Act.Rate

6.6.2 Minimum curvature rate gaits

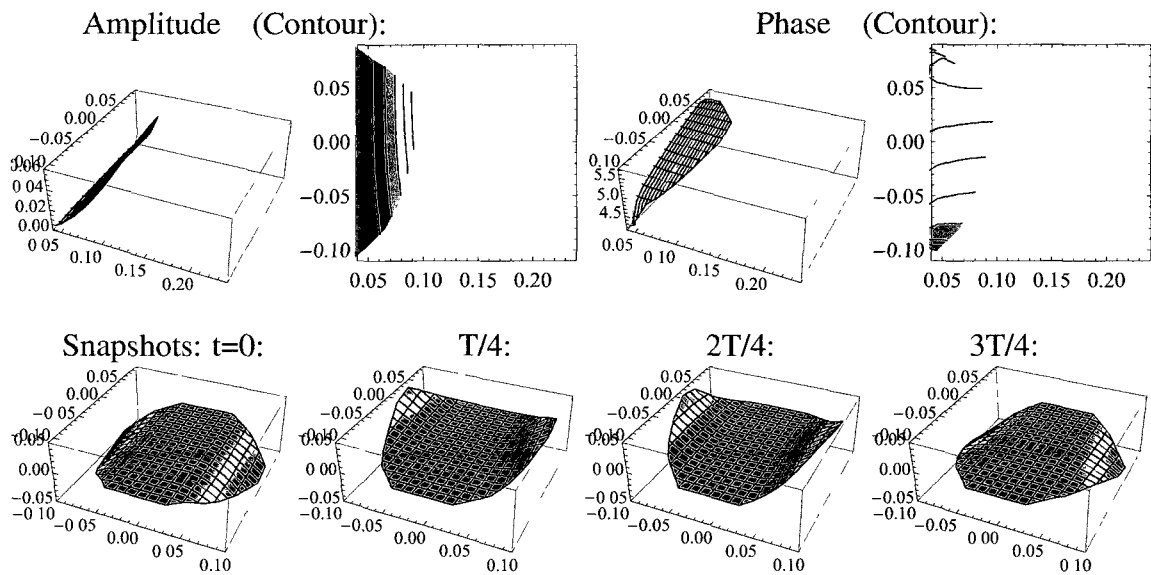


Figure 6.19: Minimum curvature rate gait for Atlantic rectangular grid.

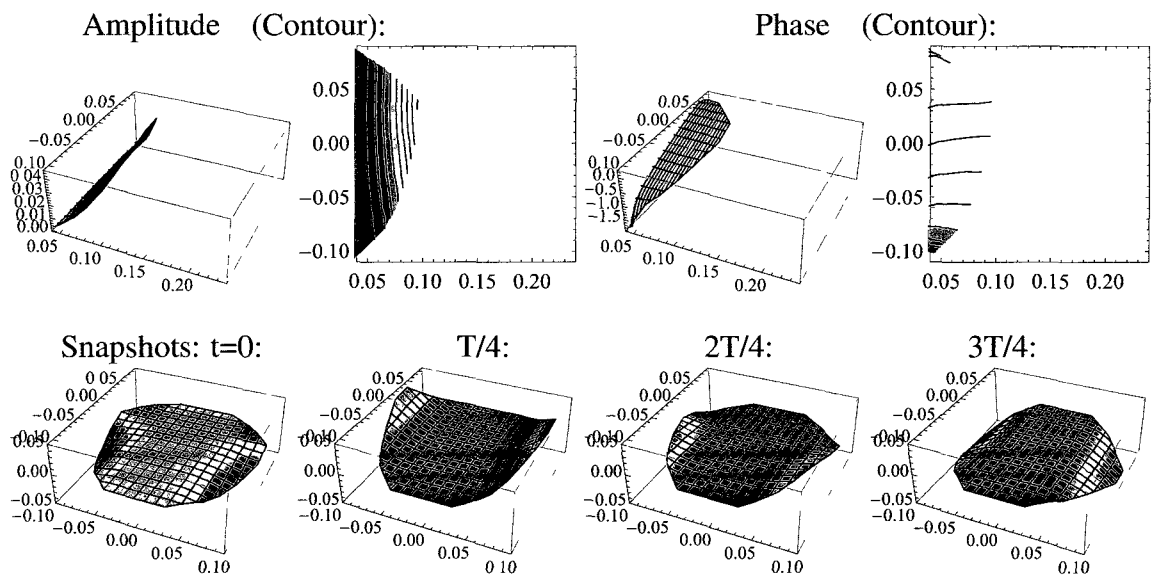


Figure 6.20: Minimum curvature rate gait at ω_{bio} for Atlantic rectangular grid.

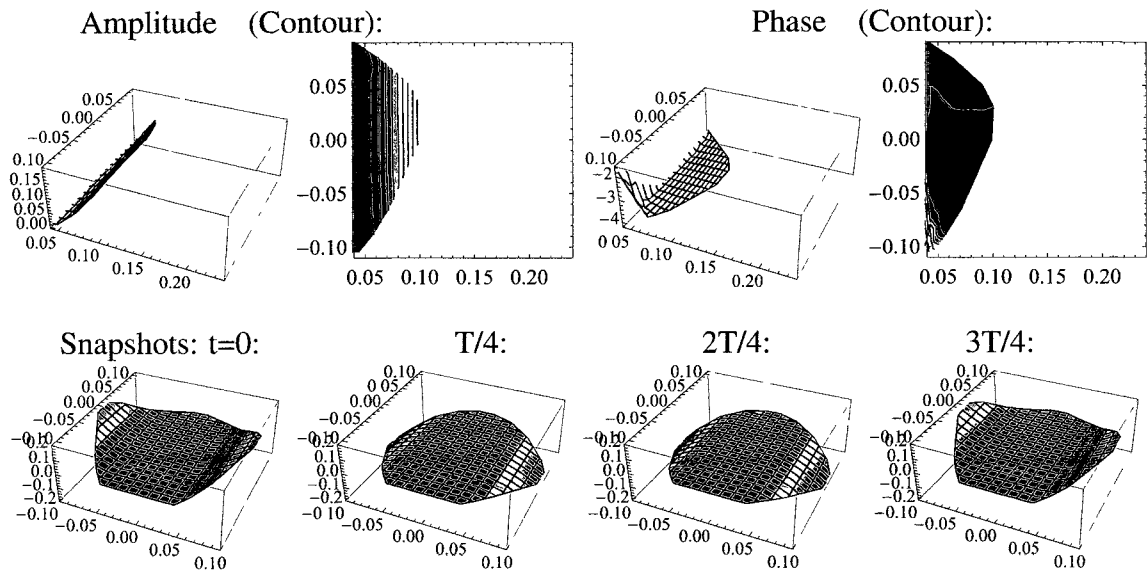


Figure 6.21: Minimum curvature rate gait for Atlantic radial grid.

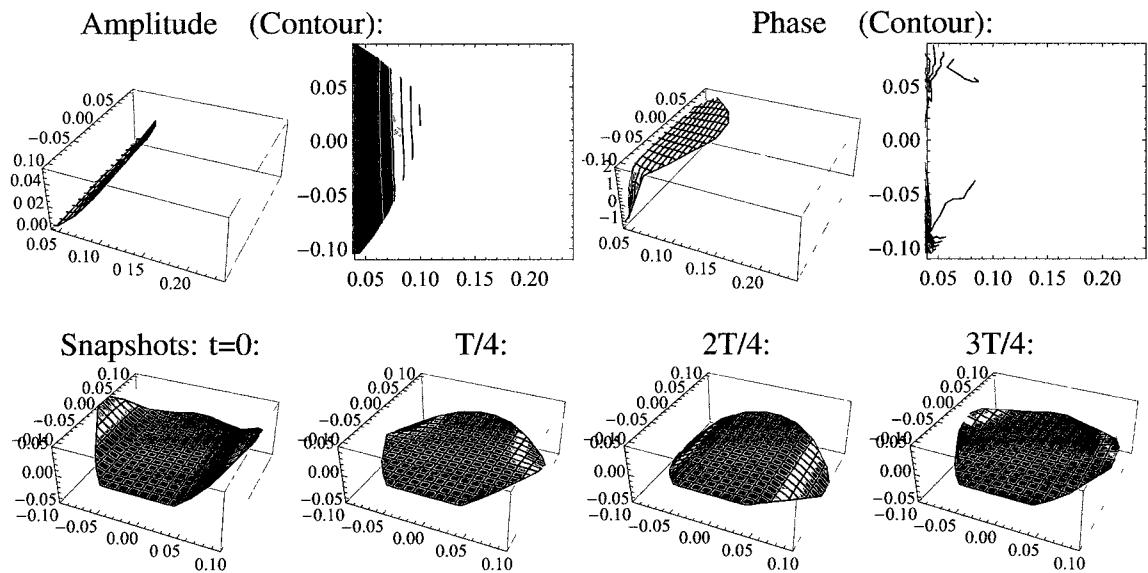


Figure 6.22: Minimum curvature rate gait at ω_{bio} for Atlantic radial grid.

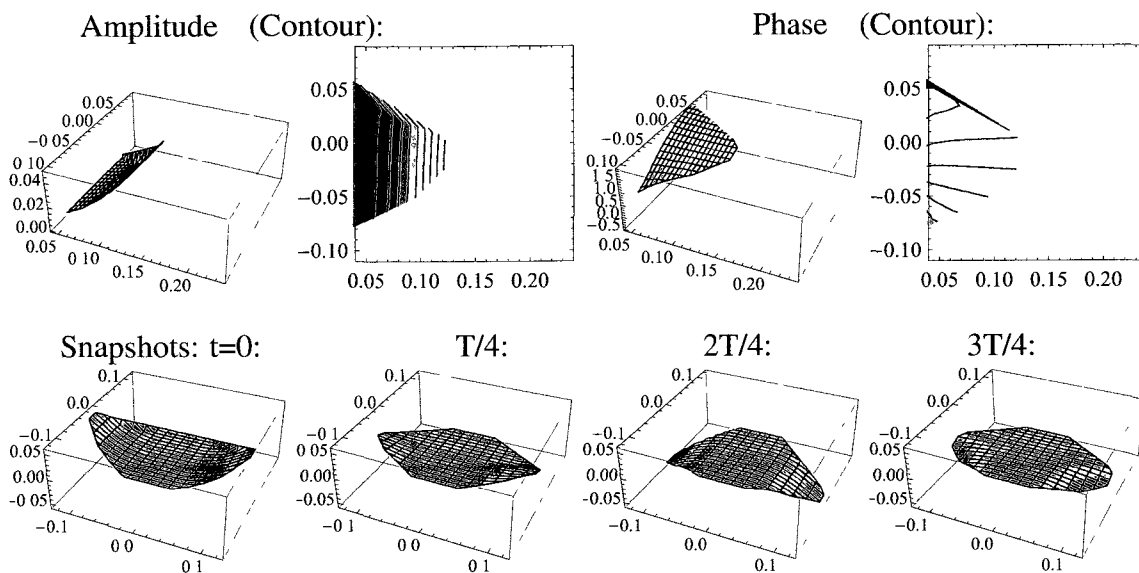


Figure 6.23: Minimum curvature rate gait for Butterfly rectangular grid.

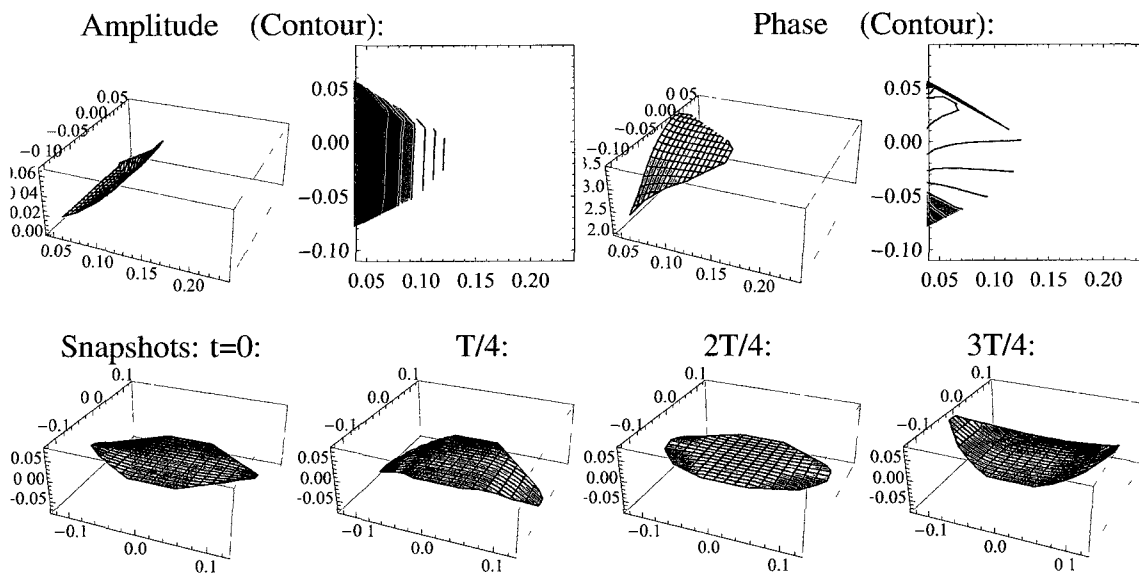


Figure 6.24: Minimum curvature rate gait at ω_{bio} for Butterfly rectangular grid.

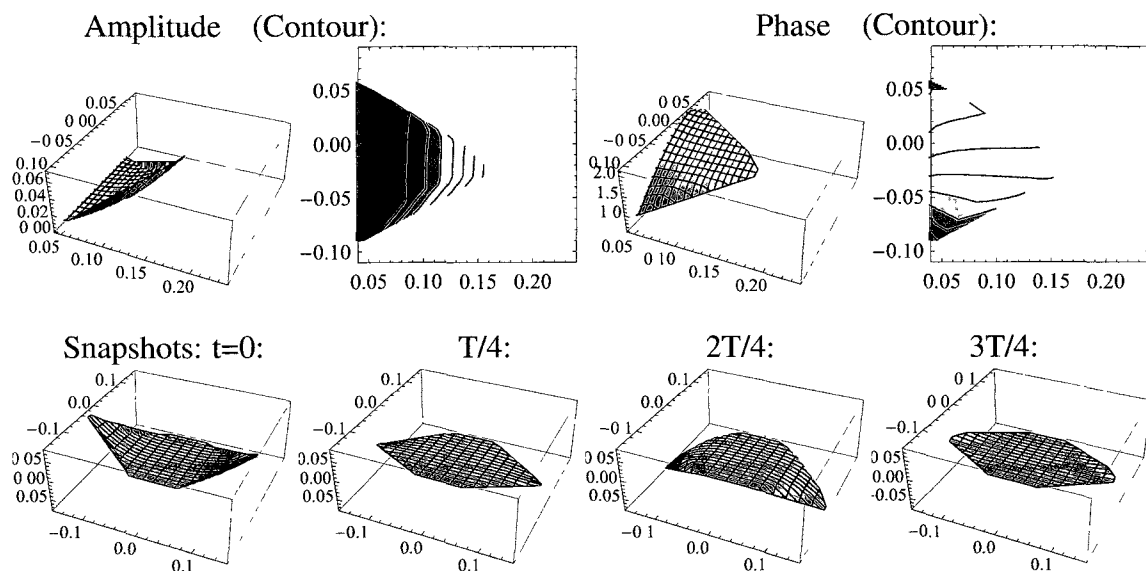


Figure 6.25: Minimum curvature rate gait for Cownose rectangular grid (symmetric constraint).

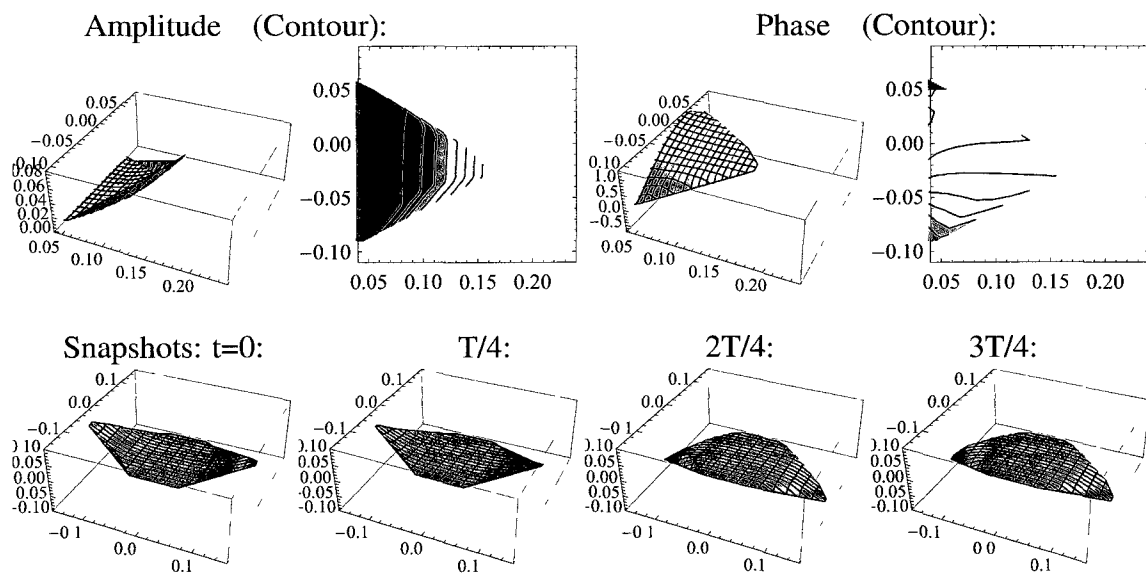


Figure 6.26: Minimum curvature rate gait at ω_{b0} for Cownose rectangular grid (symmetric constraint).

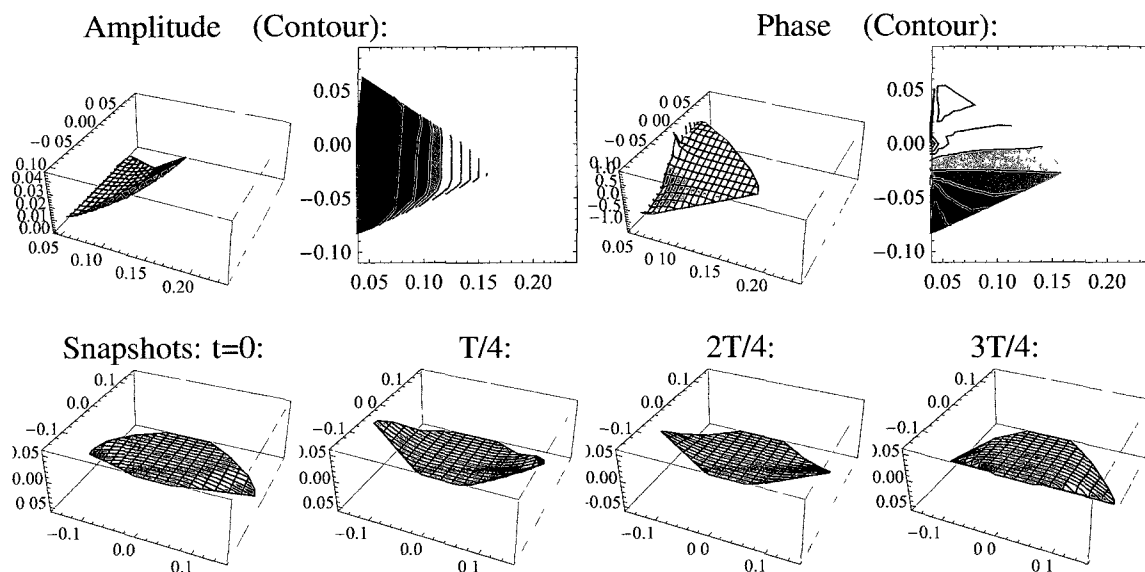


Figure 6.27: Minimum curvature rate gait for Cownose radial grid.

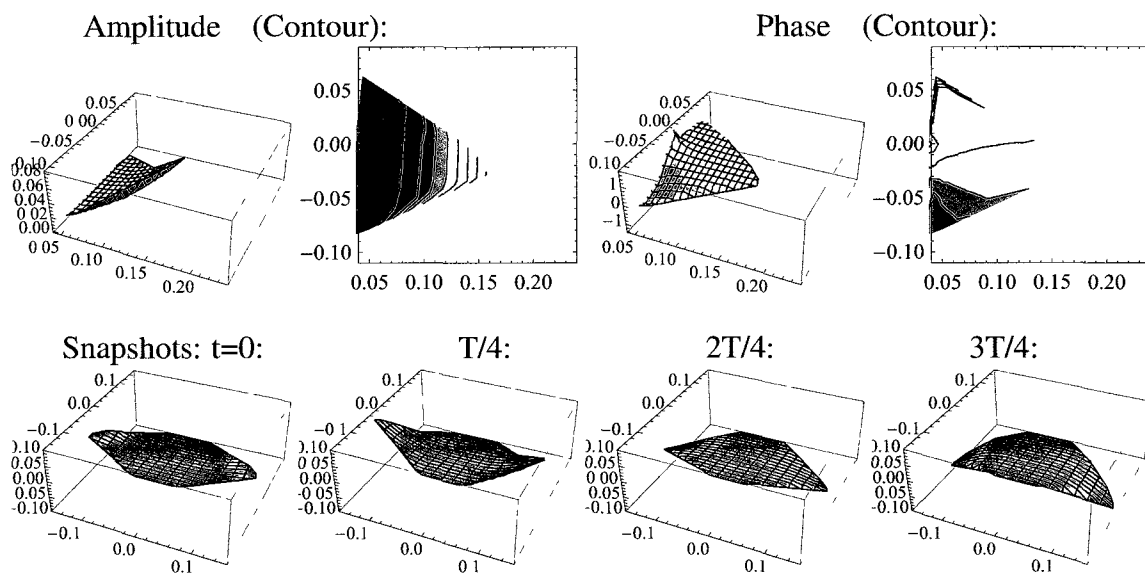


Figure 6.28: Minimum curvature rate gait at ω_{bio} for Cownose radial grid.

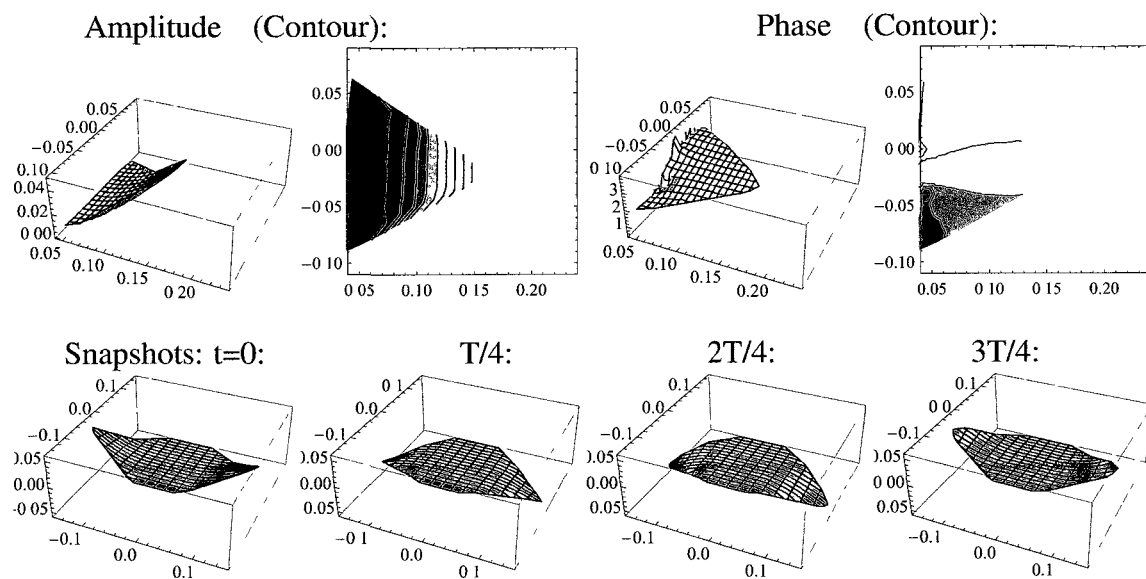


Figure 6.29: Minimum curvature rate gait for Cownose radial shifted grid (symmetric constraint).

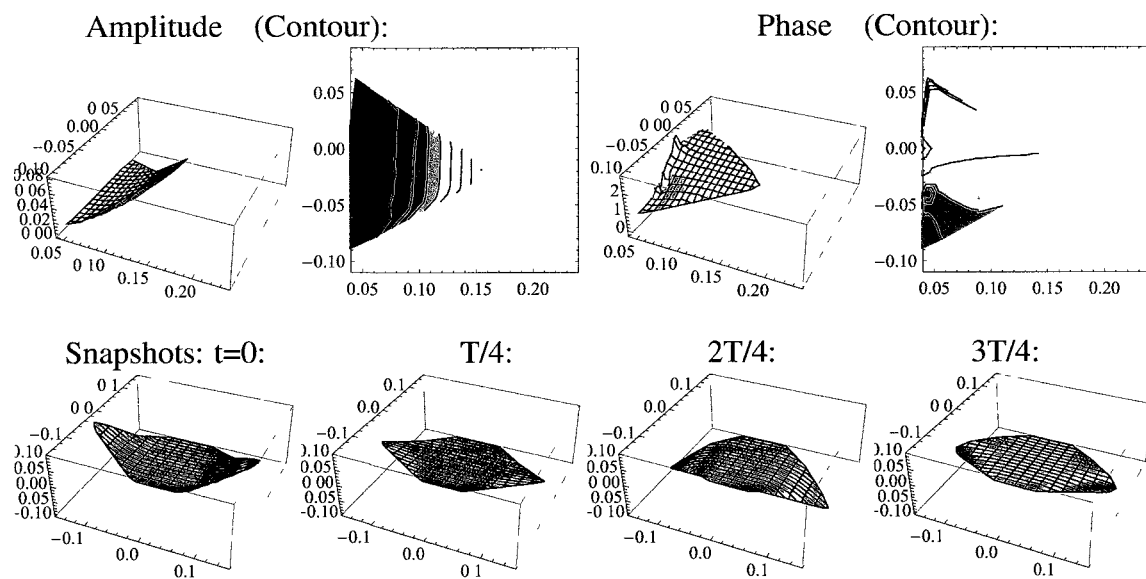


Figure 6.30: Minimum curvature rate gait at ω_{bio} for Cownose radial shifted grid (symmetric constraint).

6.6.3 Minimum power gaits

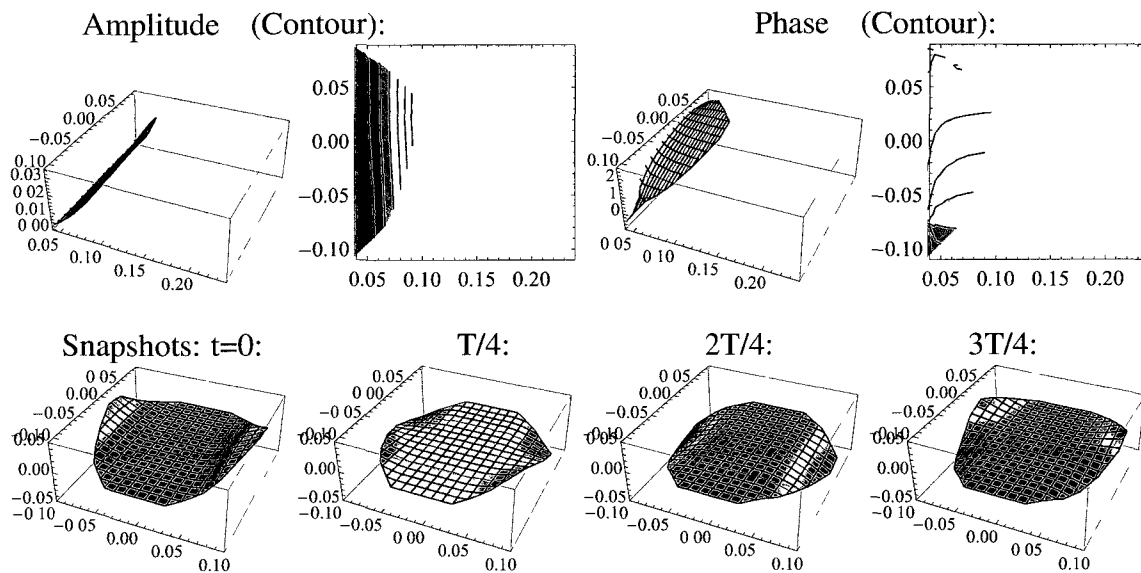


Figure 6.31: Minimum power gait for Atlantic rectangular grid.

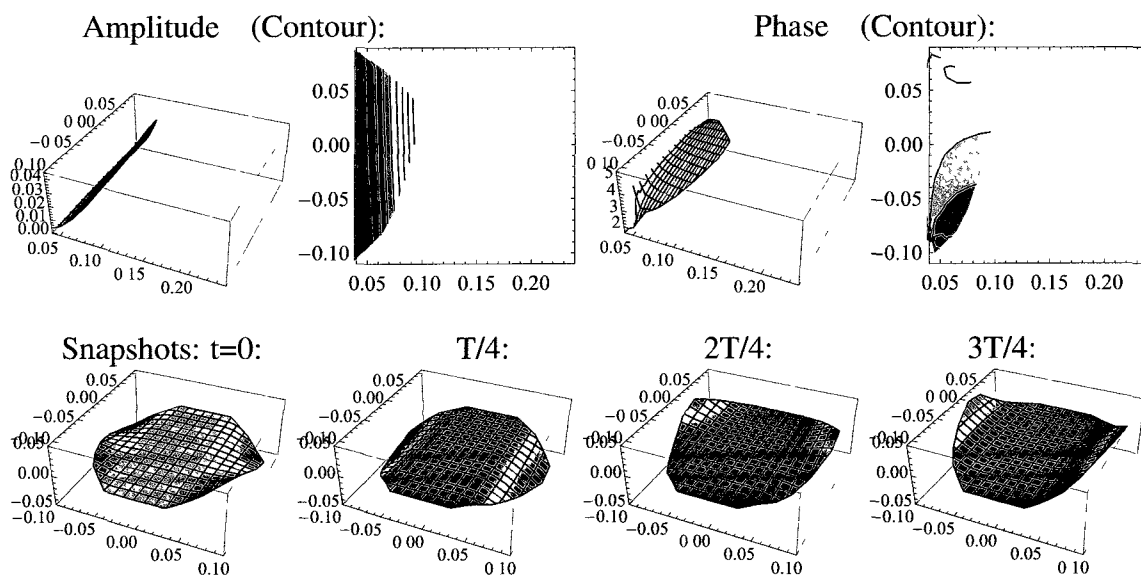


Figure 6.32: Minimum power gait at ω_{bio} for Atlantic rectangular grid.

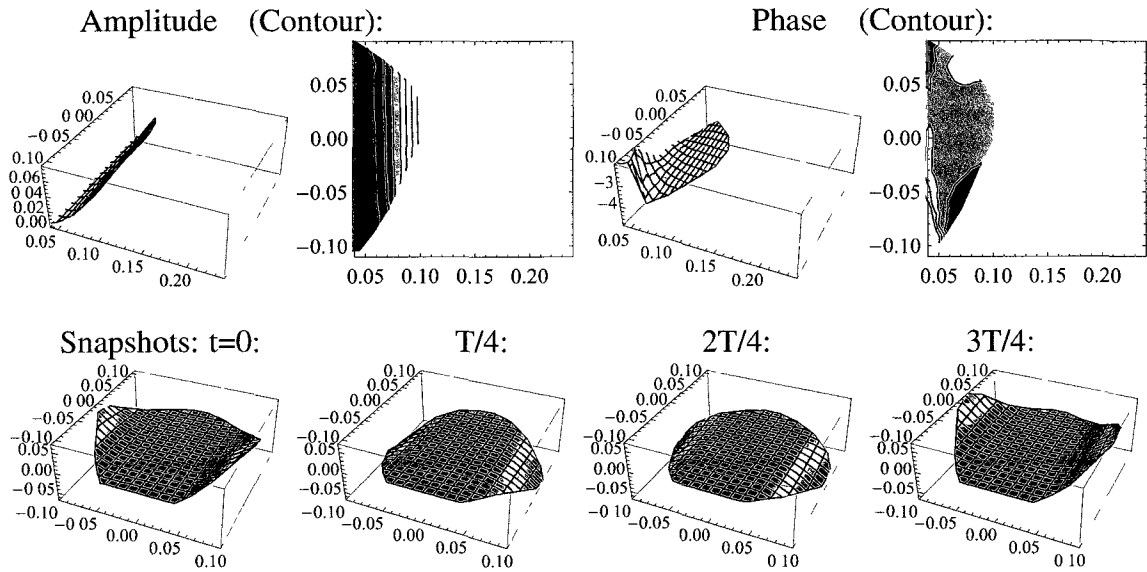


Figure 6.33: Minimum power gait for Atlantic radial grid.

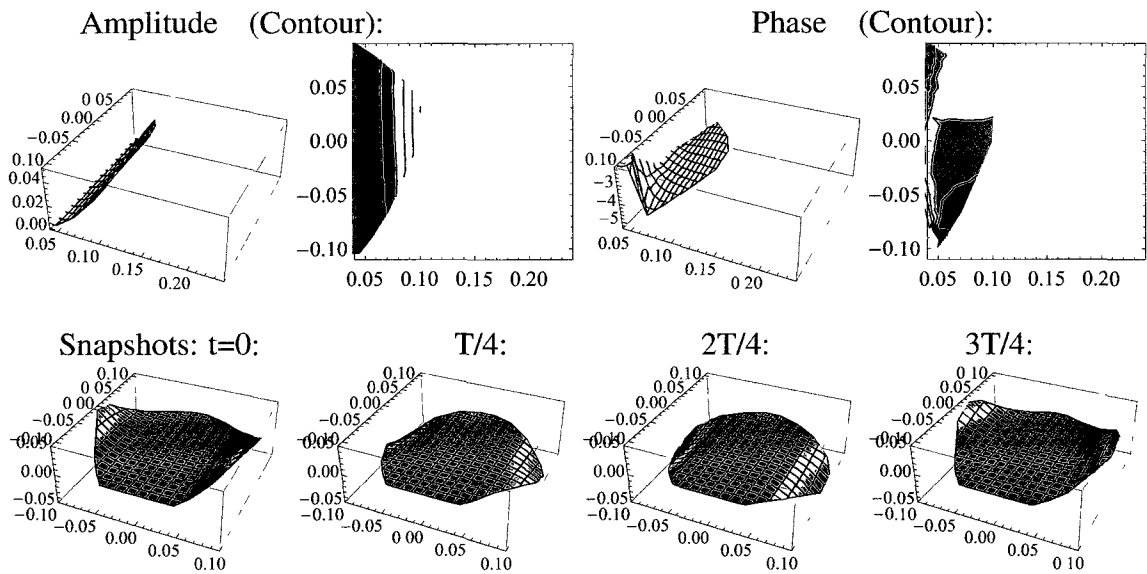


Figure 6.34: Minimum power gait at ω_{bio} for Atlantic radial grid.

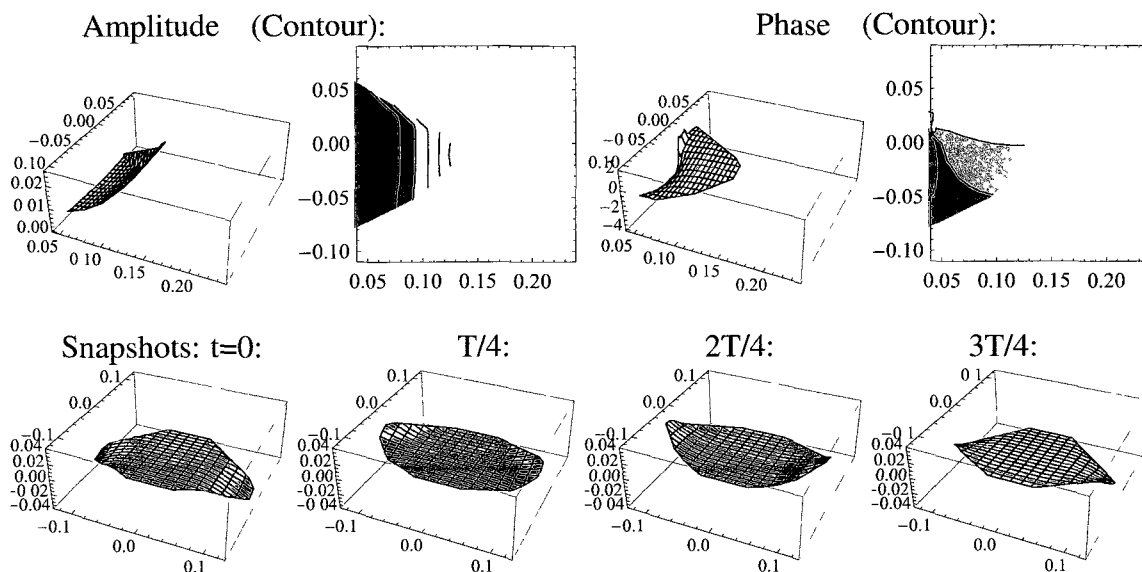


Figure 6.35: Minimum power gait for Butterfly rectangular grid.

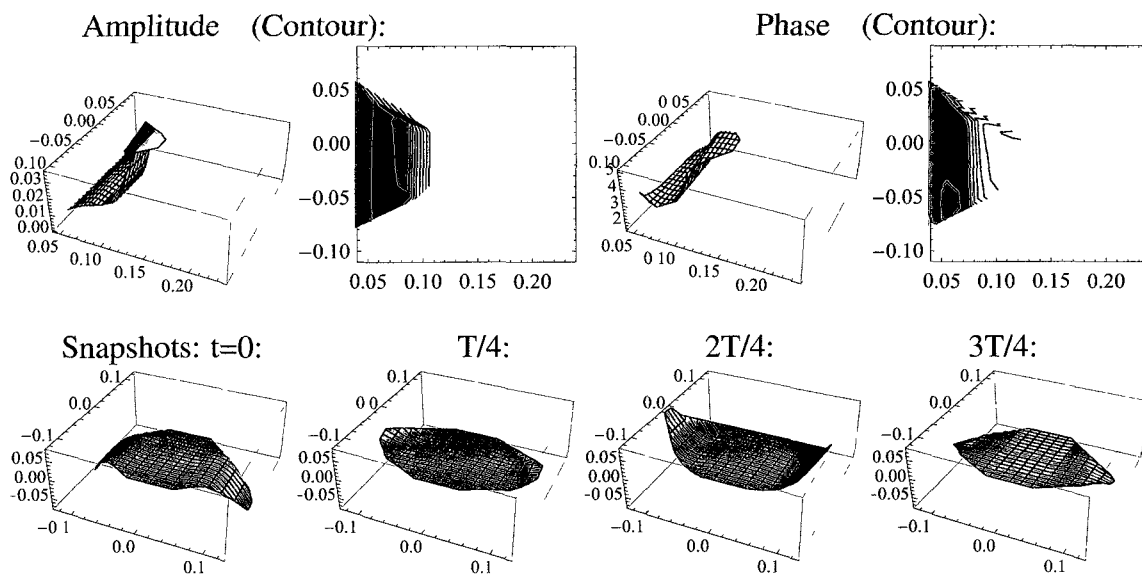


Figure 6.36: Minimum power gait at ω_{bio} for Butterfly rectangular grid.

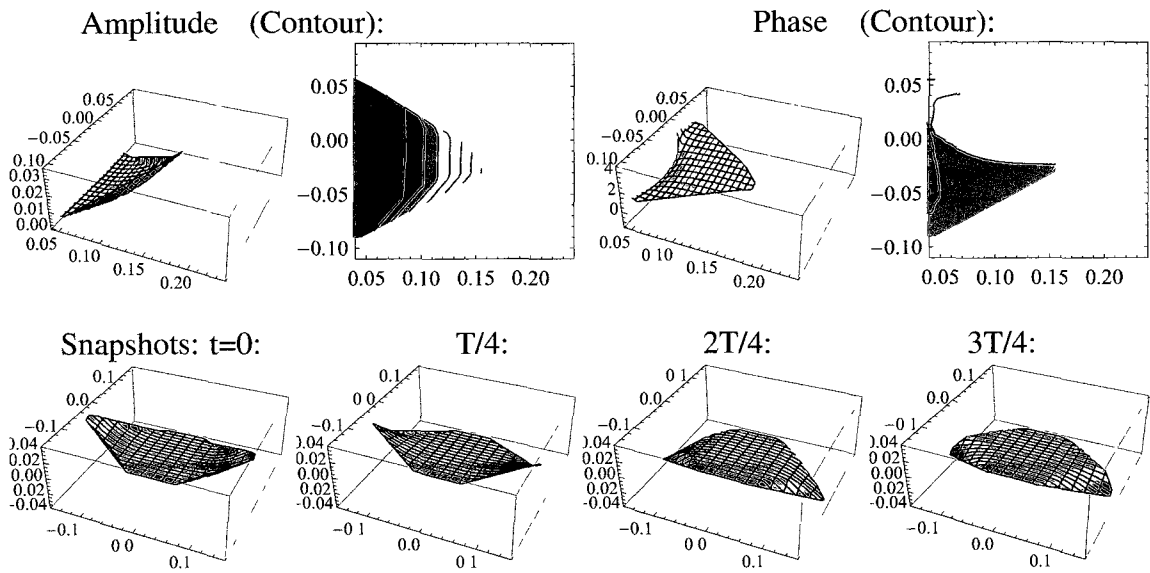


Figure 6.37: Minimum power gait for Cownose rectangular grid (symmetric constraint).

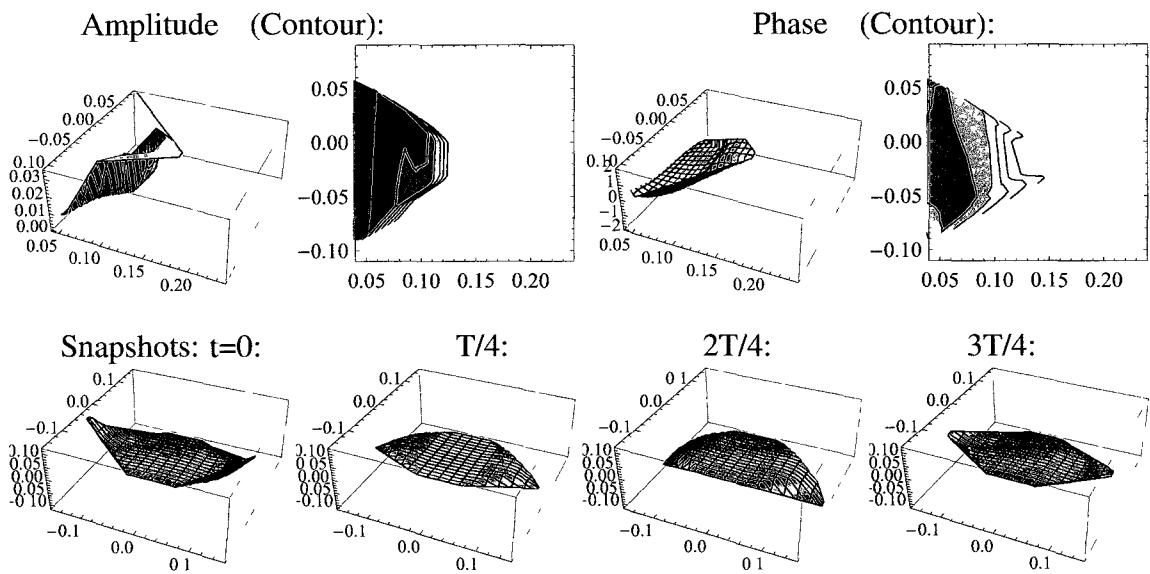


Figure 6.38: Minimum power gait at ω_{b0} for Cownose rectangular grid (symmetric constraint).

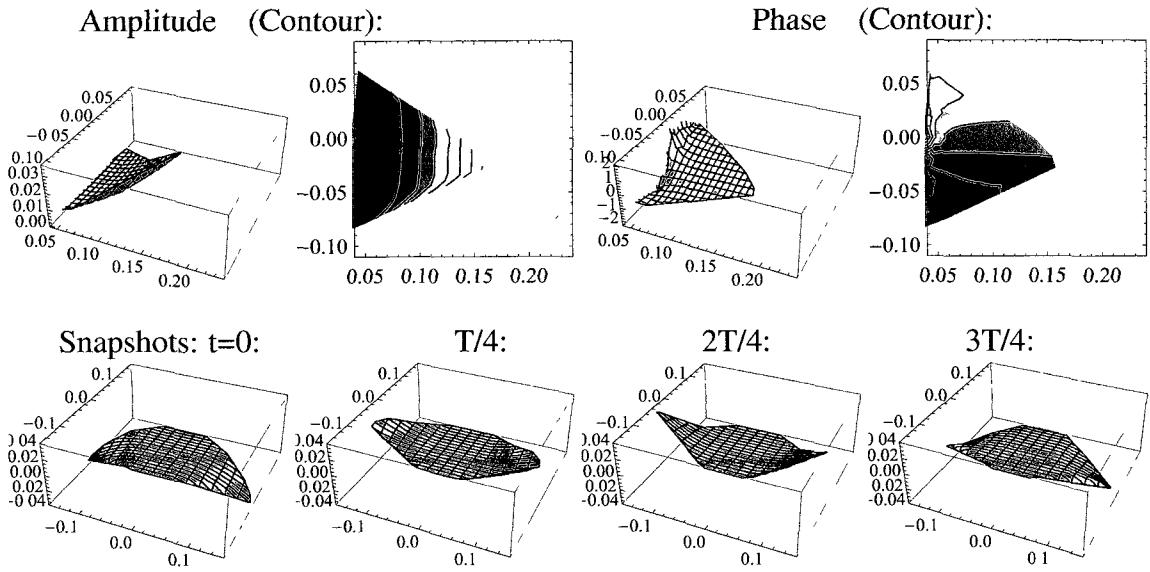


Figure 6.39: Minimum power gait for Cownose radial grid.

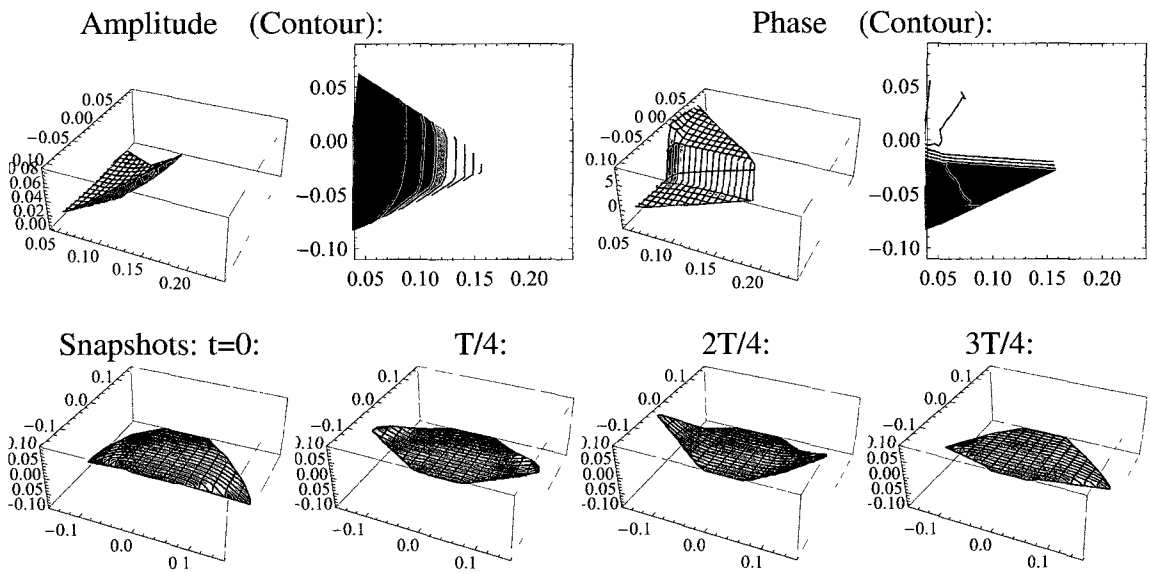


Figure 6.40: Minimum power gait at ω_{bio} for Cownose radial grid.

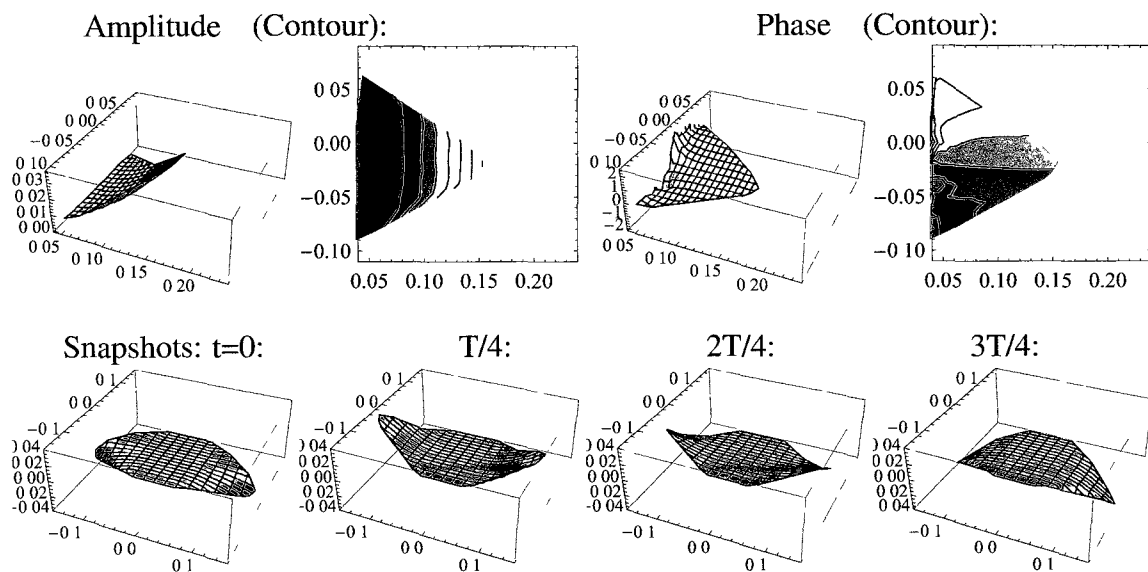


Figure 6.41: Minimum power gain for Cownose radial shifted grid (symmetric constraint).

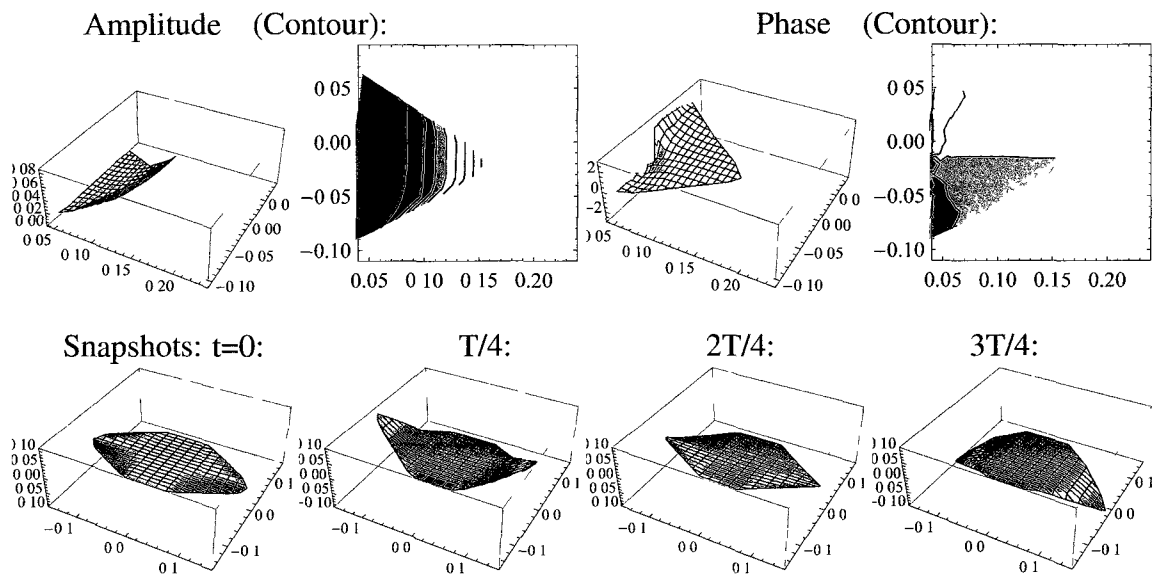


Figure 6.42: Minimum power gain at ω_{br0} for Cownose radial shifted grid (symmetric constraint).

6.6.4 Minimum actuation rate gaits

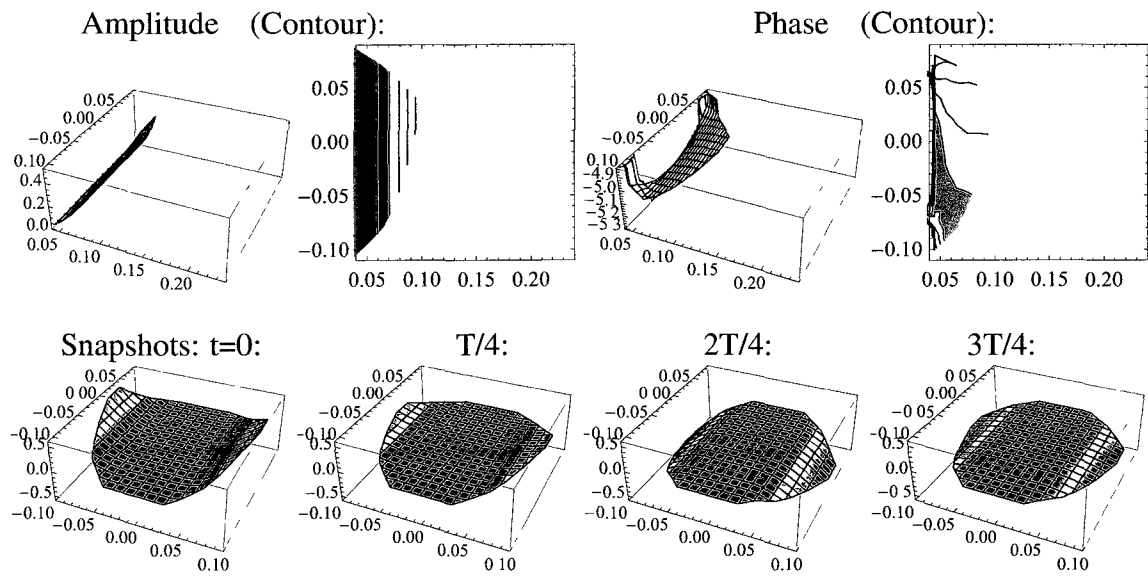


Figure 6.43: Minimum actuation rate gait for Atlantic rectangular grid.

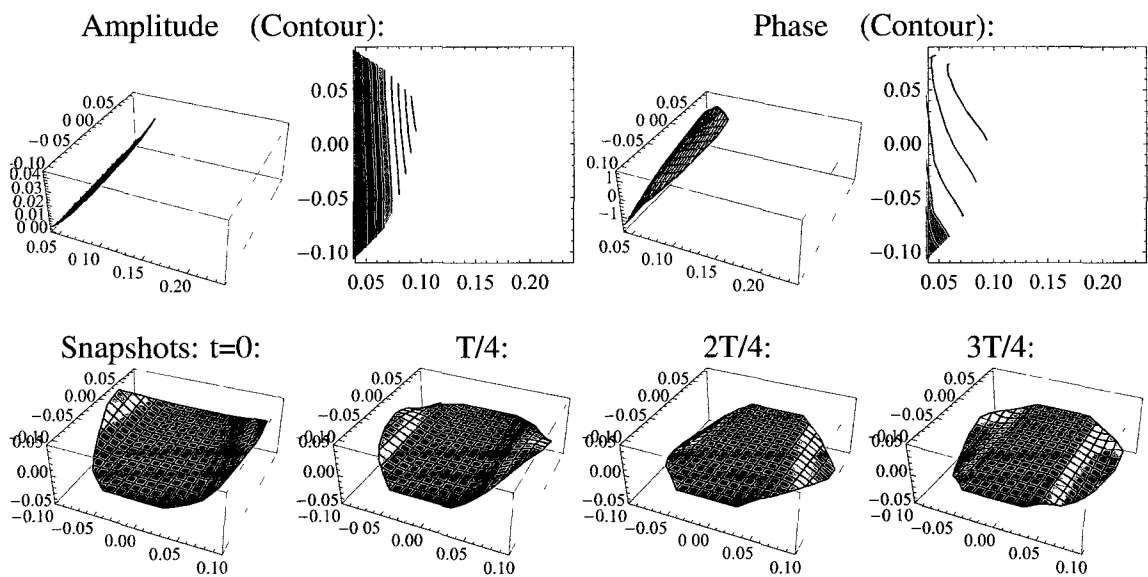


Figure 6.44: Minimum actuation rate gait at ω_{b10} for Atlantic rectangular grid.

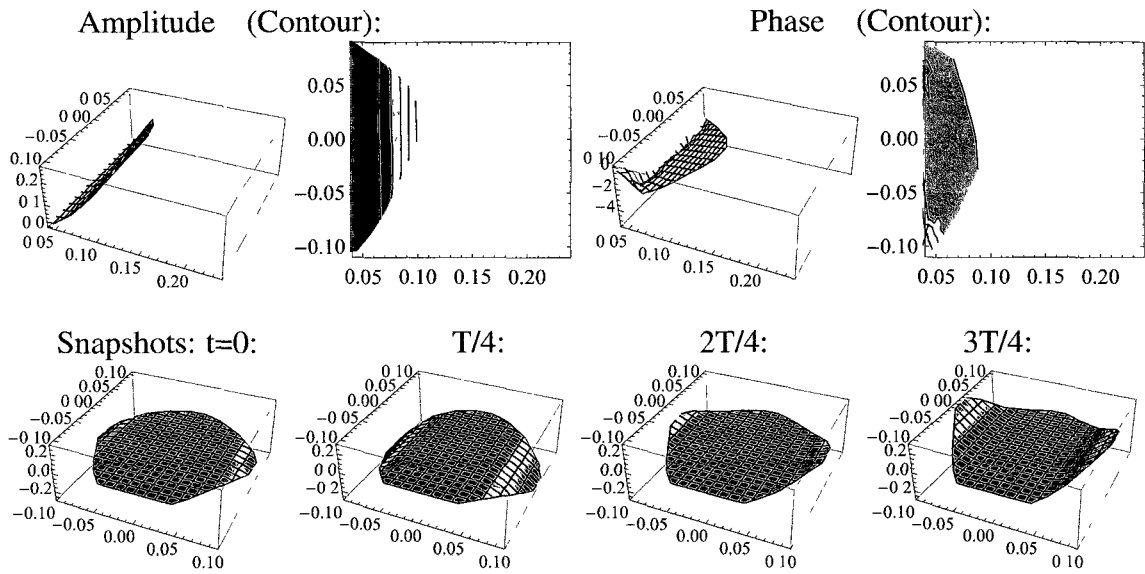


Figure 6.45: Minimum actuation rate gait for Atlantic radial grid.

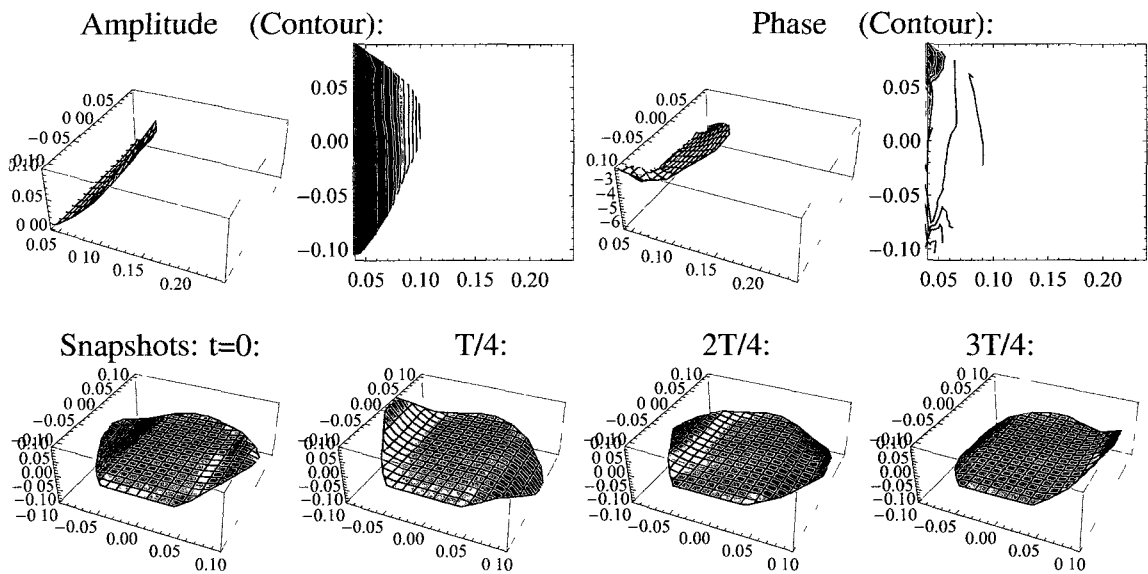


Figure 6.46: Minimum actuation rate gait at ω_{bio} for Atlantic radial grid.

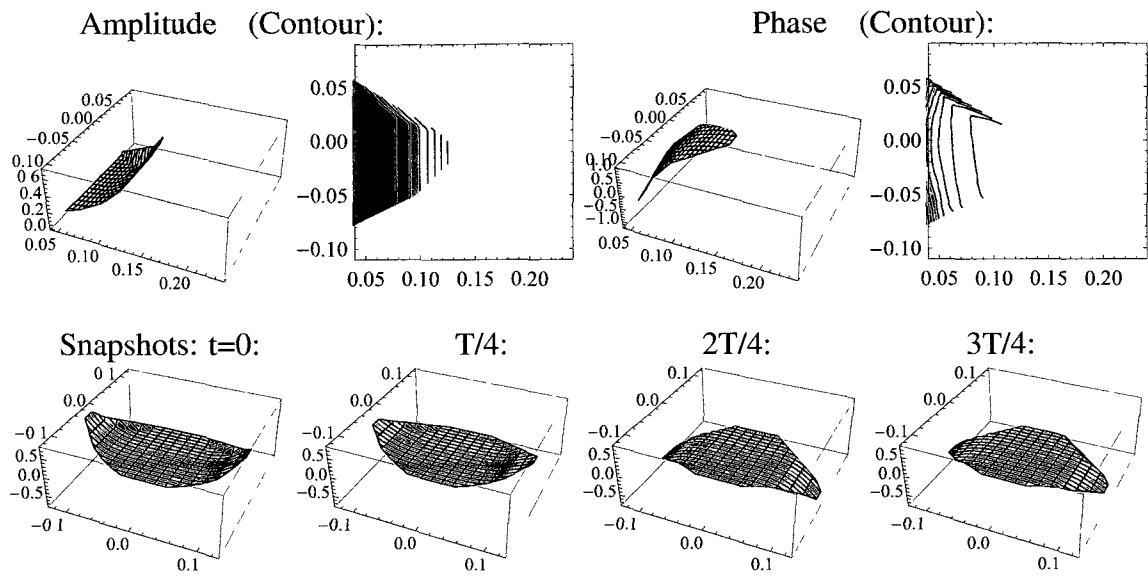


Figure 6.47: Minimum actuation rate gait for Butterfly rectangular grid.

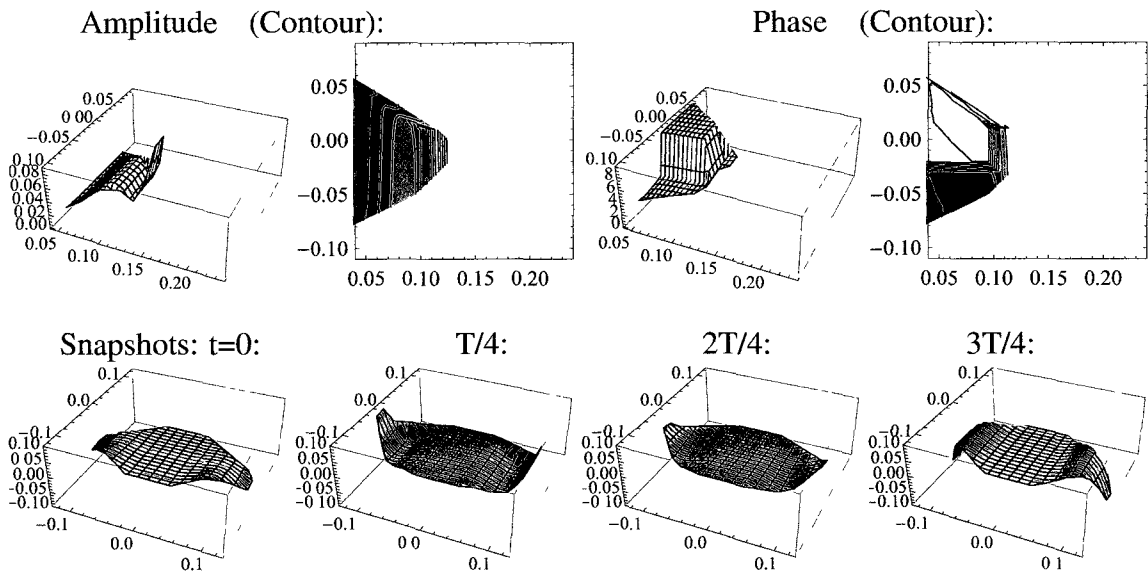


Figure 6.48: Minimum actuation rate gait at ω_{bio} for Butterfly rectangular grid.

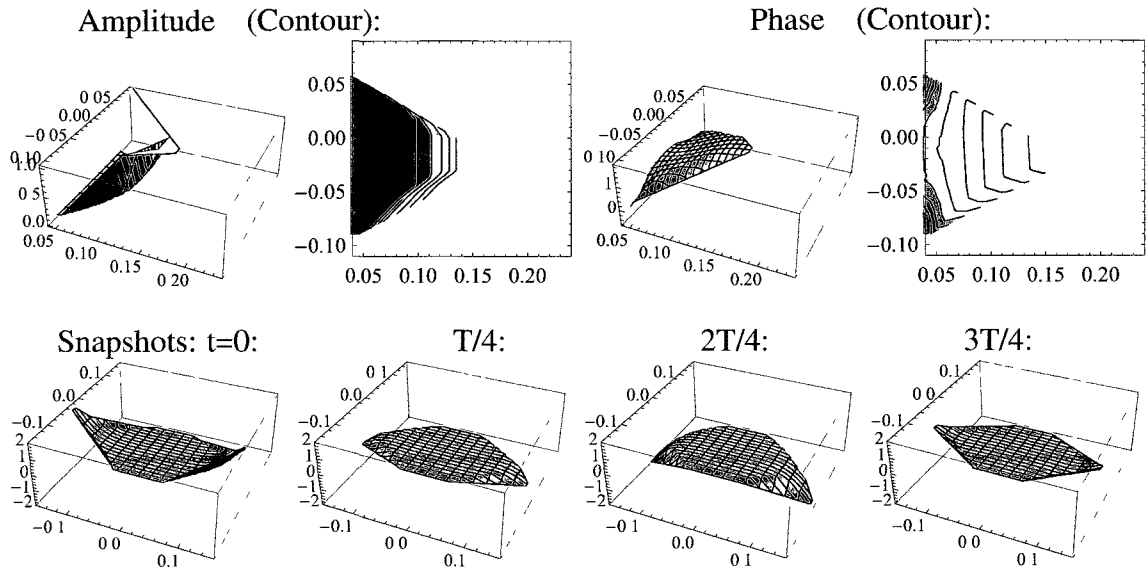


Figure 6.49: Minimum actuation rate gait for Cownose rectangular grid (symmetric constraint).

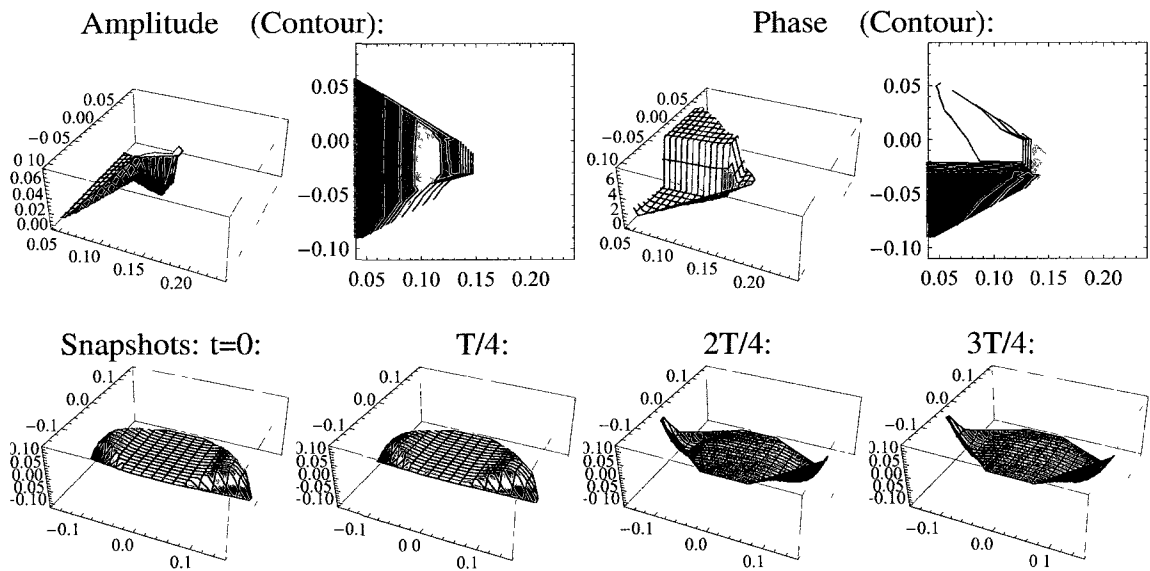


Figure 6.50: Minimum actuation rate gait at ω_{b0} for Cownose rectangular grid (symmetric constraint).

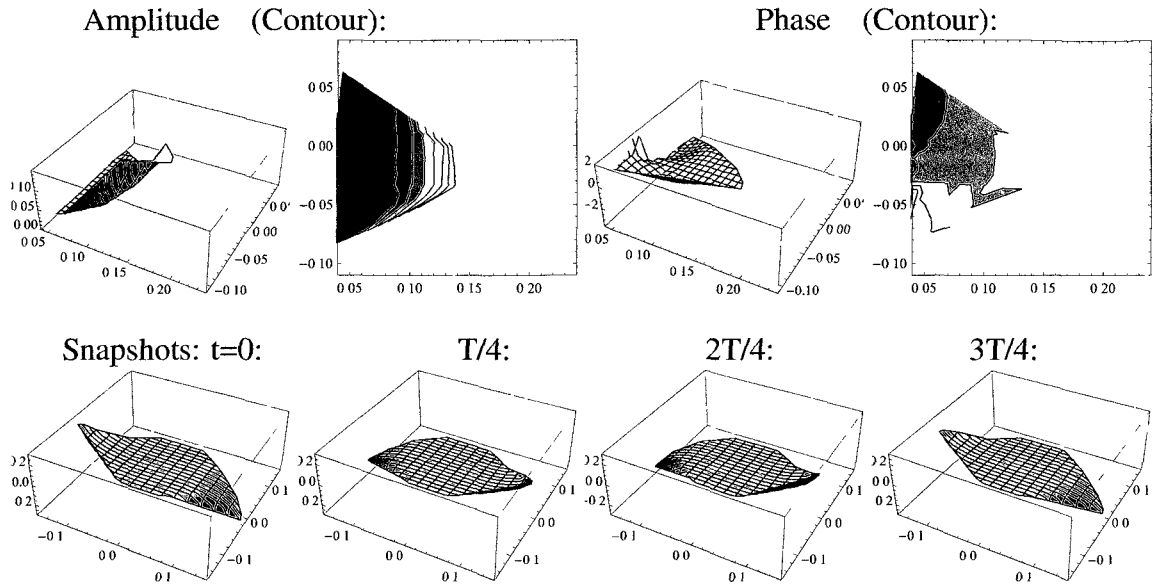


Figure 6.51: Minimum actuation rate gait for Cownose radial grid.

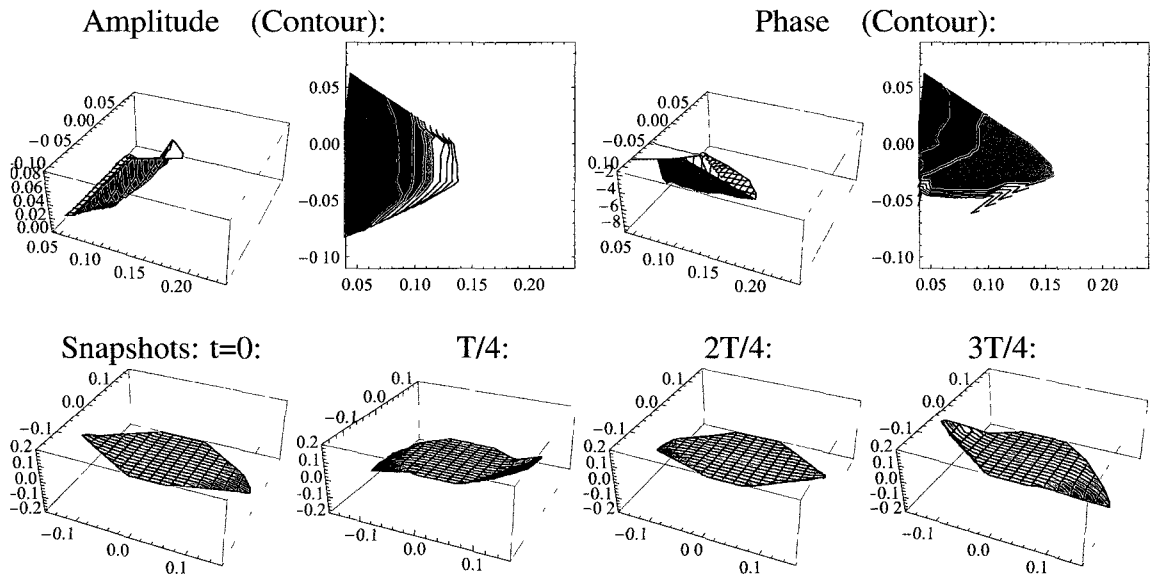


Figure 6.52: Minimum actuation rate gait at ω_{bio} for Cownose radial grid.

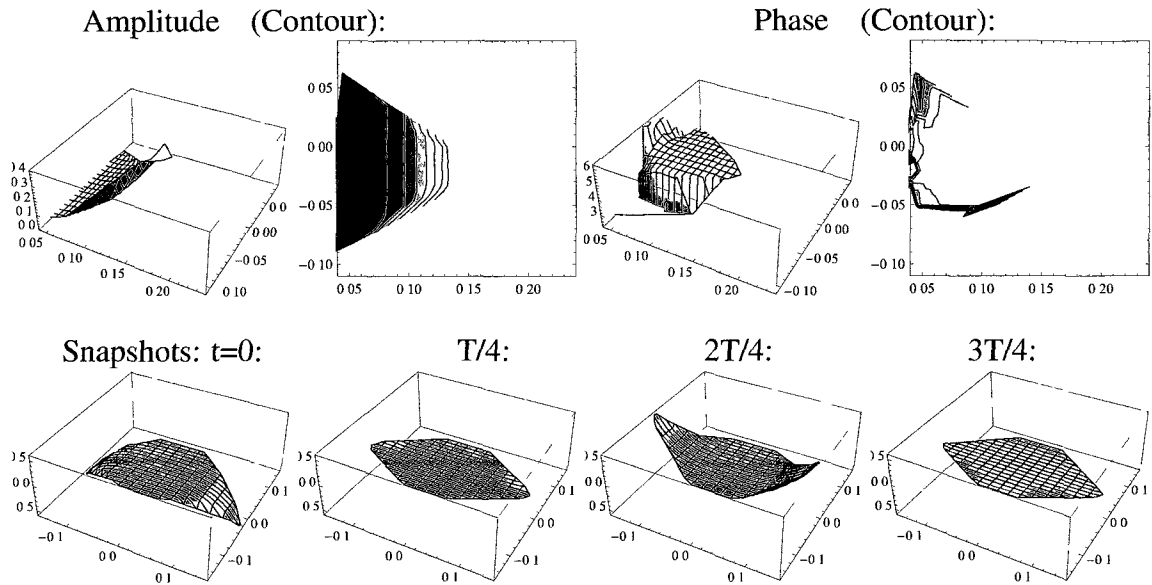


Figure 6.53: Minimum actuation rate gait for Cownose radial shifted grid (symmetric constraint).

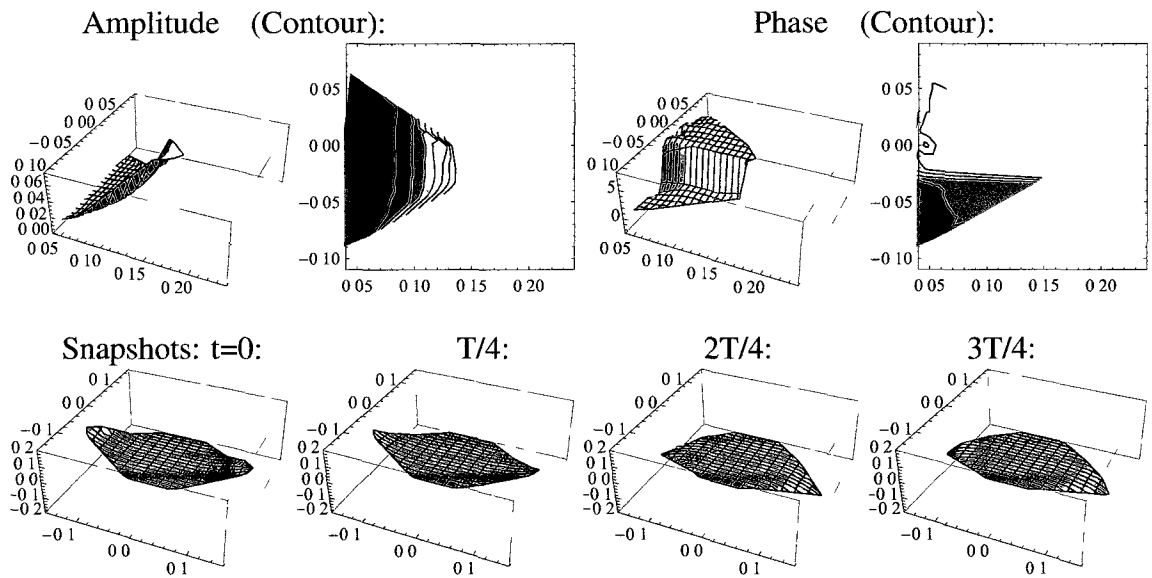


Figure 6.54: Minimum actuation rate gait at ω_{b10} for Cownose radial shifted grid (symmetric constraint).

	ω [rad/s]	Tip Amp. [cm]	Phase Lag [rad]
Curv. Rate	12	6	1
Power	20	3	2
Act. Rate	1.5	50	≈ 0

Table 6.8: Optimal gaits for the Atlantic ray, rectangular grid.

	ω [rad/s]	Tip Amp. [cm]	Phase Lag [rad]
Curv. Rate	4	20	0.25
Power	10	8	0.5
Act. Rate	3.5	25	0.25

Table 6.9: Optimal gaits for the Atlantic ray, radial grid.

	ω [rad/s]	Tip Amp. [cm]	Phase Lag [rad]
Curv. Rate	15.7	4.5	1.5
Power	15.7	4	1.5
Act. Rate	15.7	4.25	2.5

Table 6.10: Optimal gaits for the Atlantic ray, rectangular grid, observed ω .

	ω [rad/s]	Tip Amp. [cm]	Phase Lag [rad]
Curv. Rate	15.7	5	0.5
Power	15.7	5	1.5
Act. Rate	15.7	10	≈ 0

Table 6.11: Optimal gaits for the Atlantic ray, radial grid, observed ω .

	ω [rad/s]	Tip Amp. [cm]	Phase Lag [rad]
Curv. Rate	11	5	1.5
Power	21	2.5	2
Act. Rate	1	70	≈ 0

Table 6.12: Optimal gaits for the Butterfly ray, rectangular grid.

	ω [rad/s]	Tip Amp. [cm]	Phase Lag [rad]
Curv. Rate	8.38	7	1.5
Power	8.38	7	1
Act. Rate	8.38	9	1

Table 6.13: Optimal gaits for the Butterfly ray, rectangular grid, observed ω .

	ω [rad/s]	Tip Amp. [cm]	Phase Lag [rad]
Curv. Rate	9	7	1.5
Power	17	3.5	2
Act. Rate	0.5	200	≈ 0

Table 6.14: Optimal gaits for the Cownose ray, rectangular grid (symmetric).

	ω [rad/s]	Tip Amp. [cm]	Phase Lag [rad]
Curv. Rate	13	5	1.5
Power	16	3.5	2
Act. Rate	4.5	20	≈ 0

Table 6.15: Optimal gaits for the Cownose ray, radial grid.

	ω [rad/s]	Tip Amp. [cm]	Phase Lag [rad]
Curv. Rate	12	5	1.5
Power	16	3.5	2
Act. Rate	1.5	60	≈ 0

Table 6.16: Optimal gaits for the Cownose ray, shifted radial grid (symmetric).

	ω [rad/s]	Tip Amp. [cm]	Phase Lag [rad]
Curv. Rate	7.85	8	1
Power	7.85	10	0.5
Act. Rate	7.85	8	0.5

Table 6.17: Optimal gaits for the Cownose ray, rectangular grid (symmetric), observed ω .

	ω [rad/s]	Tip Amp. [cm]	Phase Lag [rad]
Curv. Rate	7.85	8	2
Power	7.85	8	2
Act. Rate	7.85	15	≈ 0

Table 6.18: Optimal gaits for the Cownose ray, radial grid, observed ω .

	ω [rad/s]	Tip Amp. [cm]	Phase Lag [rad]
Curv. Rate	7.85	8	1.5
Power	7.85	8	2.5
Act. Rate	7.85	10	2.5

Table 6.19: Optimal gaits for the Cownose ray, shifted radial grid (symmetric), observed ω .

Biography

Justin Blair was born in 1980 in Winchester, VA. Blair received a B.S. degree in 2002 with Distinction from the Mechanical and Aerospace Engineering (MAE) department in the School of Engineering and Applied Science at the University of Virginia (UVA), Charlottesville, VA. Blair's undergraduate thesis is titled "Validating a Finite Element Model for Predicting Thoracic Injury in Car Crashes." He was employed from 2002 to 2003 as a Mechanical Engineer at the Naval Surface Warfare Center in Dahlgren, VA. Presently, he



is a Research Assistant to Dr. T. Iwasaki in the Multidisciplinary University Research Initiative (MURI) team in UVA's MAE department, Charlottesville, VA, while he pursues a Ph.D. in Mechanical and Aerospace Engineering with a concentration in Dynamics and Control. His research interests include the dynamics and control of animal locomotion through modeling and analysis. Mr. Blair is a member of the American Society of Mechanical Engineers (ASME) and is a certified member of the honorary Mechanical Engineering fraternity, $\Pi T \Sigma$.

Bibliography

- [1] B.D.O. Anderson. Personal communication. 1998.
- [2] R.W. Brockett. On the rectification of vibratory motion. *Sensors and Actuators*, 20:91–96, 1989.
- [3] D.F. Hoyt and C.R. Taylor. Gait and the energetics of locomotion in horses. *Nature*, 292:239–240, 1981.
- [4] F.J. Diedrich and W.H. Warren. Why change gaits - dynamics of the walk run transition. *J. Experimental Psychology - Human Perception and Performance*, 21(1):183–202, 2000.
- [5] M. Sfakiotakis, D.M. Lane, and J.B.C. Davies. Review of fish swimming modes for aquatic locomotion. *IEEE journal of oceanic engineering*, 24(2):237–252, 1999.
- [6] A.J. Ijspeert, A. Crepsi, D. Ryczko, and J.M. Cabelguen. From swimming to walking with a salamander robot driven by a spinal cord model. *Science*, 315(5817):1416–1420, 2007.
- [7] J. Blair and T. Iwasaki. On the optimal harmonic gait for locomotion of mechanical rectifier systems. *Proc. IFAC World Congress*, 2008.
- [8] J. Blair and T. Iwasaki. A further result on the optimal harmonic gait for locomotion of mechanical rectifier systems. *Proc. American Control Conference*, 2009.

- [9] J. Blair and T. Iwasaki. Optimal gaits for mechanical rectifier systems. *IEEE Trans. Auto. Contr.*, 56(1):59–71, 2011.
- [10] J. Blair and T. Iwasaki. Modeling of flapping-wing rectifier systems and optimal gait analysis. *Proc. IFAC World Congress*, 2011.
- [11] C.J. Pennycuik. On the running of the gnu (*Connochaetes Taurinus*) and other animals. *J. Exp. Biol.*, 63:775–799, 1975.
- [12] E.L. Rezende, S.A. Kelly, F.R. Gomes, M.A. Chappell, and Jr. T. Garland. Effects of size, sex, and voluntary running speeds on costs of locomotion in lines of laboratory mice selectively bred for high wheel-running activity. *Physiol. Biochem. Zool.*, 79(1):83–99, 2006.
- [13] Jr. T. Garland. Scaling the ecological cost of transport to body mass in terrestrial mammals. *Am. Nat.*, 121:571–587, 1983.
- [14] I. Girard. Field cost of activity in the kit fox, *vulpes macrotis*. *Physiol. Biochem. Zool.*, 74:191–202, 2001.
- [15] N. Corp, M.L. Gorman, and J.R. Speakman. Daily energy expenditure of free-living male wood mice in different habitats and seasons. *Funct. Ecol.*, 13:585–593, 1999.
- [16] K.A. Christian, R.V. Baudinette, and Y. Pamula. Energetic costs of activity by lizards in the field. *Funct. Ecol.*, 11:392–397, 1997.
- [17] J. Drent, W.D.V. Lichtenbelt, and M. Wikelski. Effects of foraging mode and season on the energetics of the marine iguana, *amblyrhyncus cristatus*. *Funct. Ecol.*, 13:493–499, 1999.
- [18] V. van Ginneken, E. Antonissen, U. K. Miller, R. Booms, E. Eding, J. Verreth, and G. van den Thillart. Eel migration to the sargasso: remarkably high swimming efficiency and low energy costs. *J. Exp. Biol.*, 208:1329–1335, 2005.

- [19] A. Hreljac. Preferred and energetically optimal gait transition speeds in human locomotion. *Med. Sci. Sports Exerc.*, 25:1158–1162, 1993.
- [20] R. McN. Alexander. Optimization and gaits in the locomotion of vertebrates. *Physiological Review*, 69(4):1199–1227, 1989.
- [21] G.A. Cavagna and P. Franzetti. The determinants of the step frequency in walking in humans. *J. Physiol. (Lond.)*, 373:235–242, 1986.
- [22] S. Grillner, J. Halbertsma, J. Nilsson, and A. Thorstensson. The adaptation to speed in human locomotion. *Brain Res.*, 165:177–182, 1979.
- [23] N.C. Heglund and C.R. Taylor. Speed, stride frequency and energy cost per stride: How do they change with body size and gait? *J. Exp. Biol.*, 138:301–318, 1988.
- [24] T.A. McMahon. The role of compliance in mammalian running gaits. *J. Exp. Biol.*, 115:263–282, 1985.
- [25] C.R. Taylor. Force development during sustained locomotion: A determinant of gait, speed and metabolic power. *J. Exp. Biol.*, 115:253–262, 1985.
- [26] C.T. Farley and C.R. Taylor. A mechanical trigger for the trot-gallop transition in horses. *Science*, 253(5017):306–308, 1991.
- [27] A. Hreljac. Determinants of the gait transition speed during human locomotion: kinetic factors. *Gait & Posture*, 1:217–223, 1993.
- [28] R. Kram, A. Domingo, and D.P. Ferris. Effect of reduced gravity on the preferred walk-run transition speed. *The Journal of Experimental Biology*, 200:821–826, 1997.
- [29] M.H. Raibert. Legged robots. *Commun. ACM*, 29:499–514, 1986.
- [30] F. Delcomyn. Insect walking and robotics. *Annu. Rev. Entomol.*, 49:51–70, 2004.

- [31] R.A. Brooks. New approaches to robotics. *Science*, 253:1227–1232, 1991.
- [32] K.S. Espenschied, R.D. Quinn, H.J. Chiel, and R.D. Beer. Leg coordination mechanisms in the stick insect applied to hexapod robot locomotion. *Adapt. Behav.*, 1:455–468, 1993.
- [33] J. Eltze and F. Pfeiffer. Optimization of a leg design. *J. Robot. Syst.*, 12:757–765, 1995.
- [34] H-J. Weidemann, F. Pfeiffer, and J. Eltze. A design concept for legged robots derived from the walking stick insect. *Proc. 1993 IEEE/RSJ Int. Conf. Intell. Robot. Syst.*, 1:545–552, 1993.
- [35] F. Delcomyn and M.E. Nelson. Architectures for a biomimetic hexapod robot. *Robot. Auton. Syst.*, 30:5–15, 2000.
- [36] R.D. Quinn, G.M. Nelson, R.J. Bachmann, and R.E. Ritzmann. Toward mission capable legged robots through biological inspiration. *Auton. Robots*, 11:215–220, 2001.
- [37] J.E. Bares and D.S. Wettergreen. Dante ii: technical description, results, and lessons learned. *Int. J. Robot. Res.*, 18:621–649, 1999.
- [38] P.R. Bandyopadhyay. Trends in biorobotic autonomous undersea vehicles. *IEEE J. Oceanic Eng.*, 30:109–139, 2005.
- [39] J. Yu, Y. Hu, R. Fan, L. Wang, and J. Huo. Mechanical design and motion control of a biomimetic robotic dolphin. *Advanced Robotics*, 21(3-4):499–513, 2007.
- [40] M.S. Triantafyllou and G.S. Triantafyllou. An efficient swimming machine. *Sci. Am.*, 272:64–70, 1995.

- [41] D. Barrett, M. Grosenbaugh, and M. Triantafyllou. The optimal control of a flexible hull robotic undersea vehicle propelled by an oscillating foil. In *Proc. 1996 IEEE AUV Symp.*, pages 1–9, Monterrey, CA, 1996.
- [42] J.M. Anderson and N.K. Chhabra. Maneuvering and stability performance of a robotic tuna. *Integ. Comp. Biol.*, 42:118–126, 2002.
- [43] J. Ayers, C. Wilbur, and C. Olcott. Lamprey robots. In *Proc. Int. Symp. on Aqua Biomechanisms*, pages 1–6, Tokai University, 2000.
- [44] N. Kato. Control performance in the horizontal plane of a fish robot with mechanical fins. *IEEE J. Oceanic Eng.*, 25:121–129, 2000.
- [45] M. Nakashima and K. Ono. Development of a two-joint dolphin robot. In *Neurotechnology for Biomimetic Robots*, pages 309–324. MIT Press, Cambridge, MA, 2002.
- [46] J. Yu, M. Tan, S. Wang, and E. Chen. Development of a biomimetic robotic fish and its control algorithm. *IEEE Trans. Syst., Man Cybernet. B*, 34:1798–1810, 2004.
- [47] S. Guo, T. Fukuda, and K. Asaka. A new type of fish-like underwater microrobot. *IEEE/ASME Trans. on Mechatronics*, 8(1):136–141, 2003.
- [48] T. Fukuda, K. Hosokai, and F. Arai. Giant magnetostrictive alloy (gma) applications to micro mobile robot as a micro actuator without power supply cables. In *Proc. IEEE Conf. Micro Electro Mechanical Systems*, pages 210–215, 1990.
- [49] L. Fearing. Micro structures and micro actuator for implementing sub-millimeter robots. In *Precision Sensors, Actuators and Systems*, pages 39–72. Kluwer, Norwell, MA, 1992.

- [50] T. Fukuda et al. Distributed type of actuator by shape memory alloy and its application to underwater mobile robotic mechanism. In *Proc. IEEE Int. Conf. Robotics and Automation*, volume 2, pages 1316–1332, 1991.
- [51] T. Fukuda, A. Kawamoto, F. Arai, and H. Matsuura. Mechanism and swimming experiment of micro mobile robot in water. In *Proc. IEEE Int. Conf. Robotics and Automation*, volume 1, pages 814–819, 1994.
- [52] T. Fukuda, A. Kawamoto, and F. Arai. Steering mechanism of underwater micro mobile robot. In *Proc. IEEE Int. Conf. Robotics and Automation*, volume 1, pages 363–368, 1995.
- [53] M. Mojarrad and M. Shahinpoor. Biomimetic robot propulsion using polymeric artificial muscles. In *Proc. IEEE Int. Conf. Robotics and Automation*, pages 2152–2157, 1997.
- [54] M.H. Dickinson, C.T. Farley, R.J. Full, M.A.R. Koehl, R. Kram, and S. Lehman. How animals move: An integrative view. *Science*, 288:100–106, 2000.
- [55] J.E. Colgate and K.M. Lynch. Mechanics and control of swimming: A review. *IEEE Journal of Oceanic Engineering*, 29(3):660–673, 2004.
- [56] C. Chevallereau and Y. Aoustin. Optimal reference trajectories for walking and running of a biped robot. *Robotica*, 19:557–569, 2001.
- [57] M. Saito, M. Fukaya, and T. Iwasaki. Serpentine locomotion with robotic snake. *IEEE Control Systems Magazine*, 22(1):64–81, 2002.
- [58] K.A. McIsaac and J.P. Ostrowski. Motion planning for anguilliform locomotion. *IEEE Trans. Robotics and Automation*, 19(4):637–652, 2003.

- [59] J. Cortes, S. Martinez, J.P. Ostrowski, and K.A. McIsaac. Optimal gaits for dynamic robotic locomotion. *The International journal of robotics research*, 20(9):707–728, 2001.
- [60] T. Saidouni and G. Bessonnet. Generating globally optimised sagittal gait cycles of a biped robot. *Robotica*, 21(2), 2003.
- [61] M. Srinivasan and A. Ruina. Computer optimization of a minimal biped model discovers walking and running. *Nature*, 439(7072):73–75, 2006.
- [62] J.P. Ostrowski, J.P. Desai, and V. Kumar. Optimal gait selection for nonholonomic locomotion systems. *The International journal of robotics research*, 19:225–237, 2000.
- [63] G. Bessonnet, S. Chesse, and P. Sardain. Optimal gait synthesis of a seven-link planar biped. *The International journal of robotics research*, 23(10-11):1059–1073, 2004.
- [64] G. Hicks and K. Ito. A method for determination of optimal gaits with application to a snake-like serial-link structure. *IEEE Trans. Auto. Contr.*, 50(9):1291–1306, 2005.
- [65] V.A. Langman, T.J. Roberts, J. Black, G.M.O. Maloiy, N.C. Heglund, J.M. Weber, R. Kram, and C.R. Taylor. Moving cheaply: Energetics of walking in the african elephant. *The Journal of Experimental Biology*, 198:629–632, 1995.
- [66] C. Heine. *Mechanics of flapping fin locomotion in the cownose ray, *Rhinoptera bonasus* (Elasmobranchii, Myliobatidae)*. PhD thesis, Duke University, Durham, 1992.
- [67] J.T. Schaefer and A.P. Summers. Batoid wing skeletal structure: Novel morphologies, mechanical implications, and phylogenetic patterns. *Journal of Morphology*, 264:298–313, 2005.

- [68] L.J. Rosenberger. Pectoral fin locomotion in batoid fishes: Undulation versus oscillation. *J. of Exp. Biol.*, 204(2):379–394, 2001.
- [69] C.M. Breder. The locomotion of fishes. *Zoologica*, 50:159–297, 1926.
- [70] P.W. Webb. The biology of fish swimming. In *Mechanics and Physiology of Animal Swimming*, pages 45–62, Cambridge, 1994. Cambridge University Press.
- [71] R. Forch. Exploring new paradigms in locomotion: The development and analysis of a simplified manta ray wing model. Master’s thesis, University of Virginia, Charlottesville, VA, 2009.
- [72] P.R. Last and J.D. Stevens. *Sharks and rays of Australia*. CSIRO Australia, Canberra, 1994.
- [73] W.T. White, J. Giles, and I.C. Potter. Data on the bycatch fishery and reproductive biology of mobulid rays (myliobatiformes) in indonesia. *Fisheries Research (Amsterdam)*, 82(1–3):65–73, 2006.
- [74] H. Dewar, P. Mous, M. Domeier, A. Muljadi, J. Pet, , and J. Whitty. Movements and site fidelity of the giant manta ray, manta birostris, in the komodo marine park, indonesia. *Marine Biology*, 155(2):121–133, 2008.
- [75] G. Notarbartolo di Sciara. Natural history of the rays of the genus mobula in the gulf of california. *Fishery Bulletin*, 86(1):45–66, 1988.
- [76] K. Yano, F. Sato, and T. Takahashi. Observations of mating behavior of the manta ray, manta birostris, at the ogasawara islands, japan. *Ichthyological Research [Ichthyol.-Res.]*, 46(3), 1999.
- [77] K. Homma, T. Maruyama, T. Itoh, H. Ishihara, and S. Uchida. Biology of the manta ray, manta birostris walbaum, in the indo-pacific. In *Proc. of the 5th Indo Pacific Fish Conference, Nouma*, pages 209–216. Societe Francaise d’Ichtyologie, 1997.

- [78] A.D. Marshall. *Biology and Population Ecology of Manta birostris in Southern Mozambique*. PhD thesis, The University of Queensland, Queensland, 2008.
- [79] F.E. Fish. Internal study. 2010. West Chester University.
- [80] R.S. Russo. Internal study. 2010. University of Virginia.
- [81] M.W. Spong and M. Vidyasagar. *Robot Dynamics and Control*. John Wiley & Sons, 1989.
- [82] R.E. Skelton and M.C. de Oliveira. *Tensegrity Systems*. Springer, 2009.
- [83] T. Bliss, T. Iwasaki, and H. Bart-Smith. CPG control of a tensegrity morphing structure for biomimetic applications. *Advances in Science and Technology*, 58:137–142, 2008.
- [84] T. Iwasaki. Coordinated rhythmic motion by uncoupled neuronal oscillators with sensory feedback. *J. Control, Measurement, and System Integration*, 1(2):165–174, 2008.
- [85] Z. Chen and T. Iwasaki. Circulant synthesis of central pattern generators with application to control of rectifier systems. *IEEE Trans. Auto. Contr.*, 53(3):273–286, 2008.
- [86] H.K. Khalil. *Nonlinear Systems*. Prentice Hall, 1996.
- [87] S. Hirose. *Biologically Inspired Robots: Snake-Like Locomotors and Manipulators*. Oxford University Press, 1993.
- [88] D.L. Hu, J. Nirody, T. Scott, and M.J. Shelley. The mechanics of slithering locomotion. *Proc. of National Academy of Sciences*, 106(25):10081–10085, 2009.
- [89] G. Taylor. Analysis of the swimming of long and narrow animals. *Proc. Royal Society of London. Series A*, 214(1117):158–183, 1952.

- [90] R.W. Brockett. Pattern generation and the control of nonlinear systems. *IEEE Trans. Auto. Contr.*, 48(10):1699–1711, 2003.
- [91] G. Zhu and R.E. Skelton. Mixed L_2 and L_∞ problems by weight selection in quadratic optimal control. *Int. J. Contr.*, 53(5):1161–1176, 1991.
- [92] M.J. Lighthill. Note on the swimming of slender fish. *J. Fluid Mech.*, 9:305–317, 1960.
- [93] T. McMillen and P. Holmes. An elastic rod model for anguilliform swimming. *J. Math. Biol.*, 53(5):843–886, 2006.
- [94] G. Bowtell and T.L. Williams. Anguilliform body dynamics: modeling the interaction between muscle activation and body curvature. *Phil. Trans. R. Soc. Lond. B*, 334:385–390, 1991.
- [95] O. Ekeberg. A combined neuronal and mechanical model of fish swimming. *Biological Cybernetics*, 69(5/6):363–374, 1993.
- [96] C.E. Jordan. Coupling internal and external mechanics to predict swimming behavior: a general approach? *Amer. Zool.*, 37:710–722, 1996.
- [97] J. Chen, W.O. Friesen, and T. Iwasaki. Mechanisms underlying rhythmic locomotion: Body-fluid interaction in undulatory swimming. *J. Exp. Biol.*, 214(4):561–574, 2011.
- [98] K. Moored. Panel method (internal study). *Princeton*, 2011.
- [99] T. Iwasaki and M. Zheng. Sensory feedback mechanism underlying entrainment of central pattern generator to mechanical resonance. *Biological Cybernetics*, 94(4):245–261, 2006.
- [100] T. Iwasaki. Multivariable harmonic balance for central pattern generators. *Automatica*, 44(12):4061–4069, 2008. (DOI:10.1016/j.automatica.2008.05.024).

- [101] Y. Futakata and T. Iwasaki. Formal analysis of resonance entrainment by central pattern generator. *J. Math. Biol.*, 57(2):183–207, 2008.
- [102] Z. Chen, M. Zheng, W.O. Friesen, and T. Iwasaki. Multivariable harmonic balance analysis of neuronal oscillator for leech swimming. *J. Computational Neuroscience*, 25(3):583–606, 2008. (DOI: 10.1007/s10827-008-0105-7).
- [103] Z. Chen and T. Iwasaki. Matrix perturbation analysis for weakly coupled oscillators. *Systems & Control Letters*, 58(2):148–154, 2009. (DOI:10.1016/j.sysconle.2008.10.002).
- [104] A.L. Fradkov and V.A. Jakubovic. The S-procedure and a duality relations in nonconvex problems of quadratic programming. *Vestnik Leningrad Univ. Math.*, 6(2):101–109, 1979. (English translation of a Russian publication in 1973).